September 2014

Investigation of the Crystallization of DNL-6 and FT-Raman Spectroscopic Investigation of Guest Molecules in MOFs

Maxwell Goldman
The University of Western Ontario

Supervisor
Dr. Yining Huang
The University of Western Ontario

Graduate Program in Chemistry
A thesis submitted in partial fulfillment of the requirements for the degree in Master of Science

INVESTIGATION OF THE CRYSTALLIZATION OF DNL-6 AND FT-RAMAN SPECTROSCOPIC INVESTIGATION OF GUEST MOLECULES IN MOFs

Monograph

by

MAXWELL, GOLDMAN

Graduate Program in Chemistry

A thesis submitted in partial fulfillment
of the requirements for the degree of
Master of Science

The School of Graduate and Postdoctoral Studies
The University of Western Ontario
London, Ontario, Canada

Abstract

Microporous solids are a widely used material in adsorption, storage and catalysis. In this thesis, the crystallization of the silcoaluminaphosphate DNL-6 was characterized using powder X-ray diffraction and solid state nuclear magnetic resonance. Two crystallization routes of the SAPO DNL-6 were studied, which are the hydrothermal method and the dry-gel conversion method. Both methods followed the same crystallization pathway and showed a layered intermediate that is then transformed into DNL-6. The reaction requires two templating agents to create the RHO topology and silicon substitutes into the framework by replacing single phosphorous atoms.

This thesis contains the conformational analysis of halocarbons adsorbed into different metal-organic frameworks has also been studied using FT-Raman spectroscopy. 1,2-dichloroethane and 1-bromo-2-chloroethane were adsorbed into MIL-53, MIL-68, MIL-53NH_2, while chlorocyclohexane was adsorbed in MIL-53. For non-polar frameworks the main guest-host interactions are van der Waal interactions. The polar framework of MIL-53NH_2 is able to stabilize the *gauche* conformation of DCE and BCE at room temperature. The enthalpy of each system was determined through variable temperature FT-Raman spectroscopy and the width of the Raman bands was able to give information regarding the molecular motion of the halocarbons.

KEYWORDS: Silicoaluminaphosphate, DNL-6, crystallization, SSNMR, MOFs, FT-Raman, conformational analysis, 1,2-dichloroethane, 1-bromo-2-chloroethane

To: My dad

Joel Goldman

Acknowledgements

I would like to thank my supervisor Dr. Yining Huang for his guidance, assistance and teachings over the past two years.

Kim Law, and Grace Yau for access to the powder X-ray diffractometer. Mathew Willans for his patience, and constant help with the SSNMR. To all my lab-mates and friends in the Dr. Ding's lab thank you for constantly being supportive over the last two years. I would like to thank Adam MacIntosh for his guidance and tutelage during my first semester your help cannot be quantified.

Lastly I would like to thank my father, Joel Goldman, without his support it would not have been possible to accomplish all that I have.

TABLE OF CONTENTS

CHAPTER 3 INVESTIGATION INTO THE CRYSTALIZATION OF DNL-6 BY HYDROTHERMAL SYNTHESIS AND DRY-GEL CONVERSION METHODS

CHAPTER 4 CONFORMATIONAL ANALYSIS OF HALOCARBONS IN METAL ORGANIC FRAMEWORKS BY FT-RAMAN SPECTROSCOPY

List of Figures

Figure Page

List of Tables

List of Abbreviations

DCE	1,2-dichloroethane
BCE	1-bromo-2-chloroethane
CCH	1-chlorocyclohexane
BDC-NH_2	2-amino-terephthalic acid
$AlPO_4$s	aluminophosphates
AM	as-made
BDC	benzene dicarboxylic acid
CMACl	cetylmethylammonium chloride
CTACl	cetyltrimethylammonium chloride
CP	cross polarization
d	days
DTG	derivative of thermal gravimetric analysis curve
DEA	diethylamine
d8R	double-8-rings
DGC	dry-gel conversion
LT	exposed to air
HT	evacuated
FT-Raman	fourier transform Raman
FWHH	full width at half height
A	Gibbs free energy
h	hours
HTS	hydrothermal synthesis
LTA	Linde Type A
MAS	magic-angle spinning
MOFs	metal-organic frameworks
MIL-53	MIL-53(Al)
MIL-53-NH_2	MIL-53-NH_2(Al)
MIL-68	MIL-68(In)
NMR	Nuclear magnetic resonance spectroscopy
O	oxygen
PXRD	powder X-ray diffraction
PBU	primary building units
RT	room temperature
SBU	secondary building unit
S/N	signal-to-noise ratio
SAPOs	silicoaluminophosphates
SSNMR	solid-state nuclear magnetic resonance
SAC	steam-assisted conversion
SDAs	structure directing agents
T	tetrahedral
T-units	tetrahedral units
TTMSS	tetrakis(trimethylsilyl)-silane
TGA	thermal gravimetric analysis

$t \rightarrow g$	*trans* to *gauche*
vdW	van der Waals
VPT	vapor phase transport
VT	variable temperature
XRD	X-ray diffraction

Chapter 1

Introduction

1.1 Zeolites

Zeolites are a family of microporous aluminosilicates. They are naturally occurring and were first synthesized by Richard Barrer and Robert Milton in 1948.[1] Zeolites are inorganic porous materials that have a low density and high surface area.[2] Barrer recognized that these properties could be used for hydrogen storage, which has become one of the leading uses for aluminosilicates. The negatively charged zeolite framework may also be loaded with protons to perform selective acid catalyzed reactions, by selectively allowing guest-molecules to permeate through the pores.[2]

Zeolites are limited to valence elements that can form tetrahedral such as Al, Si, due to constraints of bond angles and bond lengths.[3] Zeolites contain SiO_4 and AlO_4 building blocks that act as primary building units (PBU). Each tetrahedral (T) site (primary building unit) is bonded by four oxygen atoms (O) and forms either Si-O-Al or Si-O-Si linkages. Each T-O-T link forms a shape, which is defined as a secondary building unit (SBU). Each SBU is a three dimensional portion of the framework, and is a repeating structure which comprises the unit cells. Zeolites and other microporous material frameworks are created by either connecting identical SBUs, or by alternating different SBUs. When repeating SBUs form a unique framework, it is denoted by a three-letter code (topology code).[4] The topology code solely describes the connectivity of SBUS regardless of the tetrahedral atoms within

the framework.[4] Novel zeolites are also given a name that is chosen by the founders, for example ZSM-5 which stands for Zeolite Socony Mobil – 5.[5] All zeolites crystallize into different three dimensional structures with different pore sizes and pore connectivities. One of the most widely used zeolites in industry is Zeolite A due to its adsorption qualities.[6] Zeolite A (Figure 1.1) has a Linde Type A topology (LTA), which is composed of a single α-cage that is made by connecting eight sodalite cages, connected by twelve double-4 rings per unit cell.

1.1.2 Aluminophosphates

Another class of microporous materials are aluminophosphates ($AlPO_4$s). They are similar to zeolites, however, SiO_4 tetrahedra are replaced by PO_4.[7] The SBUs for this class of porous materials are built by strictly alternating Al and P tetrahedra (Al-O-P), which results in a neutral open framework.[8] Flanigen et al. were able to create a new subclass of microporous materials, silicoaluminophosphates (SAPOs) by introducing silicon into the $AlPO_4$ framework.[9]

1.1.3 Silicoaluminophosphates

SAPOs contain SiO_4, PO_4, and AlO_4 tetrahedra as the PBU. The SBUs are made up of Si-O-Al, Si-O-Si, and Al-O-P linkages. However, Si-O-P linkers were theoretically calculated to be energetically unfavorable due to the fact that it would create a positively charged framework.[10] No Si-O-P linkage has been observed experimentally in any SAPOs.[11] There are three suggested routes for silicon incorporation into the framework. The first substitution mechanism, SM1, involves a silicon atom replacing an aluminum atom. This route is highly unlikely as it leads

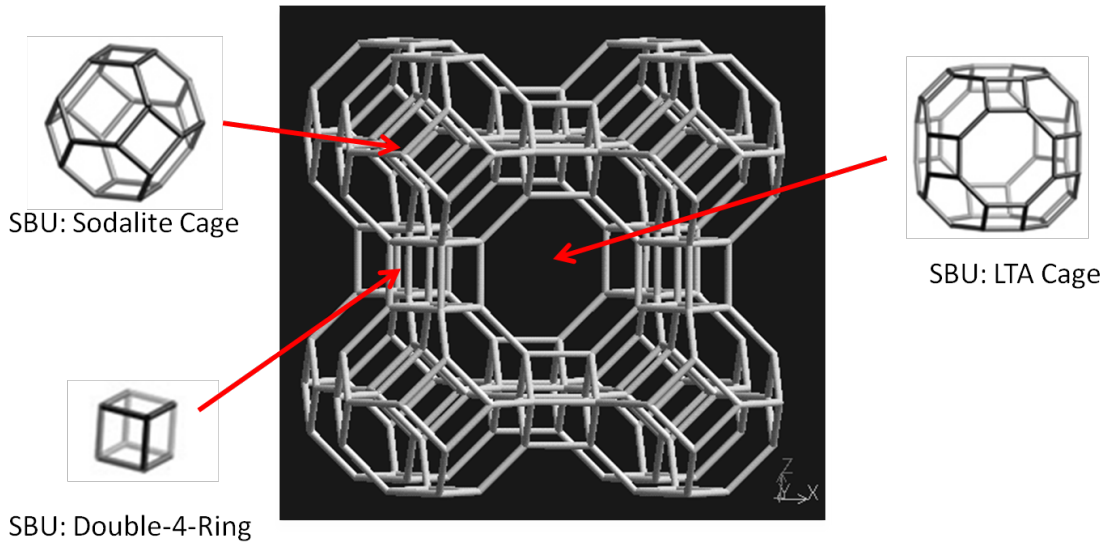

Figure 1.1 Zeolite A, with 3 different SBUs, Double-4-Rings, Sodalite Cages, and LTA Cage.[7]

to a positive framework charge due to the creation of a Si-O-P linkage.[10] The second suggested route, SM2, is the incorporation of Si into a P site. The SM2 mechanism creates four Si-O-Al linkages from a central atom. The third, SM3, involves two Si atoms replacing an Al atom and a P atom.[10] It is important to note that silicon cannot be incorporated solely through the SM3 method and that some SM2 must take place to avoid a Si-O-P bond.[10] When the concentration of Si atoms plus P atoms equals fifty percent the SAPO favors SM2 as the incorporation route, and when Si atoms plus P atoms are greater than fifty percent a mix of SM2 and SM3 is preferred.[10] To understand the incorporation of silicon into the SAPO framework, the route of crystallization of DNL-6 was chosen for this study. DNL-6, which has the same topology as zeolite RHO, has practical applications that include methanol to olefin conversion, and methyl ammonia to methylamine conversion, and strong adsorption properties.[12] As well, Zeolite RHO has the second highest CO_2 adsorption capacity behind the industry standard LTA.[13]

1.1.3.1 RHO Topology

The RHO topology has two SBUs, double-8-rings (d8R), and LTA cages (Figure 1.2). The framework can be described as alternating LTA cages and d8R (Figure 1.3).[14] RHO crystallizes into the cubic $Im\bar{3}m$ space group with only one symmetrically independent tetrahedral site, and two unique oxygen sites. The cell parameters are a = b = c = 14.91 Å, with a pore size of 3.6 x 3.6 Å.[14] However, it is more cost effective to synthesize DNL-6 as zeolite RHO requires expensive cesium crown-ether as a structure directing agent.

1.1.3.2 DNL-6

DNL-6 crystallizes into a cubic Im-3m space group. Compared to the zeolite RHO, DNL-6 has a smaller pore opening but a larger internal volume of .36 cm^3/g compared to zeolite RHO which has a volume of .26 cm^3/g.[14,15] DNL-6 has one equivalent P-site within the framework, $P(OAl)_4$, as well as one Si-site, which is an isolated silicon atom within the framework, $Si(OAl)_4$. Experimentally it has been determined that no silicon islands form within this framework.[15] By studying the crystallization structure of DNL-6 it is possible to optimize potential applications of the RHO framework, at a significantly lower cost than the zeolite RHO.

1.2 Crystallization of Aluminosilicates and Silicoaluminophosphates

This section will detail how zeolites, $AlPO_4$s and SAPOs crystallize.

1.2.1 Structure Directing Agents

Structure directing agents (SDAs) were first observed in the 1960s when alkali cations were added to the synthesis of microporous materials. SDAs were added to aid in the polymerization of silicon and aluminum in forming zeolite frameworks.[16] Due to the complexity of individual frameworks it is believed that the SDAs stabilize the subunit, which is the nucleating species in crystallization.[17] In particular, alkali cations, amines, quaternary ammonium cations and alcohols have all been studied in depth as to their respective effect on crystallization of microporous materials.[16] To create larger pores, a surfactant can be employed that causes nucleation via micellation.[18] The main drawback in using SDA is that one SDA can lead to many frameworks. Due to the lack of specificity in SDA, it is necessary to

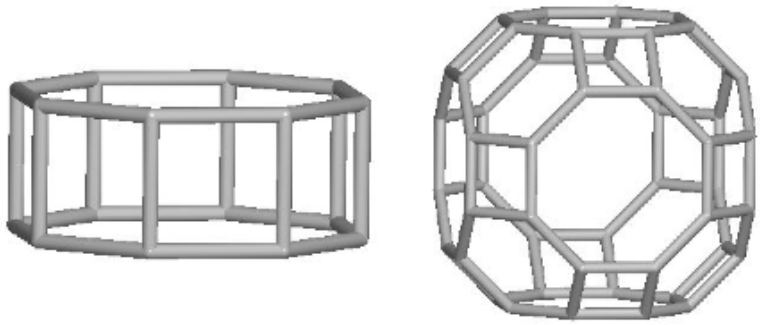

Figure 1.2 Double-8-Rings on the left and Linde Type A cage on the right.[7]

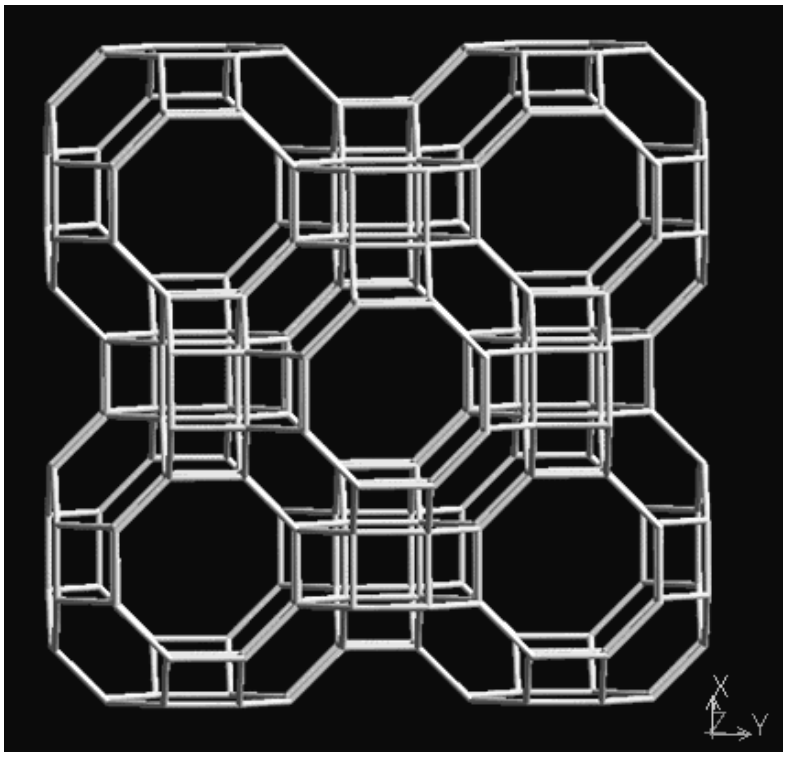

Figure 1.3 RHO framework, d8R rings connecting LTA cages.[7]

use accurate synthetic conditions as the gel composition and the SDA together will ultimately decide the framework of a zeolite.

1.2.2 Silicon Islands

The most stable form for the silicon to incorporate into an aluminum-phosphate framework during the formation of SAPOs involves the formation of silicon islands.[19] The first mechanism of forming a silicon island is via SM2. During SM2, one phosphorus atom is replaced by one silicon atom. This creates an isolated silicon atom from which silicon aggregates can form. When aggregation occurs solely via SM2 it is due to the presence of a low silicon concentration and happens by a favorable interaction between neighbour acid sites.[19] The favorable interaction between acid sites allows for low Si concentrations to aggregate and form silicon islands.[19] The other type of formation of silicon islands results from a mix of SM2 and SM3 which requires a high concentration of silicon.[20] Within the framework of a SAPO, the smallest possible silicon islands that can form because of Si-O-P linkages being prohibited are five atom silicon islands and eight atom silicon islands. The five atom silicon island is made by replacing one aluminum atom and four phosphorus atoms by five silicon atoms, and involves three SM2, and one SM3. In order to form the eight silicon island, two aluminum and six phosphorus are replaced by eight aluminum, via four SM2, and two SM3.[19] These islands have all been found to be thermodynamically favorable.[19] As these aggregates replace a large quantity of phosphorus atoms as opposed to aluminum atoms, the silicon islands are consistent with the lack of Si-O-P linkages which are energetically unfavorable.[19]

1.2.3 Acidity

The introduction of a silicon atom into the framework of an $AlPO_4$ creates a Brønsted acid site. This acidity results from hydroxyl groups being formed by neutralizing the net negative charged Si-O-Al linkages.[21] The hydroxyl groups in question come from the Si-OH-Al linkages, as opposed to hydroxyl groups that arise from lattice termination or defects within the structure.[22,23] Less acid sites are present, due to silicon island formation, increasing the strength of the remaining sites, and causing the strongest Brønsted acid sites to sit at the terminal silicon of the island. Another factor affecting the strength of the Brønsted acid site is the bond angle between two tetrahedra (T-O-T). The association between the potential energy and the bond angles indicates 144° as favorable.[24] Finally, the overall composition of the framework effects the strength of the bridging hydroxyl sites. A higher mean electronegativity of the framework (a decrease in aluminum), will lead to higher acid strengths of the SAPO.[25]

1.2.4 Hydrothermal Synthesis of Aluminosilicates and Silicoaluminophosphates

In the hydrothermal synthesis method (HTS), supersaturated gels are used to create microporous materials. All precursors are placed inside a Teflon container with excess water and sealed within an autoclave, then heated in an oven at a set temperature for a set period of time. The reaction takes place at high temperature and pressure. Early proposals for the mechanisms of zeolite synthesis, by Flanigen and by Breck, involve the growth of Al-O-Si bonds where growth occurred mainly in the solid phase.[26] Barrer then purposed a mechanism that consists of a liquid phase

reaction, where polyhedra building units undergo condensed polymerization to form zeolites.[27] Afterwards, Breck proposed that the formation of zeolites would be aided by hydroxide ions in the liquid phase.[26] The early rearrangement of silicate and aluminosilicate ions is aided by hydroxide ions and the tetrahedra would regroup around the hydrated sodium ions to form polyhedra.[26] Burkett and Davis examined the role of SDAs in zeolite synthesis. It was determined that SDAs and the inorganic species (Si, Al) form pre-organized organic and inorganic systems.[28] This ordered system, containing SDAs and inorganic species, is made by the overlap of hydrophobic hydration spheres within the gel.

Zeolite crystallization can be divided into three stages: induction period, nucleation, and crystal growth.

The induction period is defined as the start of the reaction to the time when the first detectable crystalline structure is formed and its denoted by equation 1.1[29]

$$\tau = \tau_r + \tau_n + \tau_g \qquad (1.1)$$

where τ_r is the relaxation time and is defined as the time taken to go from the first amorphous phase to the second amorphous phase.[26] The secondary amorphous phase is an equilibrated gel between solid phase and solution phase where the solid phase is more ordered. The ordered gels are formed by dissolution and reprecipitation. τ_n is the formation time of a stable nucleus and τ_g is the time for the nucleus to grow to a detectable size.[29] The primary amorphous phase exists once a silicon source and an aluminum source are mixed in a solution. Initially two metal cations and hydroxyl anions exist in a heterogenous non-equilibrated state. Once

heating takes place under elevated pressure a slow process of ordering begins to occur. Ionized monomers of $Si(OH)_4$, begin to polymerize in a reversible reaction of water exchange. When the polymers are combined with $Al(OH)_4^-$ a colloidal and aluminosilicate gel exists in equilibrium, which is the secondary amorphous phase. Once the secondary amorphous gel has reached equilibrium, a stable nucleus exists.[26]

For nucleation to commence, the energy of cohesion must be larger than the expended energy of the surface that divides the solid and liquid phases, therefore, the nucleus must be equal to the critical nucleus size.[29] The critical nucleus size is dependent on the experimental conditions of the synthetic procedure. One technique to reduce the nucleation time is through seeding. Seeding introduces a pre-made crystal into the reaction gel. Seeding allows for the induction and nucleation periods to be bypassed, and creates a synthetic direction which allows for control over crystal size. Seeding requires a large surface area and prevents the solution from reaching high levels of supersaturation allowing growth to take place on the crystal.[30]

Another mechanism to speed up reaction time is through SDAs, which allow nucleation to begin earlier. The SDA mediates the combination of tetrahedral units (T-units) from an incorrect geometry for aggregation by guiding the T-units into a more favorable geometry. After a period of time, the cation can either become trapped within the T-units, or can migrate to a neighbouring site to repeat the process.[26] Once nucleation has occurred, a large stable nucleus allows the propagation of zeolite growth. In the HTS, the rate of crystal growth is slow and

linear. This suggests that the growth mode is surface adsorption, in which the structure is created layer by layer.[31] During the growth of a layer, a growth unit is adsorbed on the surface and then migrates to a kink site until the layer is complete.[32] A kink atom only has three nearest neighbours and is the site of lowest energy for crystal growth. Once the layer is complete, either a dislocation is necessary or a monolayer island is formed via 2D nucleation. Another mechanism for zeolite growth is through aggregation.[33] Aggregation takes place when two particles of comparable size combine together, with each future aggregation involving larger particles. However, layer-by-layer is the predominate growth mechanism as seen through experimental findings.[29]

Even with current studies the crystallization process of zeolites and other microporous materials is still not completely known. The major drawback of the HTS method is that it is difficult to study *in-situ* due to the reactions taking place at high temperature and high pressure. Another drawback is the reaction times tend to be fast and this prevents the isolation of intermediates. When all the precursors are in a gelatinous state, any intermediates could be washed away while drying the sample. Using a solid precursor opposed to a saturated gel can alleviate some of these problems.

1.2.5 Dry-Gel Synthesis of Aluminosilicates and Silicoaluminophosphates

Dry-gel conversion (DGC) involves a dried sample that is suspended above a liquid phase in an autoclave and thus has no direct contact with the gel (Figure 1.4). DGC can be described as either vapor phase transport (VPT), or steam-assisted

conversion (SAC). The VPT method has water and the SDA in the liquid phase. SAC has only water in the liquid phase, which is used more commonly when non-volatile compounds are used as the template. The DGC technique is primarily used to slow down the reaction, preventing the loss of soluble reactants to the liquid phase and thus increasing the yield. The DGC method has also been successfully used to obtain zeolites, which are not obtainable from a wet gel.[34] The solid-state transformation is an internal bond switching from an amorphous solid to a crystalline phase.[35] Gittleman et al. believe that upon heating a silica network, encapsulating hydrophobic cations will rearrange through bond breaking and reformation into a more stable structure.[35] Recent studies have shown that the change in size and morphology of the final crystals compared to the precursor solid indicates that a type of recrystallization process takes place.[26] The lack of a distinct amorphous phase causes the most likely transformation to be through short-range rearrangement at the molecular level.

It has been suggested that crystallization will occur using VPT when insufficient water is used to hydrate the sample, but will decrease the rate of crystallization.[36] Changing the amount of water in the liquid phase has the greatest effect on crystallization rate. Other synthetic conditions effect the rate as well, but not to the same degree. Using either VPT or SAC has little effect on the rate of crystallization. Studies have shown that using two different SDAs, one in the gel and one in the liquid phase, does not create a competing phase.[37] Depending on the gel composition either the gel SDA or the liquid phase SDA can be the dominant templating agent. However, introducing aluminum to the precursor does tend to

favor the SDA in the dry gel.[37] It is thought that either due to increased rigidity of the framework or enhanced interactions with the organo-cations the gel SDAs take preference over the SDA in the water. This phenomenon has been seen experimentally where aluminum containing gels produced more crystalline product than their pure silica counterpart.[37] DGC is a viable alternative route in the study of crystallization of microporous aluminosilicates and will be utilized in this study to investigate the crystallization process of DNL-6.

1.2. Metal-Organic Frameworks

Metal-organic frameworks (MOFs) are another class of microporous materials. Porous and thermally stable MOFs were first reported in 1999 by Yaghi and Li.[38] MOFs differ from zeolites in that they contain a uniform framework that is composed of organic linkers and inorganic metal cations. MOFs are more versatile than zeolites due to their ability to functionalize organic linkers, which facilitates rational design. Different organic linkers can be used to form different frameworks with the same metal to change the properties of the resulting MOF. In addition, some MOFs have a flexible framework.[39] The crystal growth of MOFs is highly dependent on synthetic conditions. Temperature, stoichiometric ratios, time, and precursors all control the outcome of the final product. In the early formation of a MOF, overall particle size of the finished framework will be dependent on early nucleation, where the rate limiting step is the formation of the first PBUs when the metal becomes a free ion in solution[40]. Afterwards the SBUs are formed, which are a cluster of metal-oxygen-carbon bonds that dictate the overall topology of the MOF

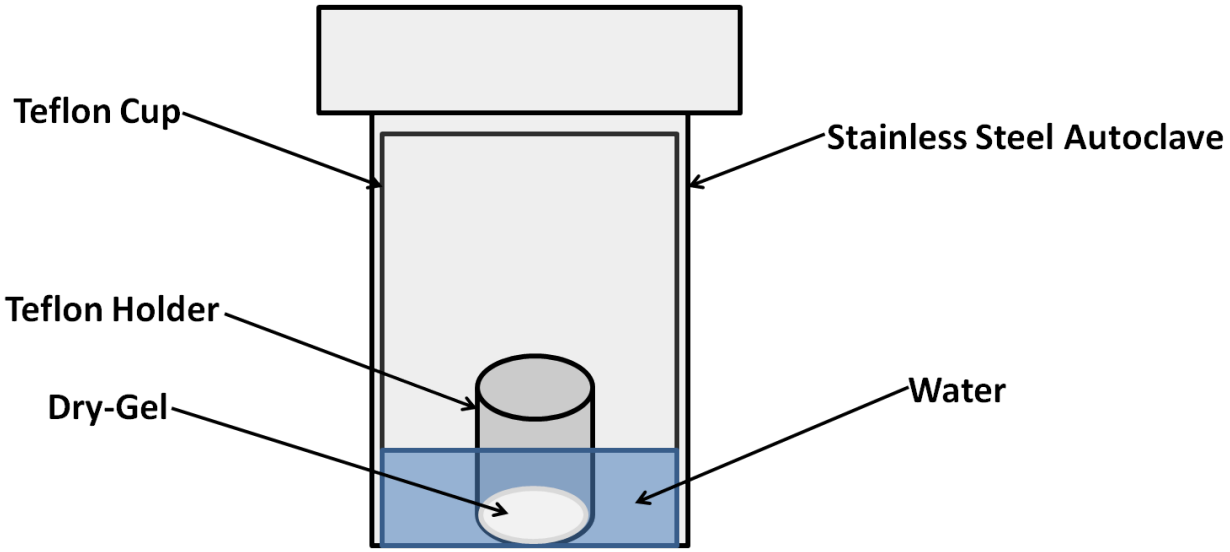

Figure 1.4 Typical dry-gel experimental setup.

being synthesized.[40,41] In this study, three different MOFs were examined due to their different and unique properties. MIL-53 was chosen for its flexible framework, MIL-53NH_2 as it has a polar and flexible framework, and MIL-68 as it has two different pore channels.[39, 42, 43]

1.2.1 MIL-53(Al)

MIL-53(Al) (MIL-53), which stands for Matériaux de l'Institut Lavoisier 53, is a metal organic framework that contains benzene dicarboxylic acid (BDC) as organic linkers that connect to metal centers (aluminum for this study) to form a stable and flexible framework.[45] MIL-53 contains an aluminum metal center, which is octahedrally coordinated to four oxygen atoms from separate BDC groups and two oxygen atoms from bridging hydroxyl groups. Depending on the absorbed molecule, MIL-53 will slightly alter its framework by changing its pore size, a breathing effect (Figure 1.6).[45] Depending on the guest molecule the pore size of this flexible framework will change. For example, the as-made (AM), the high-temperature (HT) and the low-temperature (LT) all have a different pore size.[45] As well as changing pore size, MIL-53 will also change crystallographic space groups, pore sizes and unit cell dimensions. For example, MIL-53(AM) has a monoclinic crystal system and crystallizes in the C2/c space group, while the MIL-53(HT) has an orthorhombic crystal system and crystallizes in the *Imma*.

1.1.4.2 MIL-53NH_2(Al)

MIL-53-NH_2(Al) (MIL-53-NH_2) is an amino modified version of MIL-53. Using 2-amino-terephthalic acid (BDC-NH_2) as the organic linker it is possible to create a

modified framework (Figure 1.7). The reason for creating a modified version of MIL-53, is to create a polar framework, as primary amines have roughly a dipole moment of 1.3D.[46] MIL-53-NH_2 contains the same breathing effect as the non-modified MOF, however in the absence of any sorbents, it is energetically favorable for MIL-53 to adopt the large pore form. In contrast, MIL-53-NH_2(AM) adopts the narrow pore form due to hydrogen-bonding involving the amine and AlO_6 moieties.[42] The unit cell parameters of MIL-53-NH_2 differ from MIL-53, as the AM adopts a monoclinc crystal system and the LT adopts a orthorhombic crystal system. The narrow-pore and large pore cell dimensions of a, b, c (MIL-53-NH_2) also differ from the unit cell dimensions of a, b, c (MIL-53).[42]

1.1.4.3 MIL-68(In)

MIL-68(In) (MIL-68) has a three dimensional network that has a Kagome-like lattice. It contains indium octahedra as metal centers that are connected by terephthalic acid and bridging hydroxyls to create two distinct pores (Figure 1.8). MIL-68 crystallizes into the orthorhombic space group Cmcm with cell dimensions of a = 21.77 Å, b = 37.67 Å, c = 7.23 Å which were obtained from single crystal X-ray diffraction.[43] The large and small pores of MIL-68 have a window size of 16 Å and 7 Å respectively.

1.4 Conformational Properties

Conformational isomers are a type of stereoisomers that became widely accepted in the study of organic chemistry due to the work of Barton in 1950.[47]

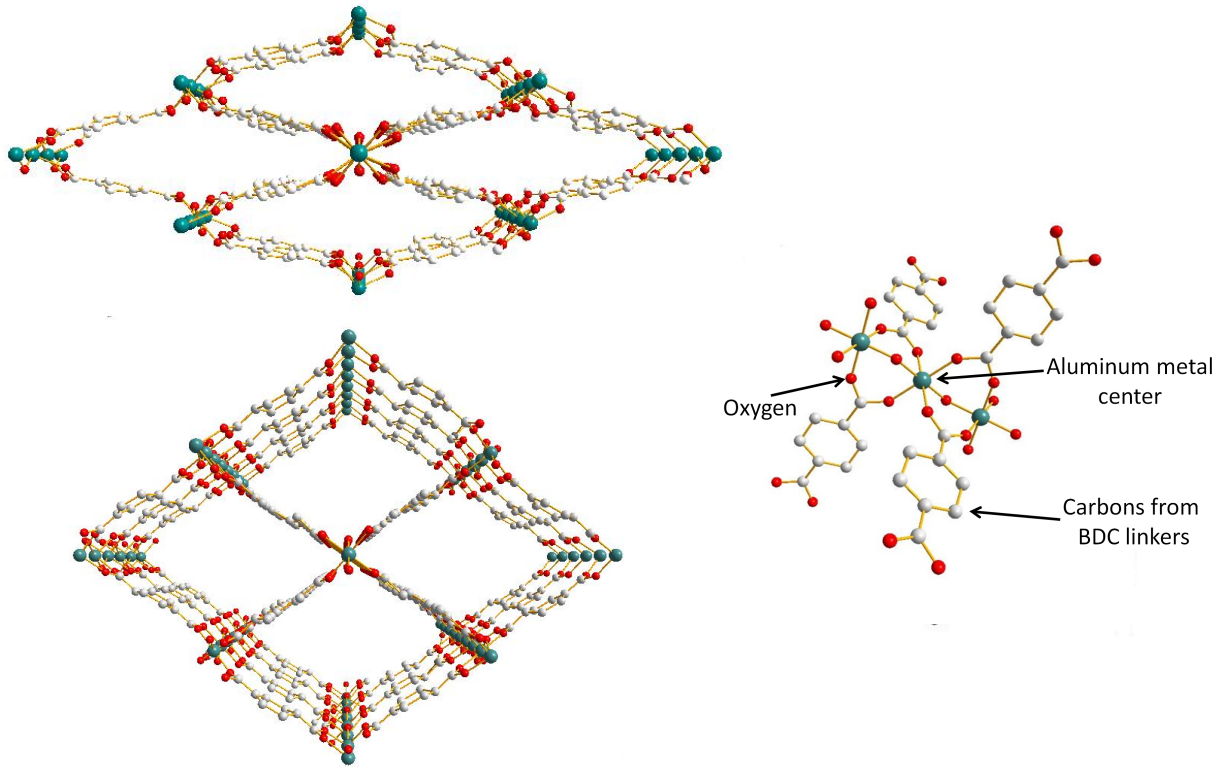

Figure 1.6 On the left, on top is the HT version of MIL-53 (monoclinc) with the LT (orthorhombic) version underneath. The SBU for MIL-53 can be seen on the right (White: Carbon, Teal: Aluminum, Red: Oxygen)

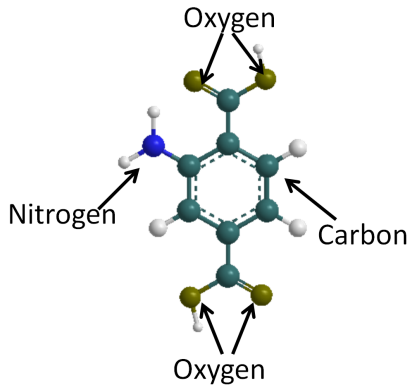

Figure 1.7 The organic linker for MIL-53NH2: 2-amino-terephlatic acid. (White: Hydrogen, Brown: Oxygen Teal: Carbon, Blue: Nitrogen)

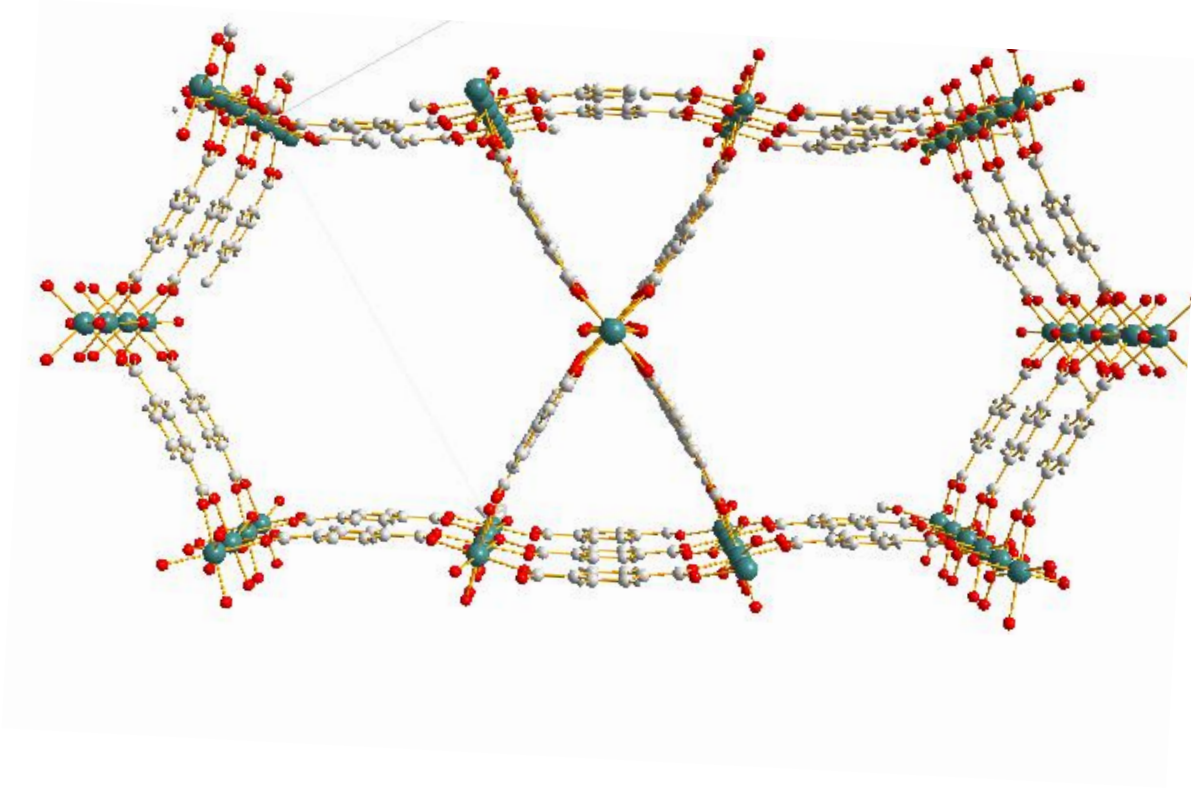

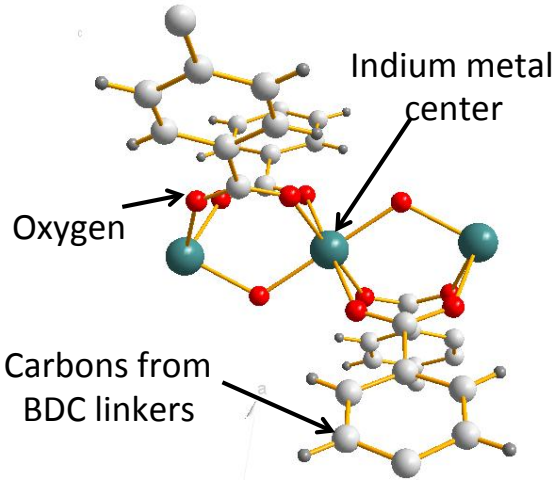

Figure 1.8 On top: MIL-68(In) (orthorhombic), On Bottom: SBU of MIL-68(In) (Red: Oxygen, White: Carbon, Teal: Indium)

Conformational isomers are formed through internal rotations of a molecule unlike enantiomers, which are mirror images of one another and non-superimposable. For a conformational isomer to be formed, a rotation must occur about a bond between two atoms, where each atom has a minimum of one other substituent. There are two different conformations that can take place, staggered and eclipsed. When the conformation takes on a staggered conformer it can further be subdivided into *trans* and *gauche* if each molecule has at least one substituent.[48] The process of an internal rotation about a bond takes less energy than to distort a bond angle. Assuming that all rotational angles have the same probability of occurring, we can assume a free rotation exists about any bond. However, as the rotation is hindered by sterics, there is no free rotation, as there is more than one minima per complete rotation around a bond. If the chain is non-hindered, for example as in ethane, then 3 distinct minima occur, all of which cannot be isolated from one another.[49] The conformational energy diagram of pure ethane shows these different energy minima and maxima.

In this study disubstituted ethane is being use to study the adsorption of halocarbons in MOFs. While the disubstituted ethane still has three distinct energy minima, the energy minima are not equal in energy as found in pure ethane (Figure 1.9). This is due to staggered conformation being able to take on both the *trans* and *gauche* conformers, with the anti being lowest in energy due to the two substituents being furthest away from each other which minimizes steric interactions. These conformers exist at equilibrium in solution and usually show a preference for the *trans* state due to sterics. However, depending on the substituents attached to ethane this is not necessarily the case.[49]

Ring compounds can also take on different conformations, as seen with cylcohexane. Cyclohexane has two distinct conformations, which are the chair and boat conformers. The chair conformer is the lowest energy minima that cyclohexane can adopt. The chair conformer is non-planar and is free of both angle strain, as all carbon-carbon bond angles are 109.5°, and torsional strain.[49] When viewing down any of the carbon-carbon bonds of cyclohexane, the C-H bonds are perfectly staggered. As well, the hydrogen atoms at either end of the ring are staggered to prevent any possible interactions between hydrogen atoms (steric repulsion). The boat conformer, which represents the lower energy maxima of cyclohexane's conformers, is also free of any angle strain. Unlike the chair conformer, the boat conformer is not completely free of torsional strain. In the boat conformation the hydrogen atoms located on C1 and C4 are close enough to one another to induce steric van der Waals repulsion. The boat conformation is 6.9 kcal/mole less stable than the chair conformation.[48] The boat conformation is not as rigid as the chair conformation and is therefore able to twist into the twist boat conformation to relieve van der Waals repulsion and alleviate some of the torsional strain found in the pure boat conformation. The twist boat conformation is 5.3 kcal/mole less stable then the chair conformation (Figure 1.10).[49]

Cyclohexane can have a single substituent group replacing a hydrogen atom while in the chair conformation. The substituent can be located in one of two positions, the axial and the equatorial position. The bonds that lie in the equatorial position point outwards from the chair conformation, while the bonds that lie in the

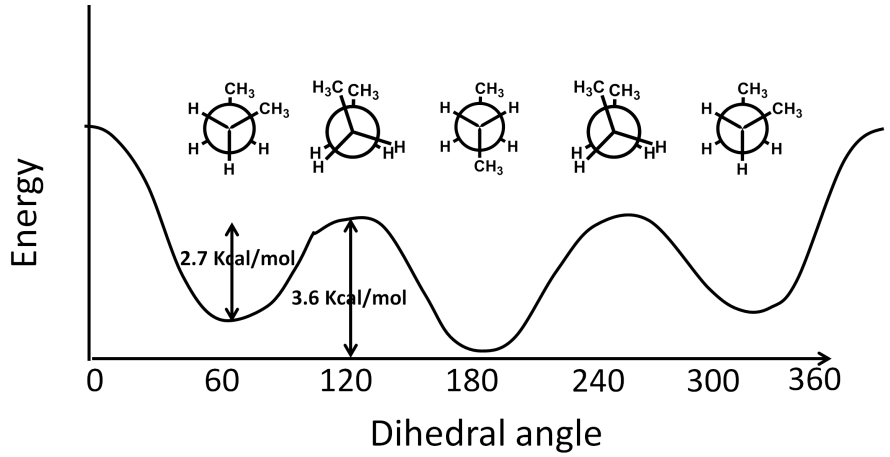

Figure 1.9 Conformational energy diagram of dimethyl-ethane (butane).

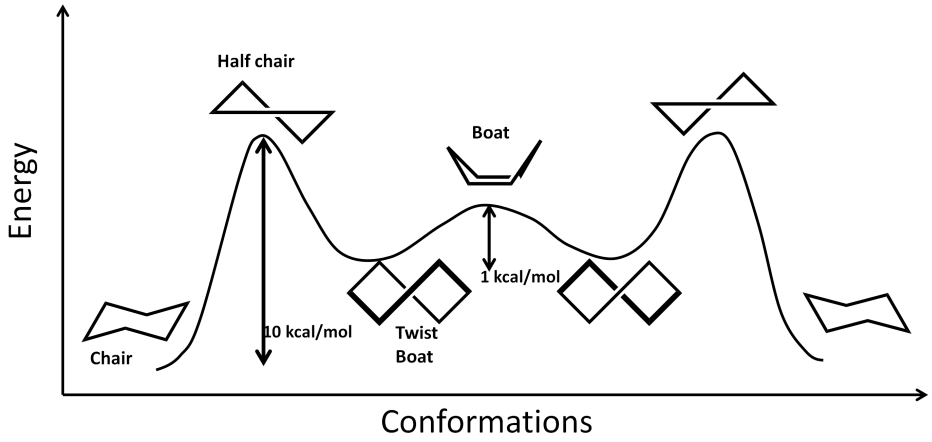

Figure 1.10 Conformational energy diagram of cyclohexane.

axial position point up and down from the chair conformation.[48] Determining whether a substituent will be located in the equatorial or axial position is dependent on its Gibbs free energy (A). When the value of A is positive the substituent is located in the equatorial position. Large and bulky substituents will have a larger value of A and a greater chance of being found in the equatorial position. While a substituent is in the equatorial position, it will minimize the interactions between the substituent located on C1 and the hydrogen atoms located on C3 and C4. This thesis studies the axial and equatorial conformations of chlorocyclohexane by FT-Raman spectroscopy.[49]

1.5 Aim of Thesis

Microporous materials such as SAPOs have a wide range of possible industrial applications. While multiple hypotheses have been made regarding the crystallization process of zeolites, $AlPO_4$s, and SAPOs there is yet to be universal agreement on what is occuring at a molecular level. By comparing the different HTS and DGC synthetic methods of synthesizing DNL-6 it is hoped that further insight will be gained into the crystallization pathway of microporous materials. Hopefully, this knowledge will aid in further research and discovery of new materials. Practical applications for MOFs include catalysis, separation, and adsorption which are their most common use.[39] By understanding the sorbate-sorbent relationship, it is possible to further understand the adsorption mechanism. In this study, a conformational analysis of halocarbons in different MOFs is used to determine which guest-host interactions are taking place. Halocarbons are highly toxic to the environment and humans. They are known to cause cancer, brain damage, birth

defects, liver failure, and an assortment of other diseases.[50,51] Disposal of halocarbon waste is problematic as incineration can lead to poisons and corrosive acids being released. Long-term storage may present a solution to the current problem.

The population of the conformations of haloalkanes, and halo-cyclicalkanes can change depending on interactions taking place with the environment. Depending on the system of the halocarbon its conformation will change depending on hydrogen bonding, dipole-dipole interactions, sterics, or dispersion forces. By understanding the conformation that the halocarbon takes in different MOFs it will allow the understanding of sorbate-sorbent interactions for possible storage. This conformational analysis was done through vibrational spectroscopy.

1.6 References for Chapter 1

1. Barrer, R. M., *J. Chem. Soc.* **1948,** *0* (0), 127.

2. Ozin, G. A.; Ozkar, S.; McMurray, L., *J. Phys. Chem.* **1990,** *94* (21), 8289.

3. Baerlocher, C.; McCusker, L. B.; Olson, D. H. *Atlas of Zeolite Structure Types*. fifth ed.; Elsevier: Amsterdam, 2001.

4. Association, I. Z. Framework Type Codes. http://izasc.ethz.ch/fmi/xsl/IZA SC/Help_Str.htm (accessed July 7th 2013).

5. Lermer, H.; Draeger, M.; Steffen, J.; Unger, K. K., *Zeolites* **1985,** *5* (3), 131.

6. *J. Chem. Educ.* **1999,** *76* (10), 1416.

7. Wilson, S. T.; Lok, B. M.; Messina, C. A.; Cannan, T. R.; Flanigen, E. M., *J. Am. Chem. Soc.* **1982,** *104* (4), 1146.

8. Yu, J.; Xu, R., *Acc. Chem. Res.* **2003,** *36* (7), 481.

9. Lok, B. M.; Messina, C. A.; Patton, R. L.; Gajek, R. T.; Cannan, T. R.; Flanigen, E. M., *J. Am. Chem. Soc.* **1984,** *106* (20), 6092.

10. E. M. Flanigen, R. L. P., S. T. Wilson, Studies in Surface Science and Catalysis. *Elsevier* **1988,** *37*, 13.

11. Sastre, G.; Lewis, D. W.; Catlow, C. R. A., *J Phys. Chem. B.* **1997,** *101* (27), 5249.

12. Li, J.; Wei, Y.; Chen, J.; Tian, P.; Su, X.; Xu, S.; Qi, Y.; Wang, Q.; Zhou, Y.; He, Y.; Liu, Z., *J. Am. Chem. Soc.* **2011,** *134* (2), 836.

13. Palomino, M.; Corma, A.; Jorda, J. L.; Rey, F.; Valencia, S., *Chem. Commun.* **2012,** *48* (2), 215.

14. Association, S. C. o. t. I. Z. Framework Type RHO. http://izasc.ethz.ch/fmi/xsl/IZA-SC/ftc_fw.xsl?-db=Atlas_main&-lay=fw&-max=25&STC=RHO&-find (accessed June 10 2014).

15. Su, X.; Tian, P.; Li, J.; Zhang, Y.; Meng, S.; He, Y.; Fan, D.; Liu, Z., *Microporous Mesoporous Mater.* **2011,** *144* (1–3), 113.

16. Barrer, R. M.; Perry, G. S., *J. Chem. Soc.* **1961,** (0), 842.

17. Regev, O.; Cohen, Y.; Kehat, E.; Talmon, Y., *Zeolites* **1994,** *14* (5), 314.

18. Beck, J. S.; Vartuli, J. C.; Kennedy, G. J.; Kresge, C. T.; Roth, W. J.; Schramm, S. E., *Chem. Mater.* **1994,** *6* (10), 1816.

19. Sastre, G.; Lewis, D. W.; Catlow, C. R. A., *J. Phys. Chem.* **1996,** *100* (16), 6722.

20. Xu, L.; Du, A.; Wei, Y.; Wang, Y.; Yu, Z.; He, Y.; Zhang, X.; Liu, Z., *Microporous Mesoporous Mater.* **2008,** *115* (3), 332.

21. Askari, S.; Halladj, R., *Ultrason. Sonochem.* **2012,** *19* (3), 554.

22. Santen, R. A. V., Theory of Brønsted Acidity in Zeolites. In *Stud. Surf. Sci. Catal.*, Jansen, J.C.; Weitkamp, J., Eds. Elsevier: 1994; Vol. 273.

23. Zecchina, A.; Lamberti, C.; Bordiga, S., *Catal. Today* **1998,** *41* (1–3), 169.

24. Jeanvoine, Y.; Ángyán, J. G.; Kresse, G.; Hafner, J. *J. Chem. Phys. B.* **1998**, *102*, 5573.

25. Jiri Cejka, A. C., Stacey Jones, *Zeolites and Catalysis: synthesis, Reactions and Applications.* Wiley: NY, NY, 2010.

26. Cundy, C. S.; Cox, P. A., *Microporous Mesoporous Mater.* **2005,** *82* (1–2), 1.

27. Barrer, R. M.; Baynham, J. W.; Bultitude, F. W.; Meier, W. M., *J. Chem. Soc.* **1959,** (0), 195.

28. Lewis, D. W.; Catlow, C.; Thomas, J. M., *Faraday Discuss.* **1997,** *106* (0), 451.

29. Mullin, J. W., *Crystallisation, fourth ed.;* Butterworth Heine-mann: Oxford. 2001

30. Kacirek, H.; Lechert, H. *J. Phys. Chem.* **1976**, 80, 1291.

31. Cundy, C. S.; Henty, M. S.; Plaisted, R. J., *Zeolites* **1995,** *15* (4), 353

32. Kossel, W., *Annln. Phys.* **1934,** *21*, 457.

33. Pound, J. L. a. G. M., *J. Chem. Phys.* **1962,** *36* (8).

34. M. Matsukata, M. O., T. Osaki, P.R.H.R. Rao, M. Nomura, E. Kikuchi, , *Top. Catal.* **1999,** *9*, 77.

35. Gittleman, C. S.; Lee, S. S.; Bell, A. T.; Radke, C. J., *Microporous Mater.* **1995,** *3* (4–5), 511.

36. (a) Matsukata, M.; Ogura, M.; Osaki, T.; Hari Prasad Rao, P.; Nomura, M.; Kikuchi, E., *Top. Catal.* **1999,** *9* (1-2), 77; (b) Yang Na, Y. M., Wang Yimeng, *Prog. Chem.* **2012,** *24* (0203), 253.

37. Thoma, S. G.; Nenoff, T. M., *Microporous Mesoporous Mater.* **2000,** *41* (1–3), 295.

38. Li, H.; Eddaoudi, M.; O'Keeffe, M.; Yaghi, O. M., *Nature* **1999,** *402* (6759), 276.

39. Loiseau, T.; Serre, C.; Huguenard, C.; Fink, G.; Taulelle, F.; Henry, M.; Bataille, T.; Férey, G., *Chem. Eur. J.* **2004,** *10* (6), 1373.

40. Tranchemontagne, D. J.; Mendoza-Cortes, J. L.; O'Keeffe, M.; Yaghi, O. M., *Chem. Soc. Rev.* **2009,** *38* (5), 1257.

41. Janiak, C.; Vieth, J. K., *New J. Chem.* **2010,** *34* (11), 2366.

42. Stavitski, E.; Pidko, E. A.; Couck, S.; Remy, T.; Hensen, E. J. M.; Weckhuysen, B. M.; Denayer, J.; Gascon, J.; Kapteijn, F., *Langmuir* **2011,** *27* (7), 3970.

43 Volkringer, C.; Meddouri, M.; Loiseau, T.; Guillou, N.; Marrot, J. r. m.; Férey, G. r.; Haouas, M.; Taulelle, F.; Audebrand, N.; Latroche, M., *Inorg. Chem.* **2008,** *47* (24), 11892.

44. Seoane, B.; Téllez, C.; Coronas, J.; Staudt, C., *Sep. Purif. Technol.* **2013,** *111* (0), 72-81.

45. Liu, Y.; Her, J.-H.; Dailly, A.; Ramirez-Cuesta, A. J.; Neumann, D. A.; Brown, C. M., *J. Am. Chem. Soc.* **2008,** *130* (35), 11813.

46. Cowley, E. G., *Nature* **1951,** *168* (4277), 705.

47. Barton, D. H. R., *Experientia* **1950,** *6* (8), 316.

48. Carey, F. A., *Organic Chemistry.* 8th ed.; McGraw-Hill: New York, 2011.

49. Fryhle, T. W. G. S. a. C. B., *Organic Chemistry*. 9th ed.; John Wiley & Sons: Hoboken, NJ, 2008.

50. Ward EM, R. A., Suruda A, *Am. J. Ind. Med.* **1996,** *30* (2), 225.

51. Lews, R. J. *Sax's Dangerous Properties of Industrial Materials*; 9 ed.; Van Nostrand Reinhold: NY, NY, 1996

Chapter 2

Experimental

2.1 Characterization Techniques for Crystallization of Microporous Materials

Ideally, to characterize microporous materials, single crystal X-ray diffraction (XRD) would be employed. However, this requires suitable crystal growth which is not always possible depending on the system.[1] To determine long range and short range structure a variety of techniques can be employed. In this study, powder X-ray diffraction (PXRD) is used to determine long range order, while solid-state nuclear magnetic resonance (SSNMR) experiments are utilized to determine the short range order and the local environment about target nuclei.[2,3]

2.1.1 Powder X-Ray Diffraction

The diffraction of X-rays on the lattice of a crystalline material causes Bragg reflections. Bragg reflections are the radial distribution in reciprocal space of the intensity of coherently scattered radiation from a given set of planes.[4] Bragg reflections must obey Bragg's law (Figure 2.1.1) which states that reflections from discrete parallel planes interfere constructively which occurs when the phase shift is a multiple of 2π.[5] Bragg's law can be expressed as the formula

$$n\lambda = 2d\sin\theta \qquad (2.1)$$

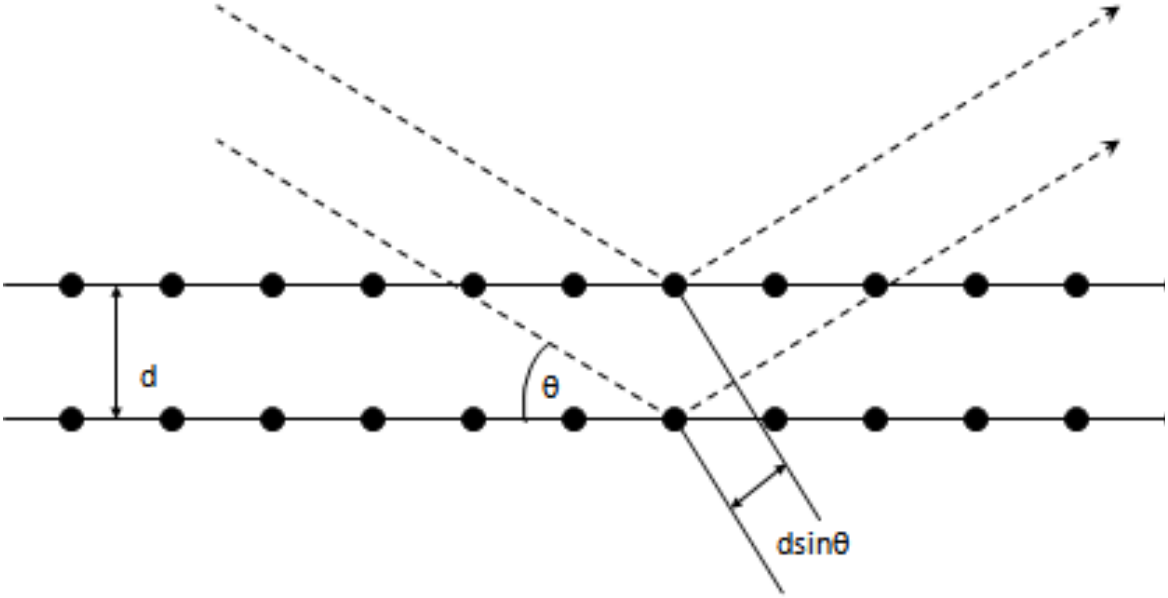

Figure 2.1 Bragg's Law, constructive interference occurs when nλ = dsinθ, equation (2.1)

where λ is the wavelength of the incident wavelength, d is the spacing between planes, and θ is the angle between the scattered planes and incident ray. When X-rays bombard a sample, constructive interference at certain angles occurs due to reflected waves from a different layer of the sample crystal lattice.[6] The constructive interference gives rise to an X-ray pattern that reveals information about the crystal structure.[6] The peak positions, intensities, and shapes in a PXRD pattern yield rich information about the crystal structure.

Peak position is determined by the unit cell parameters of the crystal structure. As a result of knowing the different peak positions of a diffraction pattern it is possible to determine what material is being investigated as different unit cells will give unique spectra. The only instrumental parameter that is used in determining peak position is the wavelength of the X-ray that impacts the sample. By changing the source of the X-ray it is possible to shift the reflections to either a higher or lower angle.[7]

Peak intensity gives information about the atomic parameters of the crystal structure, and can provide information about the orientation, absorption, and porosity of the sample. Peak intensity is dependent on many different factors such as the Lorentz-polarization factor which takes into account the finite size of a reciprocal lattice, the absorption factor which is both incident and diffracted X-rays that are absorbed by the material, and whether the powder orients randomly or has a preferred orientation.[7] Quantitatively peak intensity can be employed to determine concentrations of mixtures using the Rietveld method.[8] However, this is

unnecessary as our interest in PXRD for the SAPO is limited to identifying the crystal growth.

Finally, peak shape gives information about the crystallinity of the sample. The peak shape is defined by three major factors: instrument broadening, wavelength dispersion, and specimen function.[6] The physical properties of the sample such as grain size, strain, stress and crystallinity all play a role on the shape of the peak. For example, as crystals decrease in size the peak width will increase.[6]

Due to difficulties in performing quantitative analysis using these three variables, PXRD is used mainly for sample identification.[9] Each crystal lattice will have a corresponding PXRD pattern which can be thought of as a fingerprint, which is unique to the sample in question. Using PXRD it is possible to determine long-range-order of the system. The reflections of a PXRD pattern should sharpen and narrow as the sample becomes increasingly crystalline. In this study PXRD is used qualitatively to understand the crystallization process, at what pace the crystallization process occurs and finally through what intermediates the crystallization process takes place.

2.1.2 Solid-State Nuclear Magnetic Resonance

Nuclear magnetic resonance spectroscopy (NMR) has been one of the most commonly employed characterization techniques of molecules since the late 1960s.[10] It is necessary for a nucleus to possess a spin to be NMR active, hence, not all nuclei may be detected via NMR experiments. The spin of a nucleus is denoted in quantum terms by I. The nucleus will then have $2I + 1$ degenerate energy states.[11]

Spin is the intrinsic component of angular momentum, and does not depend on the trajectory of the nucleus. The spin in quantum mechanics takes on a magnitude, as well as a direction, which by convention is the z-axis (i.e, spin is a vector quantity). As nuclei with spin have angular momentum p, the maximum values of p for a nucleus is l. Any spinning nucleus has a magnetic moment μ which is orientated along the z-axis, and is proportional to the angular momentum ρ and gyromagnetic ratio γ.[12] When a nucleus is brought into an external magnetic field B_o, the discrete energy states will split in energy, which is the Zeeman interaction. While the Zeeman interaction is the largest in magnitude and is responsible for the initial splitting of energy levels, other interactions, which are perturbations of the Zeeman interaction, have a profound role in NMR spectra.[11] A full list of interactions, and their magnitudes for solids and liquids can be found in Table 2.1.

Table 2.1 NMR interactions.

Spin Interaction	Magnitude in Solids (Hz)	Magnitude in Liquids (Hz)
Zeeman	10^7-10^9	10^7-10^9
Quadrupolar	10^3-10^7	0
Dipolar	10^3-10^5	0
Chemical Shielding	10^2-10^5	10^2-10^5
J-Coupling	1-10^3	1-10^3

There is a significant difference between the magnitude of interactions in solution state NMR and liquid state NMR, as seen in Table 2.1. Many of these NMR interactions are anisotropic, or dependent on the orientation of the molecule with respect to the magnetic field. Therefore, in the liquid state, rapid molecular tumbling on the NMR timescale allows inter-spin vectors to randomly orient themselves in all directions. This phenomenon causes these anisotropic interactions to be averaged

to 0, while the chemical shielding and J-coupling are solely dependent on their isotropic values.[11]

In solids there is no molecular tumbling and each molecule has a set orientation with respect to the magnetic field. Each orientation of the molecule with respect to the magnetic field corresponds to a resonance at a slightly different frequency. The overall manifold of all resonances is often quite broad and of a low signal-to-noise ratio (S/N). While achieving high-resolution spectra in the solid state is difficult, it is possible by employing different techniques. For example, usually increasing the strength of the external magnetic field, employing magic-angle spinning (MAS), and using specialized pulse sequences have the ability to increase signal resolution.[12] In this study Al, Si, P, and C nuclei will be investigated as seen in Table 2.2.

Table 2.2 NMR parameters of this study.

Isotope	^{27}Al	^{29}Si	^{31}P	^{13}C
Spin (I)	5/2	1/2	1/2	1/2
Abundance (%)	100	4.7	100	1.1
Larmor Frequency @ 9.4 T (MHz)	104.30	79.46	161.92	100.5
Reference Material[13]	$Al(NO_3)_3$ (primary reference)	$C_{12}H_{36}Si_5$ (TTMSS, first peak) (secondary reference to TMS, first peak, +9.1 ppm)	$NH_4H_2PO_4$ (ADP) (secondary reference to H_3PO_4, +.81 ppm)	$C_{10}H_{16}$ (Adamantane, first peak) (secondary reference to TMS, +38.56 ppm)

2.1.2.1 Magic-Angle Spinning

By mimicking liquid state NMR it is possible to increase signal resolution in SSNMR. Certain chemical interactions, such as the dipole-dipole interaction, have an anisotropic property that is proportional to $(3\cos^2\theta - 1)$, where θ is the angle between the external magnetic field and the internuclear vector.[14] When all orientations are represented the average of the orientation dependence of the nuclear spin interaction is[14]

$$< 3\cos^2\theta - 1 > = \frac{1}{2}(3\cos^2\theta_r - 1)(3\cos^2\beta - 1) \qquad (2.2)$$

In solution state, $< 3\cos^2\theta - 1 >$ is reduced to zero by rapid molecular tumbling, whereas in solid state it is necessary to physically spin the sample at θ_r = 54.74° for the term $(3\cos^2\theta_r - 1)$ to become zero. θ_r is the angle between the magnetic field and the spinning axis. Spinning a sample at this angle to minimize these interactions is known as magic angle spinning (MAS) (Figure 2.2). MAS mimics molecular tumbling in the solid state and allows for the chemical shift and spin coupling interactions to be limited to their isotropic values, while the dipolar and 1st quadrupolar interactions are averaged to 0. The resulting NMR spectra will display line narrowing and increased resolution.[14] The sample must also be spinning at speeds that exceed the magnitude of anisotropy of the sample to mimic a solution sample which will produce solely a shift of the isotropic value. However, when spinning is slow, spinning sidebands are produced which radiate out from the isotropic shift at a distance of the spinning rate.[15]

2.1.2.2 Cross Polarization

Cross polarization (CP) is a tool used in SSNMR to enhance resolution, perform spectral editing and obtain information on physically proximate spins. CP uses dipolar coupling in order to obtain structural information of a solid sample. CP works by polarizing abundant spins and transferring the polarization to dilute spins. Usually the abundant spin chosen has a quick relaxation time, high gyromagnetic ratio. CP allows the recycle delay to be dependent on the short relaxation time of the abundant spin as opposed to the dilute spin.[15] The process of transferring polarization happens during the contact time when both radio frequency pulses are applied (Figure 2.3) to satisfy the Hartmann-Hahn condition:

$$\gamma_H B_1 = \gamma_X B_1 \tag{2.3}$$

Where B_1 is the strength of the radio frequency pulse and γ_H and γ_x are the larmor frequency of spin system H and X. This sets the radio frequency fields of the dilute spin to be equal to that of the abundant spin which allows for the transfer of polarization.[15] While the signal strength can be enhanced by a factor of γ_H/γ_x, there is still a dependence on internuclear distance. For example, nuclei from system H that are not near nuclei from system X might not appear in the spectra, while nuclei from system H that are closer to nuclei of system X will have a more enhanced signal. When conducting a MAS experiment the spinning rate must be lower than the dipolar interaction otherwise the magnetic dipole interaction averages to 0.[11]

Using SSNMR it is possible to probe the short-range order about individual nuclei within the framework. For example, it is possible to tell if SiO_4 is $Si(\text{-}O\text{-}Al)_1$,

$Si(-O-Al)_2$, $Si(-O-Al)_3$, or $Si(-O-Al)_4$ from the chemical shift.[15] This is a critical technique to understanding the route of how amorphous material progresses to a crystalline molecular sieve.

2.2 Raman Spectroscopy

Raman spectroscopy is a light scattering technique to study the vibrational modes of a molecule. For a vibrational mode of a molecule to be Raman active, it must have a non-zero derivative of the polarizability. Raman spectroscopy uses incident light in the visible spectrum, near the infrared (IR) spectrum or ultra-violet (UV) spectrum, to excite photons to a virtual energy state, which is lower than the next electronic state. Roughly 99.9% of excited photons will relax back to their ground energy state, which gives Rayleigh scattering. The other 0.1% will relax to either a higher or lower energy state, which gives Stokes and anti-Stokes shifts, respectively (Figure 2.4).[12] As the frequency of a Stokes shift is increased, the intensity increases and the ratio of intensity of a Stokes shift compared to an anti-Stokes shift intensifies due to a Boltzman distribution[16]

$$\frac{N}{N_o} = e^{\frac{-h\nu}{kT}} \tag{2.4}$$

Using character tables it is possible to determine if a vibrational mode will be Raman active or not. From an irreducible representation a Raman-active mode will contain the tensors that define polarizability (x^2, y^2, z^2, xy, xz, yz) and can be expressed as a matrix

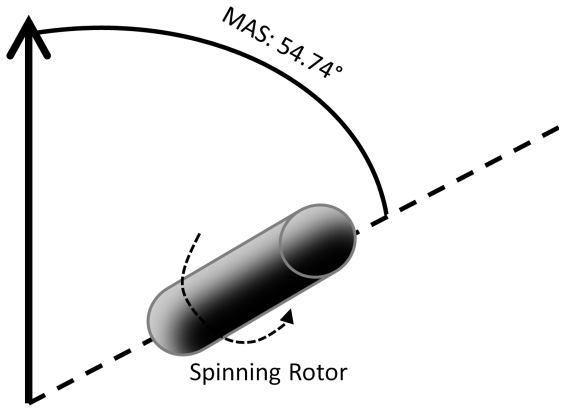

Figure 2.2 Magic Angle Spinning of a sample in SSNMR.

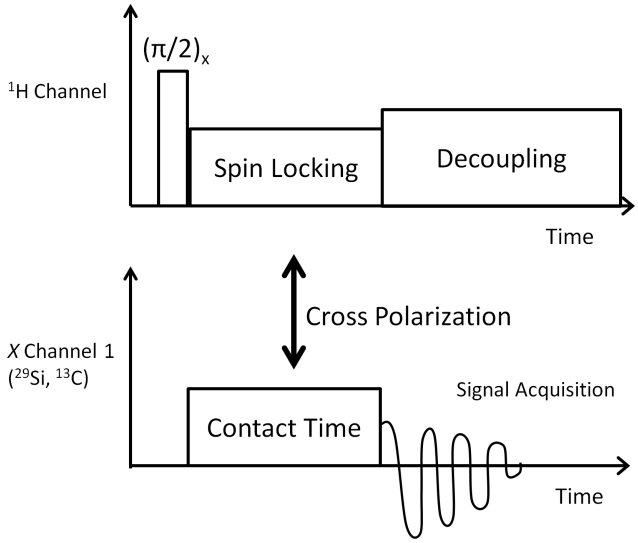

Figure 2.3 Cross polarization from frequency channel 1 to channel 2.

$$\begin{bmatrix} \mu_{ind(x)} \\ \mu_{ind(y)} \\ \mu_{ind(z)} \end{bmatrix} = \begin{bmatrix} \alpha_{xx} & \alpha_{xy} & \alpha_{xz} \\ \alpha_{yx} & \alpha_{yy} & \alpha_{yz} \\ \alpha_{zx} & \alpha_{zy} & \alpha_{zz} \end{bmatrix} \begin{bmatrix} E_x \\ E_y \\ E_z \end{bmatrix} \tag{2.5}$$

$$\mu_{ind} = \alpha \cdot E \tag{2.6}$$

Where μ_{ind} is the dipole moment, and E is the field strength of the radiation. If any of the previous tensor values change during a vibration, then the vibration is Raman active.[16] The larger the atom, the farther the outer electrons are from the core, increasing the polarizablity of a compound.[17] The largest limitation in Raman spectroscopy is the possibility of exciting a photon to the next electronic state causing fluorescence which can be minimized by employing Fourier transform Raman (FT-Raman) using a laser with a wavelength in the IR or UV region.[18]

FT-Raman in this study uses a 1064 nm $Nd3^{+}$-YAG laser, which has wavelength that is located in the IR region. Using a laser in the near-IR region it is possible to minimize photodecomposition, fluorescence, and provide greater frequency precision as opposed to lasers that use a 514 nm wavelength. One disadvantage to FT-Raman is that water absorbs wavelengths in the 1000 nm region, and this will create difficulties in obtaining spectra for aqueous solutions. Another disadvantage is that more expensive detectors and expensive instrumentation must be used due to the light scatter reaching wavelengths as high as 1700 nm.[12] In this study FT-Raman is employed to increase spectral resolution of rigid solids which have strong fluorescence properties.

Using Raman spectroscopy it is possible to visually see vibrational bands that belong to different conformers of the same molecule.[19] Studying the carbon-halogen bond it is possible to determine the percent conformation of different halocarbons and analyze the guest-host interactions taking place between MOFs and halocarbons.

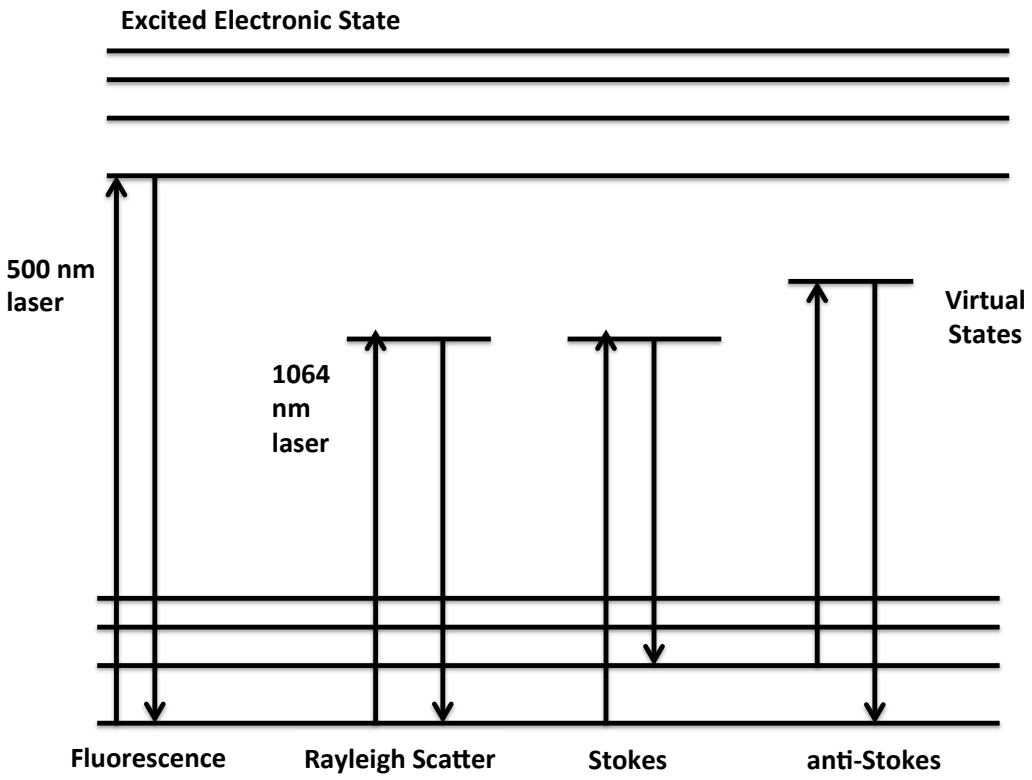

Figure 2.5 Excitation and relaxation of energy to produce Fluorescence, Raman Stokes, Raman Anti-Stokes and Rayleigh Scatter.

2.3 References for Chapter 2

1. Kanoo, P.; Gurunatha, K. L.; Maji, T. K. *J. Mater. Chem.* **2010**, *20*, 1322.

2. Cadars, S.; Brouwer, D. H.; Chmelka, B. F. *Phys. Chem. Chem. Phys.* **2009**, *11*, 1825.

3. Engelhardt, G.; Hunger, M.; Koller, H.; Weitkamp, J. In *Stud. Surf. Sci. Catal.*; J. Weitkamp, H. G. Karge, H. Pfeifer, W. Hölderich, Eds. **1994,** Elsevier 421-428

4. Langford, J. I.; Daniel, L. *Rep. Prog. Phys.* **1996**, *59*, 131.

5. Bragg, W. L. *Proc. Cam. Phil. Soc.* **1913**, *17*.

6. Fultz, B.; Howe, J. Transmission Electron Microscopy and Diffractometry of Materials; Springer Heidelberg: NY, 2013.

7. Zavalij, P.; Pecharsky, V. *Fundamentals of Powder Diffraction and Structural Characterization of Materials*; Springer Science + Business Media: NY, NY, 2005.

8. Dinnebier, R. E.; Billinge, S. J. L. *Powder Diffraction: Theory and Practice*; Royal Society of Chemistry Publishing: Cambridge, 2008.

9. van Koningsveld, H.; Bennett, J.; Structures and Structure Determination; Springer Heidelberg: NY, 1999.

10. Pekar, J. J. *Engineering in Medicine and Biology Magazine, IEEE* **2006**, *25*, 24.

11. Levitt, M. H. *Spin Dynamics: Basics of Nuclear Magnetic Resonance*; 2nd Edition ed.; Wiley: NY, NY 2008.

12. Skoog D.; Harris, F.; Crouch, S. *Principles of Instrumental Analysis*; 6th ed.; David Harris: Belmont, CA, 2007.

13. Harris, R. K.; Becker, E. D.; De Menezes, S. M. C.; Goodfellow, R.; Granger, P. *Pure Appl. Chem*. **2001** 73 1975

14. Duer, D. M. J. *Solid-State NMR Spectroscopy Principles and Applications*; Blackwell Science, 2002.

15. Mackenzie, K. J. D.; Smith, M. E. *Multinuclear Solid-State NMR of Inorganic Materials*; Elsevier Science Ltd.: Kidlington, Oxford, 2002

16. Grasselli, J.G.; Snaveyly, M.K.; Bulkin, B. J. *Chemical Applications of Raman Spectroscopy*; John Wiley & Sons: NY, 1981.

17. Eric Le Ru, Pablo Etchegoin. Principles of Surface-Enhanced Raman Spectroscopy: and related plasmonic effects; Elsevier B.V.: Amsterdam, 2009

18. Harris, D.C. *Symmetry and Spectroscopy; An Introduction to Vibrational and Electronic Spectroscopy*; Oxford University Press: New York, 1978.

19. Durig, J. R.; Costner, T. G.; Little, T. S.; Durig, D. T. *J. Phys.Chem* **1992**, *96*, 7194.

Chapter 3

INVESTIGATION INTO THE CRYSTALIZATION OF DNL-6 BY HYDROTHERMAL SYNTHESIS AND DRY-GEL CONVERSION METHODS

3.1 Introduction

Man-made microporous materials have been extensively studied since their discovery in 1862.[1] The main focuses of these studies have included adsorption, catalysis, and crystallization routes.[2-5] In order to study the crystallization of microporous materials using HTS, it is necessary to obtain the intermediates that exist between the initial amorphous gel and the final molecular sieve.[6] These intermediates are necessary to understand the crystallization pathway the sieve undergoes. However, due to the high pressure and high temperature reaction conditions, *in situ* characterization cannot be carried out easily.[7]

In order to slow down reaction speeds of HTS and obtain intermediates, DGC can be employed.[7-9] DGC slows down the reaction by preventing gel dissolution and associated high concentration gradients and mass transport limitations. While DGC can slow down the speed of the reaction, it is also possible that the same initial composition will lead to different morphologies depending on the synthetic method.[10] Therefore, it is first necessary to establish that both synthetic methods lead to formation of the desired microporous material.

DNL-6 is a SAPO with a RHO topology that was first discovered at Dalian National Laboratory.[11] Previous studies of DNL-6 include the characterization of DNL-6 and it's intermediates using hydrothermal methods, as well as studying its catalytic properties.[11,12] Current synthetic studies include the investigation of crystallization under hydrothermal and aminothermal conditions.[13] Currently three different synthetic pathways exist for DNL-6. By using different compositions of the initial gel it is possible to control the amount of silica incorporation into the framework.[13,14] DNL-6 has a reaction time of one day, and can be challenging to synthesize. Slightly varying the Si content or templating agent leads to the formation of CHA or a completely amorphous material.[11] CHA is a topology that contains CHA cages linked to double-6-rings. The CHA topology contains smaller pores and volume than the RHO topology. However, despite all the work that has gone into understanding the crystallization of microporous materials on a molecular level, the mechanisms are still not fully understood to this day. Using a different synthetic method to slow down the reaction may give insight into the crystallization process of DNL-6. This study will investigate and compare the DGC and HTS methods. By using the DGC method new intermediates may be obtained that do not exist under typical HTS. These intermediates will be studied by PXRD and SSNMR to allow further understanding into the formation of DNL-6.

3.2 Experimental

The experimental procedures for synthesizing and characterizing DNL-6 by HTS and DGC will be discussed in this section.

3.2.1 Experimental Synthesis

The hydrothermal synthesis of DNL-6 was performed according to literature procedures.[11] 4.02g (0.0197 mol) of aluminium isoproxide (Sigma Aldrich) was dissolved in 18 mL of water and was mixed with 1.78 g (0.0184 mol) of phosphoric acid (Caledon Labratory Chemicals) and left to stir for 15 minutes. After being stirred, 0.24 g (0.004 mol) of fumed silica, particle size 5 nm to 50 nm, (Caledon Labratory Chemicals) was slowly added and left to stir for 30 minutes. After stirring, 2.44g (0.0019 mol) of a 25% w/w solution of the surfactant, cetyltrimethylammonium chloride (CTACl), (Sigma Aldrich) was added, followed by 1.44 g (0.0197 mol) of the SDA, diethylamine (DEA) (Alfa Aesar), and stirred for 2 hours. The final product was then placed inside a telfon container and put inside a stainless steel autoclave. The autoclave was heated inside an oven at 200°C for 24 hours to yield the final crystalline product. The SAPO was then washed repeatedly with water and methanol followed by calcination, in a furnace at 600°C for four hours.

The synthesis to create the dry-gel differs slightly from the hydrothermal route. After mixing DEA and CTACl, the gel was stirred for 5 hours followed by freeze-drying overnight. The resultant powder was then placed in a small teflon cup, which was put into a larger teflon container with 1.1 g of water at the bottom. The teflon container was placed in an autoclave and heated in an oven at 160°C for up to 10 days. The washing process was the same as in the hydrothermal route.

3.2.2 Characterization by Powder X-ray Diffraction

As none of the microporous materials in this study crystallize into a uniform single crystal, PXRD was used as a fingerprinting method to determine if the desired structure was synthesized. The PXRD patterns were acquired by a Rigaku diffractometer using Co Kα radiation (λ = 1.7902 Å). All the samples were scanned between 5° - 45° at a scan rate of 10°/min, with a 0.02° increment rate.

3.2.3 Characterization by Solid State Nuclear Magnetic Resonance

SSNMR spectra were acquired for four different nuclei, ^{27}Al, ^{31}P, ^{29}Si and ^{13}C. All spectra were acquired on a 9.4 T Varian Infinity Plus 400 spectrometer. Each sample was placed in a Varian ZrO_2 rotor and spun at the magic-angle with a spin rate of 8 kHz. ^{27}Al was referenced using 1 M $Al(NO_3)_3$ (δ_{iso} = 0.0 ppm).[15] ^{31}P was referenced using $NH_4H_2PO_4$ (secondary reference of 85% H_3PO_4, +.81 ppm). ^{29}Si was referenced using tetrakis(trimethylsilyl)-silane (TTMSS) (secondary of TMS, +9.1 ppm,). ^{13}C was referenced using adamantane (secondary of TMS, +38.56 ppm). TTMSS and adamantane both have two resonances, the first of which is used for referencing purpose. The resonance frequencies for ^{27}Al, ^{31}P, ^{29}Si and ^{13}C were 104.3, 79.46, 161.92, 100.5 MHz, respectively. ^{31}P SSNMR spectra were obtained using a recycle delay of 60 seconds (s) and a pulse tip angle of 45° with a pulse length of 1.83 μs. ^{27}Al SSNMR spectra were attained with a pulse delay of 1 s and a pulse tip angle of 90° with a pulse length of 1.10 μs. ^{29}Si SSNMR spectra were acquired with a pulse delay of 60 s and a pulse tip angle of 60°, a pulse length of 1.75 μs for the one-pulse experiment. The ^{29}Si CP experiments were run with a pulse

delay of 10 s, a pulse tip angle of 90°, and a pulse length of 5.50 μs with a contact time of .5 μs (^{1}H--> ^{29}Si CP). ^{13}C CP experiments were acquired with a pulse delay of 10 s, pulse angle of 90°, a pulse length of 5 μs, and a contact time of 3 μs (^{1}H--> ^{13}C CP).

3.3 Results and Discussion

This section will detail the data collected by PXRD and SSNMR.

3.3.1 Powder X-ray Diffraction

PXRD was predominantly used as a finger printing method for microporous materials, but information was also gained by analyzing the intermediate crystalline structures during the crystallization process. When looking at the crystallization stages of DNL-6 (Figure 3.1) under hydrothermal conditions and DGC (Figure 3.2) notable differences exist. The PXRD of the HTS sample, at one hour has no peaks present indicating that the gel is completely amorphous. The earliest peaks seen are at roughly 3 hours (h) after the reaction initiation. However, these peaks are extremely weak and hard to resolve. At 9.5 h more defined peaks start to appear at 2θ values of ~6°, ~9°, and 25° indicating that some long-range order is present in the structure. It is important to note that the peak at 6° is not part of the final powder pattern. This peak can be attributed to early layered phases that occur during the nucleation phase and slowly disappear as the crystals continue to grow until the layered intermediate no longer exists at 24 h (Appendix A, Figure A.1).[16] A full table of DNL-6 reflections of the synthesized sample compared to the predicted peak

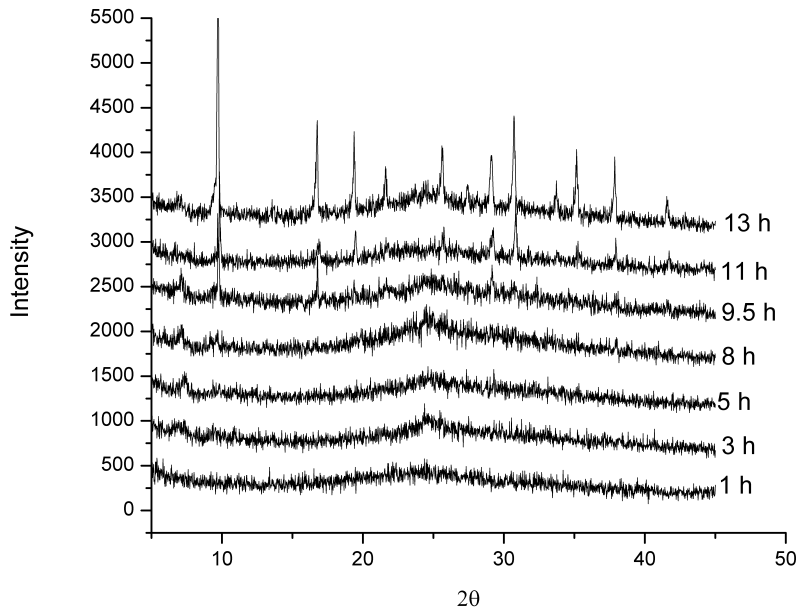

Figure 3.1 Powder X-ray diffraction patterns of intermediates of DNL-6 synthesized by the HTS method (Excluding final product due to intensity of reflections).

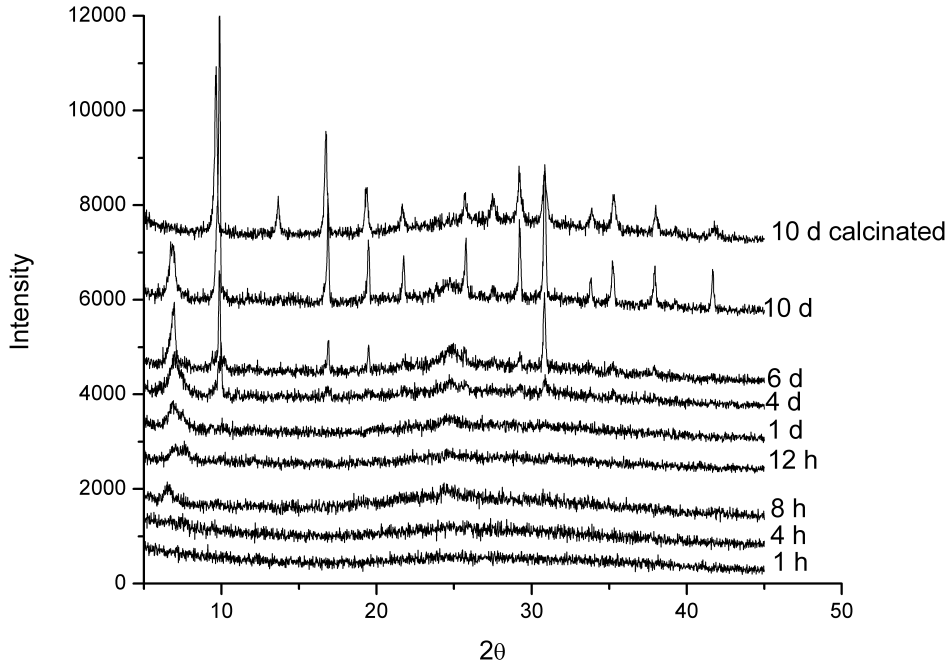

Figure 3.2 Powder X-ray diffraction patterns of intermediates of DNL-6 synthesized by the DGC method.

positions can be seen in Table 3.1. When viewing the PXRD pattern of the dry gel

Table 3.1 DNL-6 experimental reflections indexed to predicted DNL-6 reflections

Predicted DNL-6 Reflections(2θ)	Experimental DNL-6 Reflections (2θ)
9.7	9.8
13.7	13.6
16.8	16.8
19.5	19.5
21.8	21.7
23.9	23.8
25.9	25.8
27.7	27.5
29.4	29.2
31.1	30.9

crystallization (Figure 3.2), it can be seen that the initial gel before the reaction begins is completely amorphous. This information indicates that even after prolonged stirring, no long-range order exists without exposure to high temperatures and pressures. At 8 h, a reflection is first seen near 6°, as well as a broad reflection near 25°. Both these reflections continue to grow in intensity as the synthesis continues. These early peaks correlate to those seen in the hydrothermal method. This indicates that the first stages of induction and nucleation are similar between the two synthetic pathways under investigation. The first set of peaks that can be correlated to DNL-6 start to appear after four days (d). During the HTS the

early peaks that show crystal growth happen in a time frame of hours opposed to days, making this synthetic route roughly ten times slower than the hydrothermal method. The crystallinity continues to increase from 4 d to 10 d, until the final crystalline product from the DGC method exists. The early precursor peak at 6° remains after 10 d indicating that not all of the intermediate was converted to DNL-6 as seen with the HTS. As well, the final product of the DGC seems to have more amorphous material from the initial gel and semi-crystalline material than seen in the HTS. In order to remove the impurity and the amorphous material, the final product was subjected to calcination at 600 °C. As any impurities or precursor materials should have lower thermal stability than the SAPO, they should be able to be removed at high temperatures. Rerunning PXRD confirmed the disappearance of the low angle reflection indicating that solely DNL-6 remained.

The early reflection at 6° is still present in the final product. However, the peak decreases relative to the DNL-6 reflections as the duration of the synthesis increases. This indicates that the molecular sieve is formed through a precursor intermediate during the synthesis that eventually becomes DNL-6. This early intermediate phase has been seen previously in the crystallization of different $AlPO_4$s and SAPOs.[16-18] As the low angle peak is below 9°, the basal spacing of the semi-crystalline layered material are most likely larger than the LTA cages and may be mesoporous in nature. The low angle peak in the formation of $AlPO_4$-5 disappears after washing indicating it is held together by weak van der Waals forces and hydrogen bonding.[17] In the case of DNL-6 the reflections remain even after

washing. This indicates that T-O-T formation has begun during the formation of the semi-crystalline intermediate.

In previous work involving the synthesis of zeolite RHO, which contains no phosphorous, the PXRD patterns lack the low angle reflection seen in DNL-6.[19] $AlPO_4$s and SAPOs can easily form semi-crystalline layered intermediates due to the presence of phosphorous in the framework. Su et al. did not report a low angle peak in their hydrothermal study of DNL-6.[11] As the low angle reflection in the HTS is very weak, it is possible that in the study by Su et al. the signal to noise ratio (S/N) of the PXRD was not high enough to differentiate between noise and the weak reflection. However, the ^{31}P SSNMR spectra of Su et Al. does contain resonances at roughly -20 ppm, which correlates to the semi-crystalline intermediate which will be further discussed.

Using Scherrer's equation it is possible to estimate the crystal size of the crystallites obtained by both HTS and DGC.

$$\tau = \frac{K\lambda}{\beta cos\theta} \qquad 3.1$$

where τ is the crystallite size, K is the shape factor that can be estimated to be 0.92, β is the FWHH and θ is the Bragg angle. Using equation 3.1 the crystallize of the HTS crystallites is 69.39 Å , while that of the DGC is 69.31 Å. As the crystallite is the same from both methods it can be assumed they crystallize through the same pathway.

In the case of DNL-6, as seen from the PXRD, both the HTS and DGC synthesis follow the same pathway in the formation of the microporous material. As both syntheses follow the same crystallization pathway SSNMR experiments were run on

both the HTS and DGC intermediates to study the short-range order of the crystallization process.

3.3.2 Solid-State NMR

DNL-6 contains SiO_4, PO_4, and AlO_4 tetrahedra as the primary building blocks. Each atom has its own distinct chemical shift depending on its local environment. For example, Si may have a different chemical shift depending on the number of Al atoms in its coordination sphere. The Al atoms change the chemical shift due to the nuclear shielding effect of each additional atom. With this knowledge, it is possible to deduce the silicon incorporation mechanism. It is also possible to determine how the phosphorous and aluminum start to bond before silicon substitution takes place. Using ^{13}C SSNMR it is also possible to investigate the role of the structure directing agent and the surfactant in the crystallization of DNL-6.

3.3.2.1 ^{31}P Magic Angle Spinning Solid-State NMR

The ^{31}P SSNMR spectra of the HTS product and intermediates (Figure 3.3) show that the initial gel composition exhibits a broad resonance located between 5 ppm and -45 ppm with a span of ~50 ppm, which is indicative of an amorphous local environment. This broad resonance is in contrast to the two relatively sharper resonances observed at 0 ppm and the other at roughly -19 ppm. This means that in the initial composition there are at least two distinct ordered local P environments with most of the long-range-ordered structure remaining disordered. After 3 h of heating, the resonance at 0 ppm disappears while the resonance at -19 ppm strengthens. While there is a defined peak at 3 h in the ^{31}P spectrum, the PXRD

pattern indicates that the sample is still lacking long-range order. The emergence of a defined resonance at 3 h implies that some P nuclei have a defined local environment indicating that the crystallinity of the sample has increased even though the HTS PXRD pattern shows no reflections at 3 h.

After 8 h, the emergence of a resonance at -29 ppm occurs. This resonance correlates to $P(-O-Al)_4$ of the fully crystalline product, and coincides with the emergence of DNL-6 reflections in the PXRD pattern.[16] As the resonance at -29 ppm continues to grow, the broad resonance between 5 ppm and -45 ppm and the resonance at -19 ppm of the layered intermediate decrease until 13 h. At 13 h, the resonance at -19 ppm in the ^{31}P SSNMR spectra and the 6° reflection in the PXRD pattern has completely disappeared. This supports the concept that the local P environment causing the -19 ppm resonance is indeed the intermediate that the DNL-6 crystallizes from. At 24 h the reaction continues to completion and the broad resonance decreases in intensity. The -29 ppm resonance increases in strength indicating that almost all of the phosphorous in the initial gel is now part of the framework.

When examining the ^{31}P MAS SSNMR spectra of the DGC method (Figure 3.4) there is a considerable difference between that of the HTS and the DGC. The 1 h spectrum for the DGC contains the same broad amorphous resonance as the HTS, however the resonances that exist at 0 ppm and -19 ppm differ. The dry-gel has a slightly more defined resonance at 0 ppm but almost no resonance at -19 ppm. The lack of resonance at -19 ppm indicates that water may play a significant role in

forming the layered intermediate. After 4 h, resonances are visible at both -1 ppm and -20 ppm, indicating that the intermediate compound has started to form a local environment around the P nuclei. The resonance at -19 ppm continues to increase in signal strength over a four-day period. Starting at 4 d a small resonance is visible at -30 ppm indicating the start of visible $P(-O-Al)_4$. The $P(-O-Al)_4$ resonance once again increases in intensity from 4 d to 10 d while the resonance at -19 ppm decreases. However, for the DGC method after 10 d there is still amorphous material and the intermediate remains present. This can further be seen in the PXRD as the reflection at 6° is still present after 10 d indicating the sample contains impurities.

At 5 h the HTS PXRD pattern has a reflection at 6°. It is likely that the -19 ppm resonance in the ^{31}P spectra and the PXRD reflection at 6° correspond to the same intermediate. The intermediate should not be as condensed as the final product, therefore the intermediate phosphorous should have a local environment of $P(-O-Al)_x$ where $x < 4$. In order to determine the second coordination sphere previous work was carried out using $^{13}P\{^{27}Al\}$TRAPDOR experiments.[20,21] TRAPDOR experiments use dipolar coupling to ascertain connectivity and spatial interactions between a quadrupole nuclei and a spin 1/2 nuclei.[22] In this case the decoupling nuclei must be a quadrupole.[22] These experiments showed that for a resonance near -18 ppm the second coordination sphere of phosphorous has three aluminum atoms. Each P site was further characterized using CP experiments and it was determined the -18 ppm resonance has a local environment of $P(-O-Al)_3(OH)$.[17] In the case of DNL-6 for both the HTS and DGC the intermediate phosphorous species is most likely $P(-O-Al)_3(OH)$ which is the reason the intermediate

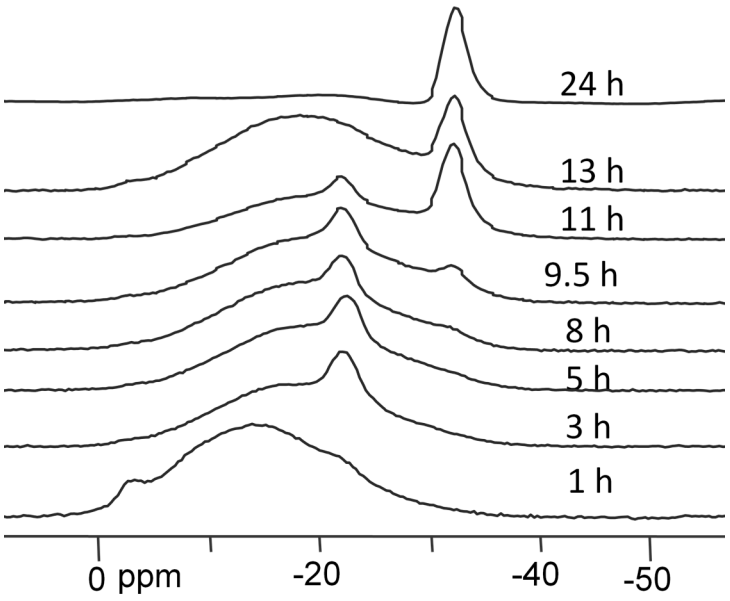

Figure 3.3 ^{31}P MAS SSNMR spectra of DNL-6 intermediates synthesized by HTS

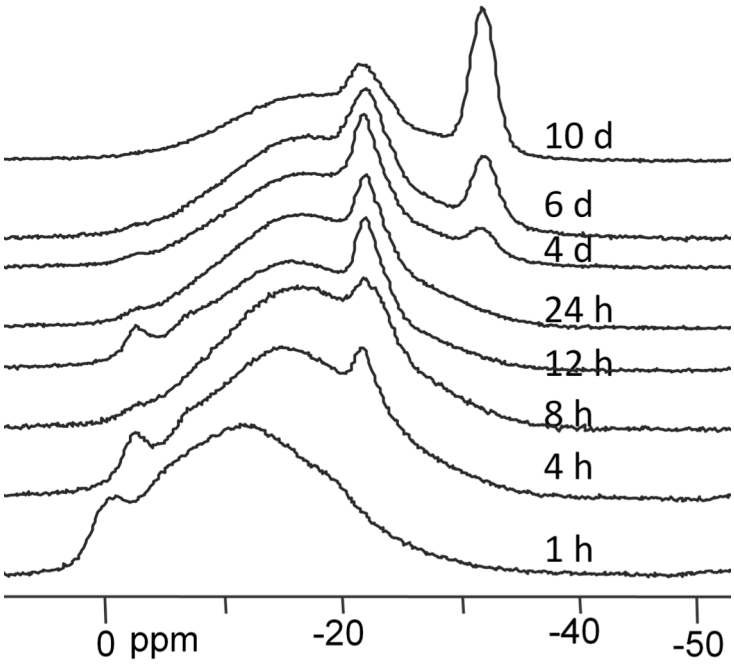

Figure 3.3 ^{31}P MAS SSNMR spectra of DNL-6 intermediates synthesized by DGC

was not seen in the crystallization of zeolite RHO. Even though the DGC is not in solution it is likely that phosphorous coordinates to hydroxyl atoms trapped in the dry-gel.

3.3.2.2 ^{27}Al Magic Angle Spinning Solid-State NMR

The ^{27}Al SSNMR spectra of the HTS crystallization of DNL-6 (Figure 3.5) display two defined resonances 1 h into the synthesis. The larger of the two resonances is centered at -4 ppm and corresponds to $Al(-O-P)_4(OH_2)_2$ in the amorphous material. This assignment agrees with previously published SSNMR studies of different SAPOs.[23] The second resonance is located at 44 ppm, which corresponds to $Al(-O-P)_4$, which would correspond to early aluminum species within the SAPO framework.[24] Between 3 h and 9.5 h the resonance at 44 ppm slightly increases while -4 ppm resonance does not change significantly. At 11 h, a resonance starts to emerge between the two resonances. The chemical shift of this new resonance is indicative of penta-coordinated aluminum $Al(-O-P)_4(OH_2)$.[25] The penta-coordinated aluminum corresponds to the aluminum in the SAPO that is coordinated to water found in the pores. As seen from the PXRD pattern (Figure 3.1) the early DNL-6 reflections start to be seen between 9 h and 11.5 h. The resonance continues to increase in intensity until 24 h, at which point the two original resonances can no longer be resolved. At 24 h the resonance at -4 ppm exists, indicating some amorphous aluminum is still present after DNL-6 is fully synthesized. The ^{27}Al SSNMR spectra of DNL-6 synthesized by the DGC method (Figure 3.6)

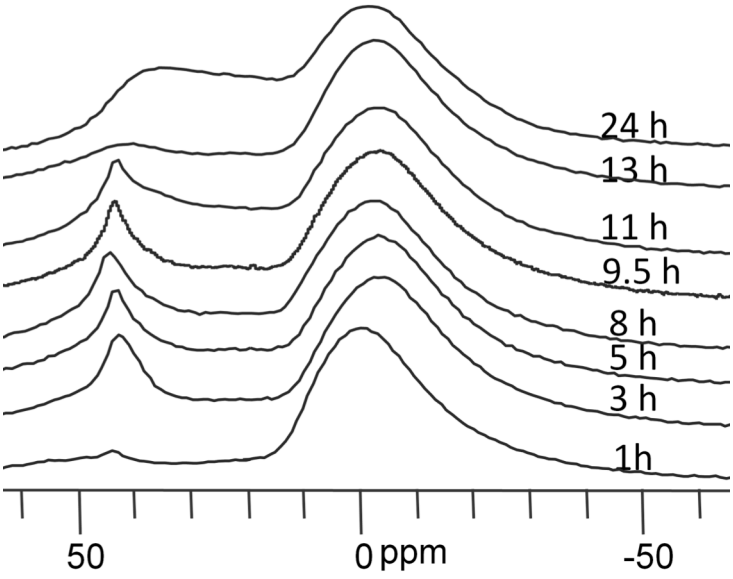

Figure 3.5 ^{27}Al MAS SSNMR spectra of DNL-6 intermediates synthesized by HTS method.

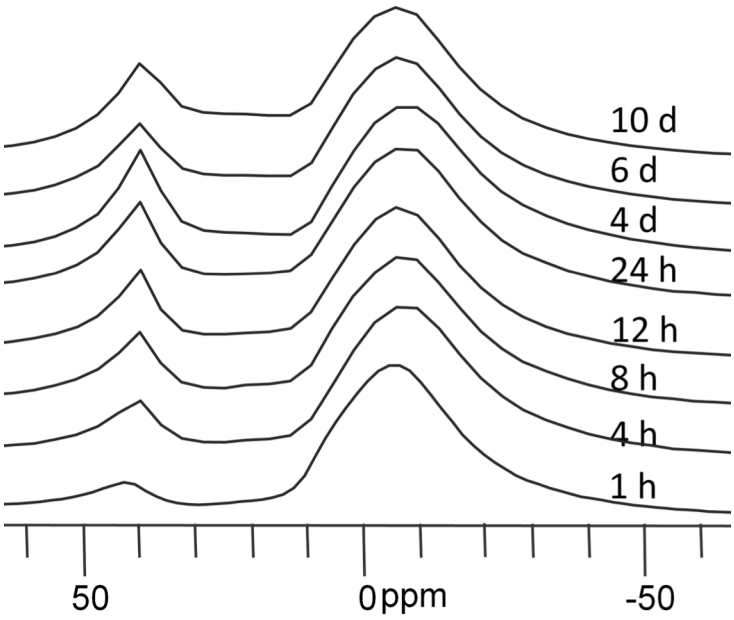

Figure 3.6 ^{27}Al MAS SSNMR spectra of DNL-6 intermediates synthesized by DGC.

In the DGC spectra, the same resonances are seen at the start of the reaction. The early resonances which exist at -5 ppm and 45 ppm are again indicative of $Al(-O-P)_4(OH_2)_2$ and $Al(-O-P)_4$, respectively. In this case H_2O has coordinated to the aluminum while aging the gel during stirring. As the reaction continues, the resonance at 45 ppm grows in intensity indicating that more aluminum is becoming tetrahedrally-coordinated within the framework. After 4 d, the PXRD pattern for the DGC shows DNL-6 reflections, however no resonance that belongs to penta-coordinated water exists. The lack of the penta-coordinated ^{27}Al resonance is due the reaction not taking place in the liquid phase.

3.3.2.3 ^{13}C Magic Angle Spinning Solid-State NMR

As carbon is not part of the SAPO framework, any carbon signal must be due to either the SDA or surfactant, hence only CP experiments were run. CTACl and DEA have distinctively different ^{13}C NMR chemical shifts, therefore are distinguishable.

From the HTS ^{13}C spectra (Figure 3.7), at 1 h, the only observed resonances correspond to the surfactant. From the ^{27}Al, ^{31}P, and PXRD spectra, it has been shown that at this point no DNL-6 exists. At 11 h, new resonances can be seen that belong to DEA and the timing of these resonances correspond to the first DNL-6 reflections in the PXRD spectra. Once the reaction is completed after 24 h, the intensity of the DEA resonances increase significantly indicating that DEA molecules are remaining in the pores at the end of the crystallization process. A stark contrast exists when examining the DGC method. The DGC ^{13}C spectra (Figure 3.8) show no

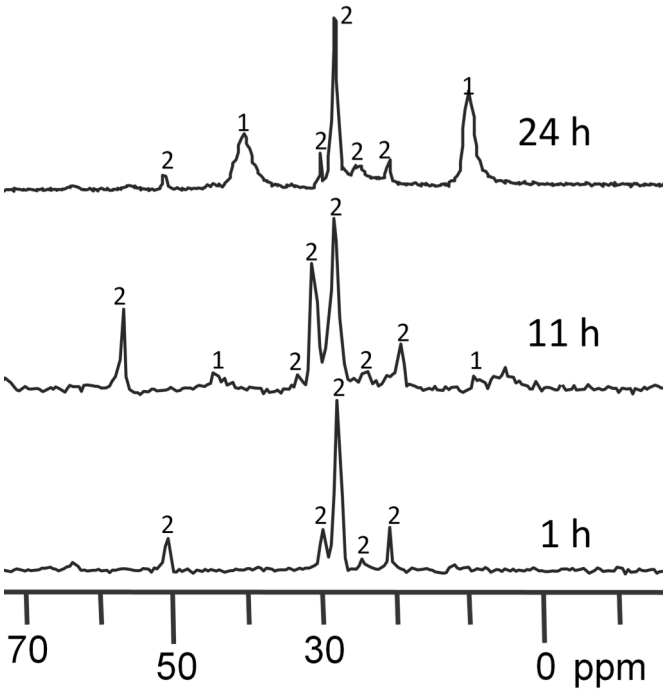

Figure 3.7 ^{13}C MAS CP SSNMR spectra of DNL-6 intermediates synthesized by HTS method (1 = DEA, 2 = CTACl).

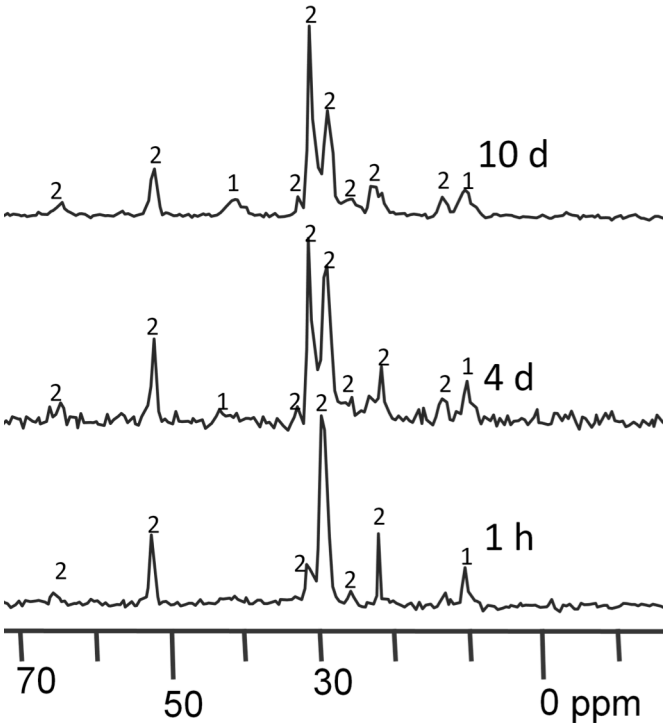

Figure 3.8 ^{13}C MAS CP SSNMR spectra of DNL-6 intermediates synthesized by DGC (1 = DEA, 2 = CTACl).

SDA resonances for the 1 h spectrum and a significantly smaller amount is seen for the intermediate at 4 d. While it is possible that more DEA is migrating from complete pore to incomplete pore, it is not supported by the weak PXRD reflections. After 10 d, instead of seeing a large increase in intensity of the DEA resonances, they remain relatively weak compared to that of the surfactant. The ^{13}C assignments of the ^{13}C spectra for DGC and HTS can be seen in Table 3.2. ChemBioDraw 13 was used to predict the chemical shifts of cetylmethylammonium chloride (CMACl) (Figure A.2).

Table 3.2 Chemical shifts of ^{13}C resonances of DNL-6 by HTS and DGC.

^{13}C peaks of HTS method (24 h) (ppm)	^{13}C peaks of DGC method (10 d) (ppm)	Assignment (ppm) CTACl[26] DEA[30]
11	11	DEA
N/A	14	CTACl
23	23	CTACl
26	27	CTACl
29	30	CTACl
32	32	CTACl
36	N/A	CMACl
43	42	DEA
54	54	CTACl
58	N/A	CMACl
67	66	CTACl

The layered intermediate most likely requires DEA molecules to be located between the basal planes in order to connect and form LTA cages. It is likely that DEA molecules are found within the LTA cages as the ^{13}C resonances correlate to the PXRD reflections of DNL-6. The small amount of DEA present in the 10 d ^{13}C spectra may be the cause of the layered intermediate remaining after the reaction goes to completion. It is possible that when aging or drying the dry-gel that DEA molecules evaporate due to the high volatility of the organic compound. Another possibility is that due to the lack of a liquid phase DEA molecules cannot migrate out of finished LTA cages in order to act as a SDA for new ones.

As seen from both the DGC method and the HTS method, the surfactant clearly remains 1 h into the synthetic process, long before any early DNL-6 peaks are visible in the PXRD patterns. This indicates that CTACl is located within the amorphous material, and is not soluble in water. Most likely the surfactant is being used as a SDA for the layered intermediate. In the early process of forming the ordered equilibrated gel the surfactant may be inside the ordered material.

Usually employing surfactants such as CTACl above the critical micelle concentration allows aggregation of the surfactant molecules into ordered self-assemblies.[26-28] While surfactants have been used in the synthesis of microporous materials, once the surfactants aggregate they are used in the synthesis of mesoporous materials such as MCM-41 and M41s.[26,27]

Recently, Huang et al. described how the use of surfactants in microporous materials is highly temperature dependent.[28] By using high enough temperatures to

break up the surfactant aggregates (160 °C), it is possible to obtain microporous materials from a gel that would create a mesoporous material at lower temperatures.[28] In the case of DNL-6, a low concentration of surfactant is employed at either 200 °C for the HTS or 160 °C for the DGC. These reaction conditions are sufficient enough to break the surfactant-surfactant interactions. It has been previously reported that CTACl can be found within the pores of the microporous material ZSM-5.[29] Therefore it is possible that CTACl is located in two positions. The first position that CTACl may be located is within multiple LTA cages with the head in one and the tail extending along either the a, b or c axis. The other possibility is that CTACl is located in the center cage where once again the head is located in one unit-cell and the tail extends to other unit-cells along the a, b or c axis. CTACl most likely exists in the center cage due to its presence in the early stages of crystallization before LTA cages are formed, and that DEA is most likely within the LTA cages.

In the ^{13}C spectra of the HTS method peaks that do not belong to CTACl or DEA exist. It has been previously reported that at high temperatures and pH greater than 11, CTACl will decompose into centene, cetyldimethylamine, and trimethylamine via Hoffman degradation.[26] These decomposition products can then act as the templating agents as seen in the synthesis of ZSM-35.[28] However, in the case of DNL-6, the pH of the gel prior to the reaction is 8, indicating that CTACl should not be decomposing and the single molecules of the surfactant should be acting as individual SDAs. Furthermore, it has previously been reported that the pH increases as aluminosilicate species condense as the reaction of SAPOs proceed.[28]

The peaks at 67 ppm and 58 ppm would be assigned to cetyltrimethylamine while the peaks at 54 ppm and 36 ppm would be assigned to cetylmethylamine (Figure A.4). Therefore in the case of DNL-6 HTS, the surfactant is decomposing, but retains a bulky hydrophobic tail and a hydrophilic head. These resonances are not present in the DGC method, most likely due to the lack of a solution phase. It is possible that the lack of decomposition of CTACl further slows down the reaction and prevents DNL-6 from forming.

Initially it was reported that without CTACl in solution the final product would be a mixture of CHA and RHO topologies, a majority which was CHA.[11] The lack of the large surfactant acting as a templating agent for the layered intermediate, leads to the formation of smaller CHA cages. More recently, it has been reported that DNL-6 can be synthesized without using a surfactant and by increasing the molar ratio of DEA in the initial gel.[13] By increasing the amount of DEA in the initial gel it is possible that 2-3 DEA molecules may be able to mimic the role of the surfactant (CTACl) as a templating agent.

By comparing the DGC method and the HTS method and using previously reported literature, it is possible to establish the role of both CTACl and DEA during the crystallization process. Individual CTACl molecules are necessary to form the semi-crystalline layered intermediate and are most likely located in the center cages extending through multiple unit-cells. The role of DEA would then be to form the LTA cages between the layered intermediate to form DNL-6. This would cause DEA to be located within the LTA cages.

3.3.2.4 ^{29}Si Magic Angle Spinning Solid-State NMR

^{29}Si SSNMR experiments were run using both a one-pulse experiment and a CP experiment. The CP spectra should increase S/N, but it will only show Si atoms that are in close proximity to H atoms.

^{29}Si SSNMR spectra of the HTS, acquired using one-pulse experiments (Figure 3.9), show no silicon at the start of the reaction. Since the silicon enters the framework through a substitution method, no resonance is anticipated since aluminum and phosphorous have not begun to form the RHO topology. After 11 h, a distinct resonance emerges at -90.5 ppm, which corresponds to $Si(-O-Al)_4$.[22] This peak indicates that the intermediates were formed solely through a SM2 mechanism, and Si is incorporated into the framework by replacing a P atom. At 24 h after the reaction has gone to completion, no other resonances have emerged, indicating that Si does indeed only incorporate through SM2 and no silicon islands are formed within the DNL-6 framework. In the case of the ^{29}Si CP MAS spectra (Figure 3.10) the same resonance is present at 24 h, except no resonance can be seen for the intermediate at 11 h. These CP experiments rely on hydrogen being in close proximity to Si. If there are no resonances, there must not be any acidic sites where a hydrogen atom has protonated the Si-O-Al linkage. This indicates that the addition of the proton is not immediate and a negatively charged framework exists in the crystallization process. The intensity of the resonance centered at -90.5 ppm at 11 h correlates to the emergence of the resonance in the ^{31}P spectra that corresponds to $P(O-Al)_4$ in the framework.

^{29}Si MAS SSNMR spectra of the DGC product acquired using one-pulse experiments (Figure 3.12) show a resonance at -90.3 ppm after 10 d. The 4 d intermediate shows no resonance indicating that the substitution of Si into the framework takes longer for the DGC method. Unlike the HTS method, even though the PXRD pattern and ^{31}P SSNMR spectra show that DNL-6 has started to form, there is no silicon entering the framework. As there is still only one resonance for the final product, Si must incorporate into the framework in the same SM2 fashion as the HTS, albeit at a slower rate. The Si incorporates into the framework slowly due to the fact that it does not incorporate into the intermediate phase seen between 3 h and 9.5 h. The Si only starts to replace P atoms in the framework once the framework of DNL-6 is formed. As the DNL-6 framework takes longer to form in the DGC method, results in the Si substitution into the framework taking longer. The spectra from the CP experiment (Figure 3.13) display a resonance only after 10 d. The resonance at 10 d indicates that no acidic sites have formed during the early stages of silicon incorporation.

3.4 Summary

The results of this study differ from previously published results regarding the HTS method. The previously published results indicate no presence of surfactant in ^{13}C SSNMR experiments.[11] However, they do report that CTACl is necessary in order to form DNL-6 with a molar ratio of .1:1 to DEA. As the surfactant seems to be necessary to form DNL-6, it can only be assumed that the surfactant plays a role in the formation of the SAPO framework.[11] As the temperature of the HTS far exceeds

the temperature required to break the aggregates, it is likely individual CTACl molecules are found within the larger LTA cages. The previously published paper also fails to identify the intermediate layered phase, however their ^{31}P spectra does show a resonance at roughly -19 ppm but fails to discuss its significance in the crystallization process.[11] Both this study and the study of Su et al. indicate that Si incorporates into the framework through SM2.[11] Using CP it is possible to ascertain the time period when the acidic sites form in the SAPO. Lastly the PXRD spectra of the previous study shows a full PXRD pattern corresponding to DNL-6 peaks at 3 h, which differs greatly from the reaction time determined in this study. While both studies follow the same general crystallization pathways, there are significant differences between DGC and HTS concerning the rate of the reaction and the semi-crystalline intermediate.

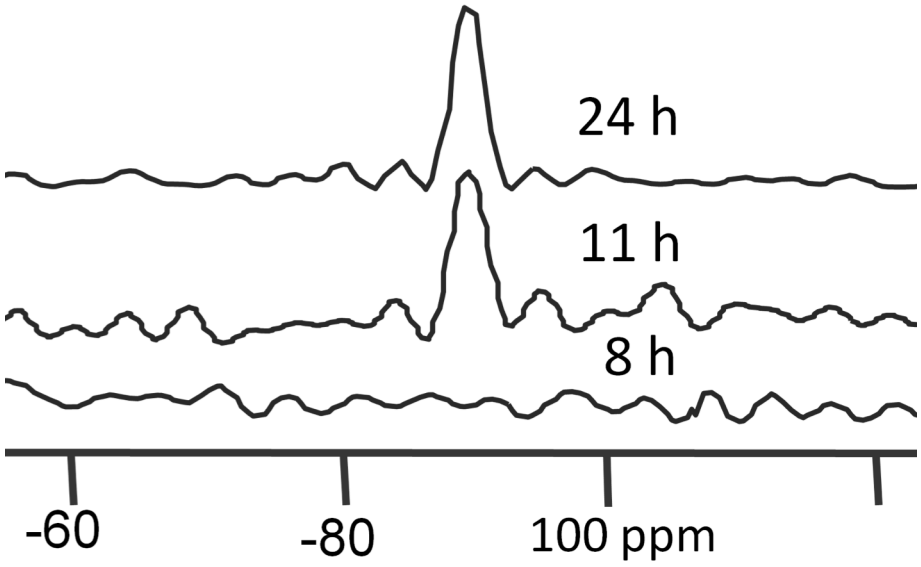

Figure 3.9 ^{29}Si MAS SSNMR spectra of DNL-6 intermediates by HTS.

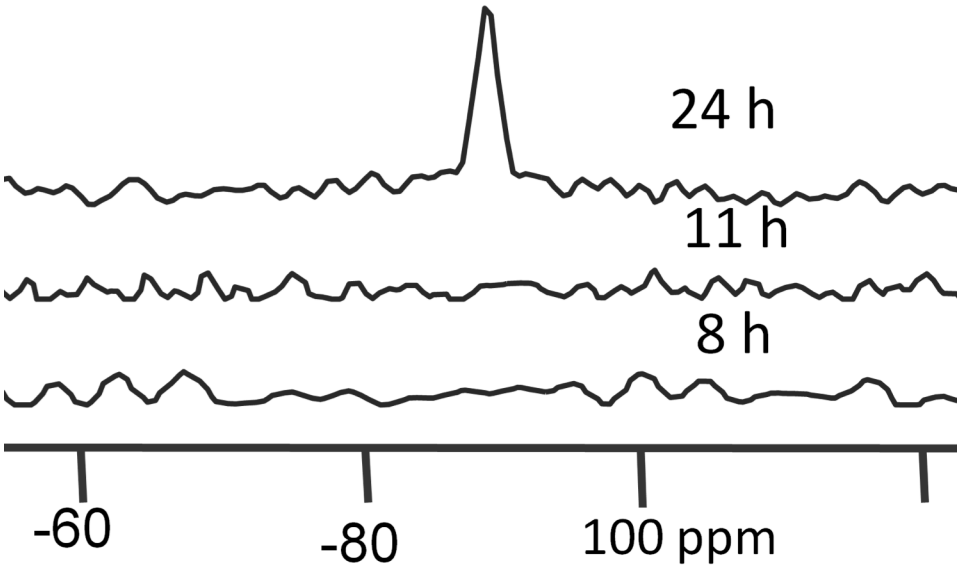

Figure 3.10 ^{29}Si MAS CP SSNMR spectra of DNL-6 intermediates by HTS.

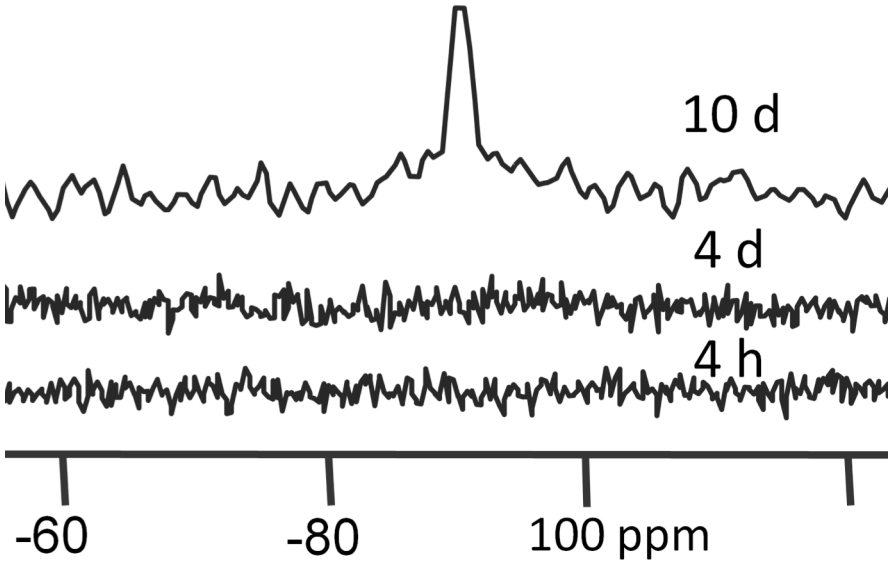

Figure 3.11 ^{13}C MAS SSNMR spectra of DNL-6 intermediates synthesized by DGC.

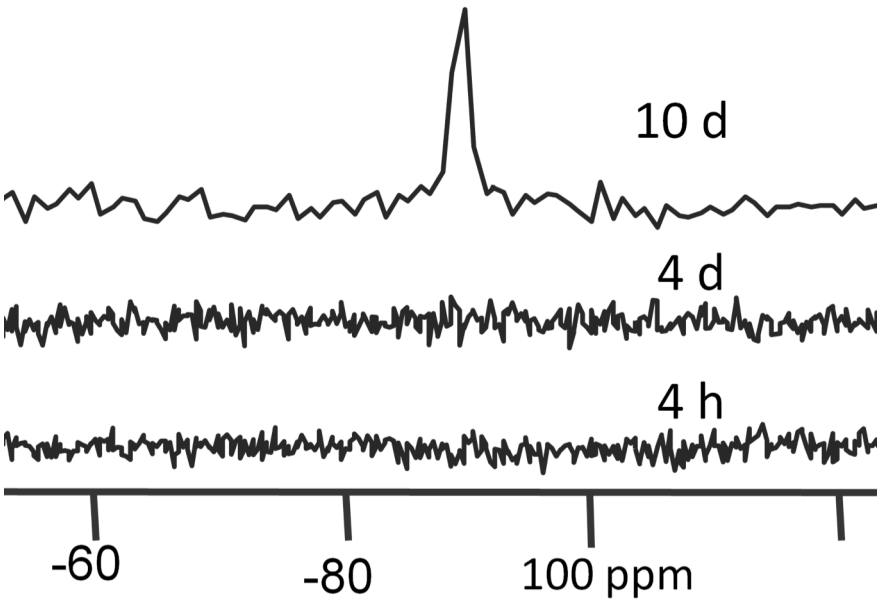

Figure 3.12 ^{13}C MAS CP SSNMR spectra of DNL-6 intermediates synthesized by DGC.

3.5 References for Chapter 3

1. Sainte-Claire Deville, H. *Comptes. Rendus Acad. Sci.* **1862**, *54*.

2. López-Fonseca, R.; Aranzabal, A.; Steltenpohl, P.; Gutiérrez-Ortiz, J. I.; González-Velasco, J. R. *Catal. Today* **2000**, *62*, 367.

3. Cundy, C. S.; Cox, P. A. *Microporous Mesoporous Mater.* **2005**, *82*, 1.

4. *Cubillas, P.; Anderson, W.M. Zeolites and Catalysis: synthesis, Reactions and Applications*; L. Cejka, S. Jones, Eds. Wiley, NY 2010.

5. Barrer, R. M.; Baynham, J. W.; Bultitude, F. W.; Meier, W. M. *J. Chem. Soc* **1959**, 195.

6. Zhang, L.; Bates, J.; Chen, D.; Nie, H.-Y.; Huang, Y. *J. Phys. Chem.* **2011**, *115*, 22309.

7. Xu, W.; Dong, J.; Li, J.; Li, J.; Wu, F. *J. Chem. Soc., Chem. Commun.* **1990**, 755.

8. Saha, S. K.; Waghmode, S. B.; Maekawa, H.; Komura, K.; Kubota, Y.; Sugi, Y.; Oumi, Y.; Sano, T. *Microporous Mesoporous Mater.* **2005**, *81*, 289.

9. Matsukata, M.; Ogura, M.; Osaki, T.; Hari Prasad Rao, P.; Nomura, M.; Kikuchi, E. *Top. Catal.* **1999**, *9*, 77.

10. Rao, P. R. H. P.; Ueyama, K.; Kikuchi, E.; Matsukata, M. *Chem. Lett.* **1998**, *27*, 311.

11. Su, X.; Tian, P.; Li, J.; Zhang, Y.; Meng, S.; He, Y.; Fan, D.; Liu, Z. *Microporous Mesoporous Mater.* **2011**, *144*, 113.

12. Li, J.; Wei, Y.; Chen, J.; Tian, P.; Su, X.; Xu, S.; Qi, Y.; Wang, Q.; Zhou, Y.; He, Y.; Liu, Z. *J. Am. Chem. Soc.* **2011**, *134*, 836.

13. Su, X.; Tian, P.; Fan, D.; Xia, Q.; Yang, Y.; Xu, S.; Zhang, L.; Zhang, Y.; Wang, D.; Liu, Z. *ChemSusChem* **2013**, *6*, 911.

14. Fan, D.; Tian, P.; Xu, S.; Xia, Q.; Su, X.; Zhang, L.; Zhang, Y.; He, Y.; Liu, Z. *J. Mater. Chem.* **2012**, *22*, 6568.

15. Harris, R. K. B., E. D.; De Menezes, S. M. C.; Goodfellow, R.; Granger, P. *Pure Appl. Chem.* **2001**, *73*.

16. MacIntosh, A. R.; Huang, Y. *Microporous Mesoporous Mater.* **2013**, *182*, 40.

17. Chen, B.; Kirby, C. W.; Huang, Y. *J. Phys Chem.* **2009**, *113*, 15868.

18. Chen, B.; Huang, Y. *J. Phys. Chem.* **2007**, *111*, 15236.

19. Araki, S.; Kiyohara, Y.; Tanaka, S.; Miyake, Y. *J. Colloid Interface Sci.* **2012**, *376*, 28.

20. Grey, C. P.; Veeman, W. S.; Vega, A. J. *J. Chem. Phys.* **1993**, *98*, 7711.

21. Grey, C. P.; Vega, A. J. *J. Am. Chem. Soc.* **1995**, *117*, 8232.

22. Mackenzie, K. J. D.; Smith, M. E. *Multinuclear Solid-State NMR of Inorganic Materials*; Elsevier Science Ltd.: Kidlington, Oxford, 2002

23. Blackwell, C. S.; Patton, R. L. *J. Phys. Chem.* **1988**, *92*, 3965.

24. Blackwell, C. S.; Patton, R. L. *J. Phys. Chem.* **1984**, *88*, 6135.

25. Alemany, L. B.; Kirker, G. W. *J. Am. Chem. Soc.* **1986**, *108*, 6158.

26. Trébosc, J.; Wiench, J. W.; Huh, S.; Lin, V. S. Y.; Pruski, M. *J. Am. Chem. Soc.* **2005**, *127*, 3057.

27. Kresge, C. T.; Leonowicz, M. E.; Roth, W. J.; Vartuli, J. C.; Beck, J. S. *Nature* **1992**, *359*, 710.

28. Huang, L.; Chen, X.; Li, Q. *J. Mater. Chem.* **2001**, *11*, 610.

29. Xu, D.; Feng, J.; Che, S. *Dalton Trans.* **2014**, *43*, 3612.

30. Lee, J. K.; Turrina, A.; Zhu, L.; Seo, S.; Zhang, D.; Cox, P. A.; Wright, P. A.; Qiu, S.; Hong, S. B. *Angew. Chem.* **2014**, *126*, 7610.

Chapter 4

Conformational Analysis of Halocarbons Adsorbed in Metal Organic Frameworks

4.1 Introduction

The conformations of halocarbons have been the target of investigation since the 1930s.[1] Multiple techniques such as NMR, vibrational spectroscopy, photoelectric spectroscopy, and theoretical calculations have been used to determine the conformations of different halocarbons.[2-5] For substituted alkanes such as 1,2-dichloroethane (DCE) (Figure 4.1), and 1-bromo-2-chloroethane (BCE) (Figure 4.2) the molecules exist in both the *trans* and *gauche* conformations. For substituted cyclic compounds such a 1-chlorocyclohexane (CCH) (Figure 4.3), the substituent can exist in either the equatorial or axial position.

Vibrational spectroscopy has been used to study the conformation of halocarbons as the C-Cl stretch for both the *trans* and *gauche* conformers can be easily resolved. To investigate that internal rotation was occurring for substituted alkanes, vibrational spectroscopy was employed at various temperatures.[1] It was determined that for DCE in the liquid and gas phase a mixture of both the *trans* and *gauche* conformer exist, whereas in the crystalline solid only the *trans* conformer exists. The conformeric mixture of DCE in the liquid and gas phases does not exist as a 50/50 mixture as the energy difference between the *trans* and *gauche* conformers is 5.02 kJ/mol. In the gas phase the *trans* population of DCE is favored and its population is 77%, whereas in the liquid phase the *trans* population of DCE is 35%.[6]

The phenomenon that stabilizes the *gauche* conformer in the liquid phase are polar interactions that exist between DCE and the solvent. DCE has a net dipole moment of 3.12 D in the *gauche* conformation, and a net dipole of 0 D in the *trans* conformation.[7] It has previously been proved that the *gauche* conformer is further stabilized in polar solvents by solvent-solute effects.[8]

In non-polar solvents such as CCl_4, it has been proven by theoretical calculations that there is still a preference for the *gauche* conformer. In the case of non-polar solvents, there is no solvent-solute effect taking place to stabilize the dipole found in the *gauche* conformation. However, the solvent can be seen as a dielectric medium that can have an induced dipole. This net dipole allows DCE to favor the *gauche* conformer to a larger extent than seen in the gas phase.[9] Raman spectroscopic studies have calculated the volume difference between the two conformers, showing that the *gauche* conformer's volume is 2.7 cm^3/mol smaller than that of the *trans* conformer.[3] BCE exhibits similar characteristics as DCE when considering conformation populations in the solid, liquid, and gas phase.

In the case of BCE, the *trans* population has been calculated to be 83% in the gaseous state and 54% in the liquid state.[10] In the solid phase BCE crystallizes solely into the *trans* conformer. BCE has a dipole of 2.5 D for the *gauche* conformer and has a slight dipole of 0.1 D for the *trans* conformer.[10] The shift of BCE's conformation population in the liquid and gas phases can be attributed to the same reasons as seen with DCE, where the *gauche* population is stabilized in the liquid phase by polar interactions. However, when compared to DCE the *trans* population is much

higher in the case of BCE. The higher population is credited to the weaker dipole moment of the *gauche* conformer, which weakens the dipole-dipole interactions with the solvent. In the case of BCE, the volume difference between the two conformers is only 2 cm^3/mol.[3]

The difference in dipoles and volume between BCE and DCE can be attributed to the exchange of a chlorine atom of DCE with a bromine to form BCE. The bromine is a larger atom, which prefers the trans conformer to minimize steric interactions. Bromine is also a less electronegative atom, which will give the *gauche* conformer of BCE a weaker dipole than DCE. The weaker dipole moment causes the *gauche* conformer of BCE to be less stabilized by polar solvents than DCE.

DCE and BCE have both been previously studied within the context of microporous materials. Previously the focus of study for DCE was limited to zeolites and the first studies included that of adsorption,[11,12] decomposition,[13] and catalytic effects.[14] The conformation of DCE within different zeolite frameworks was studied by Leech.[7] These studies showed when DCE is absorbed by different zeolites the *trans* population changes depending on the environment of the zeolite topology, the existence and nature of cations, and the Al:Si ratio.[7] There are currently few studies that investigate DCE and its interactions with MOFs. A study has been recently published investigating the adsorption isotherms, kinetics and desorption of DCE in MIL-101.[15] To the best of my knowledge, there are no studies investigating the conformation of DCE in MOFs.

The interactions of BCE with microporous materials have not been as thoroughly investigated as DCE. Current studies of BCE in microporous materials include adsorption/desorption in zeolites[11] and a conformational study using FT-Raman spectroscopy in zeolites by Wang.[10] Wang showed similar results to that of Leech in that BCE interacts strongly with polar frameworks to mimic liquid phase conformer populations, and minimally with non-polar frameworks to take on conformer populations that imitate the gas phase.[10] To the best of my knowledge no studies have been published that investigate BCE adsorbed in MOFs.

Previous work with monosubstituted cyclohexanes have studied the adsorption of CCH in zeolites by both ^{13}C SSNMR and FT-Raman spectroscopy.[7,16] The two studies have produced contradictory results. The SSNMR study concluded that the framework of a zeolite has no substantial effect on determining the conformer of CCH. The FT-Raman spectroscopy study concluded that by changing the framework of the zeolite, it is possible to control guest-host interactions. The FT-Raman conformational study concluded that completely siliceous frameworks stabilize the equatorial conformer, whereas the presence of a cation in the framework, as in zeolite Na-Y, prevents molecular motion as there is no change in population at low temperatures.[7]

Halogenated alicyclics do not behave the same way as simple alkane chains. The main interactions preventing the axial conformation in the alicyclic compound are van der Waals (vdW) forces. There are currently few studies that investigate halocarbons and their guest-host interactions with MOFs. As well, to my knowledge

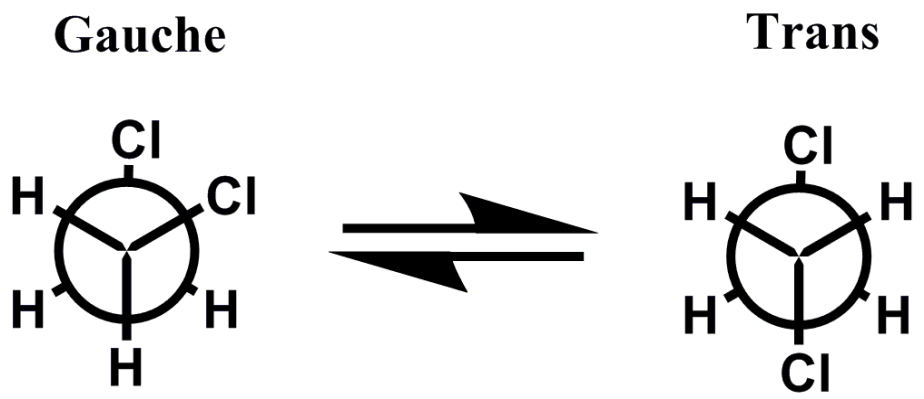

Figure 4.1 (left) DCE *gauche* conformation, (right) DCE *trans* conformation.

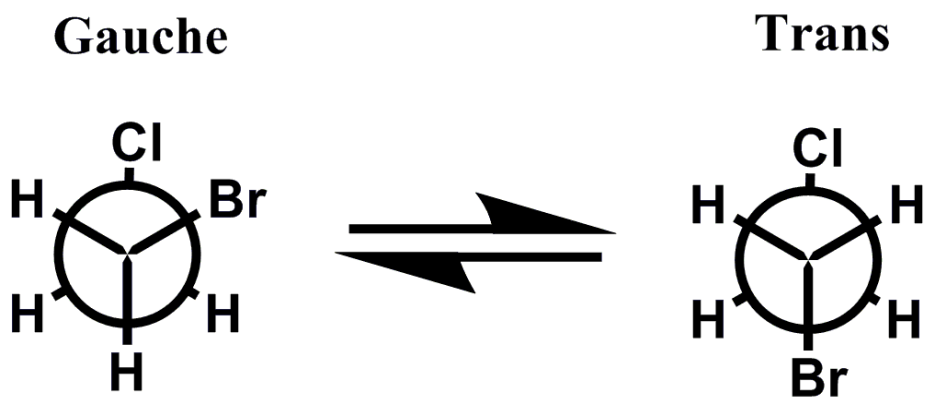

Figure 4.2 (left) BCE *gauche* conformation, (right) BCE *trans* conformation.

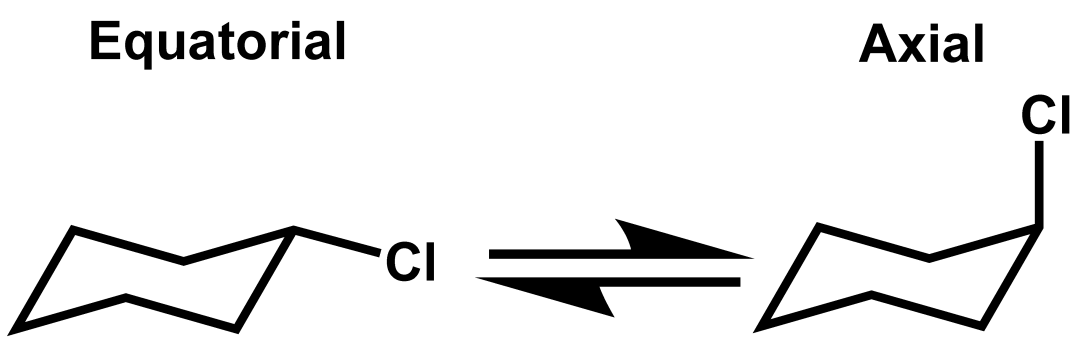

Figure 4.3 (left) CCH equatorial conformation, (right) CCH axial conformation.

no studies exist that investigate halocarbon conformation adsorbed into MOFs.

As halogenated hydrocarbons have many negative environmental effects, the storage and possible decomposition of these compounds is of interest.[17,18] Halocarbons are known for high toxicity and carcinogenic properties, for example DCE, a widely used solvent, has been classified as a possible carcinogen, causes chronic liver and kidney effects, and has moderate to acute toxicity levels from oral exposure or inhalation.[19] BCE, a pesticide, has moderate toxicity when inhaled and incineration leads to highly toxic halogen gas.[19] As of 2013, the long term toxicology of CCH has yet to be investigated, however, its short term toxicology includes possibly causing skin irritation and respiratory problems if inhaled. Incineration of halocarbons is known to give off toxic gases. A possible alternative is the storage of halocarbon waste. Using MOFs to store toxic halocarbons may allow for better storage capacities before safe disposal is possible. In order to investigate the possibility of storage, understanding the interactions of halocarbons in MOFs is necessary. This chapter presents the results of a conformational analysis of DCE, BCE, and CCH in different MOFs through FT-Raman spectroscopy to understand sorbent-sorbate interactions. The MOFs chosen for this study are MIL-53, MIL-53NH_2 and MIL-68. Each MOF has different properties that may affect the conformation of the halocarbons. For example, MIL-53 has a flexible framework,[20] MIL-68 has a rigid framework with two different pore sizes,[21] and MIL-53NH_2 has a flexible and polar framework.[22]

4.2 Experimental

MIL-53, MIL-68, and MIL-53NH_2 were all synthesized using previously published syntheses.[21,23,24]

MIL-53 was synthesized by mixing $Al(NO_3)_3 \cdot 9H_2O$ (Sigma Aldrich), BDC (Sigma Aldrich) in distilled water at a 2:1:160 ratio. After vigorous stirring the solution was placed in a Teflon container that was then moved into a stainless steel autoclave. The autoclave was then put into an oven for 72 hours at 220 °C. The product was then filtered and washed with distilled water and the structure was confirmed by using PXRD. The sample was then calcinated at 330 °C for 72 hours to eliminate any solvents in the pores. MIL-53 and MIL-53NH_2 were calcinated at 330 °C for 72 hours, while MIL-68 was calcinated at 250 °C for 24 hours.

To perform the loading, the sample was evacuated in a glass NMR tube under vacuum for 6 hours at 300 °C. The sample was then sealed using Teflon tape under vacuum, and the guest molecule of choice was loaded using a syringe followed by flame sealing the glass tube. The glass tube was then heated to 10 °C above the boiling point of the guest molecule overnight to allow the halocarbons to enter the pores. The temperatures for loading DCE (Sigma Aldrich), BCE (Sigma Aldrich), and CCH (Sigma Aldrich) were 95 °C, 117 °C, and 153 °C, respectively. The loading of all the samples in this study took place in this fashion. Table 4.1 gives the different synthetic conditions for MIL-53, MIL-68 and MIL-53NH_2. PXRD was used to ensure that each MOF was synthesized without impurities. As well, after loading PXRD was

used to investigate the shape adopted by MIL-53 and MIL-53NH_2, which have a flexible framework, and MIL-68,

Table 4.1 Synthesis parameters of different MOFs.

MOF	Metal Source (g)	Organic Linker (g)	Solvent (mL)	Temperature (°C)	Time (hours)
MIL-53[23]	$Al(NO_3)_3 \cdot 9H_2O$ 1.3	BDC 0.288	Water 10.00	220	72
MIL-68[21]	$In(NO_3)_3 \cdot 5H_2O$ 0.816	BDC 0.400	DMF 10.00	100	48
MIL-53NH_2[24]	$Al(NO_3)_3 \cdot 9H_2O$ 3.1	BDC-NH_2 1.5	Water 23.00	150	5

which has a rigid framework. The PXRD experiments were carried out by using a Rigaku diffractometer using Co Kα radiation (λ = 1.7902 Å). All the samples were scanned between 5° - 45° at a scan rate of 10°/min, with a 0.02° increment rate.

In order to determine the maximum loading of each sample thermal gravimetric analysis (TGA) was used. TGA experiments were performed using a Mettler Toledo TGA/SDTA 851e with a flow rate of N_2 of 60 mL/min. Each sample was heated from 298 K to 673 K at a rate of 10 K/min. The derivative of each TGA curve (DTG), was used to determine which molecules were inside or outside of the pores by determining the amount of peaks.

FT-Raman experiments were carried out on a Bruker RFS 100/S FT-Raman spectrometer equipped with a $Nd3^+$/YAG laser operating at the wavelength of 1064

nm and a liquid nitrogen-cooled Ge detector. The maximum laser power of the spectrometer was 500 mW. The strength of the laser at the sample varied with each system in order to maximize the signal, while minimizing the fluorescence of the sample. The laser strength ranged from 50 mW to 150 mW at the sample during the experiments. A constant laser power was used when collecting the variable temperature (VT) spectra. The resolution used for a majority of samples was 4 cm^{-1} with the exception of the DCE/MIL-53NH_2, BCE/MIL-53NH_2, and CCH/MIL-53 systems which used a resolution of 2 cm^{-1}. To conduct the VT experiments, a Bruker Eurotherm 800 series temperature control unit with an accuracy of +/- 1 °C was used.

4.3 Results & Discussion

The following will section will detail the data collected by FT-Raman spectroscopy, TGA and PXRD.

4.3.1 1,2-Dichloroethane

DCE is a disubsituated alkane chain that can adopt either a *trans* or *gauche* conformation. This study will probe the guest-host interactions of DCE with different MOFs using Raman Spectroscopy.

4.3.1.1 1,2-Dichloroethane/MIL-53(Al)

DCE was loaded into MIL-53, which is a flexible MOF, whose pore diameter changes depending on the guest molecule.[25] To confirm the maximum loading of DCE into the pores of MIL-53, TGA experiments were conducted. A full table of the maximum loadings of all systems determined by TGA can be seen in Table 4.2. When

evaluating the TGA curves (Figure 4.4) a distinct loss of weight was observed at 160°C. This temperature is higher than the boiling point of DCE of 84°C, suggesting that DCE is adsorbed within the pores. FT-Raman spectroscopy was performed on the DCE/MIL-53 system with maximum loading of 0.31 molecules/unit-cell to evaluate the conformation of DCE. When evaluating the spectra for DCE loaded into MIL-53, the largest peaks belong to the organic linkers of the MOF (Appendix B, Figure B.1). The only vibrations from DCE that give well-resolved peaks are the C-Cl peaks found in the region between 600 cm^{-1} and 800 cm^{-1} (Figure 4.5). A full table of the carbon-chlorine stretches found in the FT-Raman spectra from DCE loaded into MIL-53 can be found in Table 4.3. The assignment of all peaks can be found in the

Table 4.2 Maximum loading of investigated systems.

System	Maximum Loading (molecules/unit-cell)
DCE/MIL-53	0.31
DCE/MIL-68	1.69
DCE/MIL-53NH_2	0.64
BCE/MIL-53	0.12
BCE/MIL-68	1.57
BCE/MIL-53NH_2	0.50
CCH/MIL-53	0.12

supporting information (Table B.1). The two DCE conformers have different point groups and therefore different Raman spectra. DCE in its *trans* state has symmetry of C_{2h}, while DCE in its *gauche* state has symmetry of C_2. These two different point groups allow for the differentiation of the C-Cl peaks for the two conformers. Group theory predicts that the C_{2h} point group has nine Raman active vibrations, one of

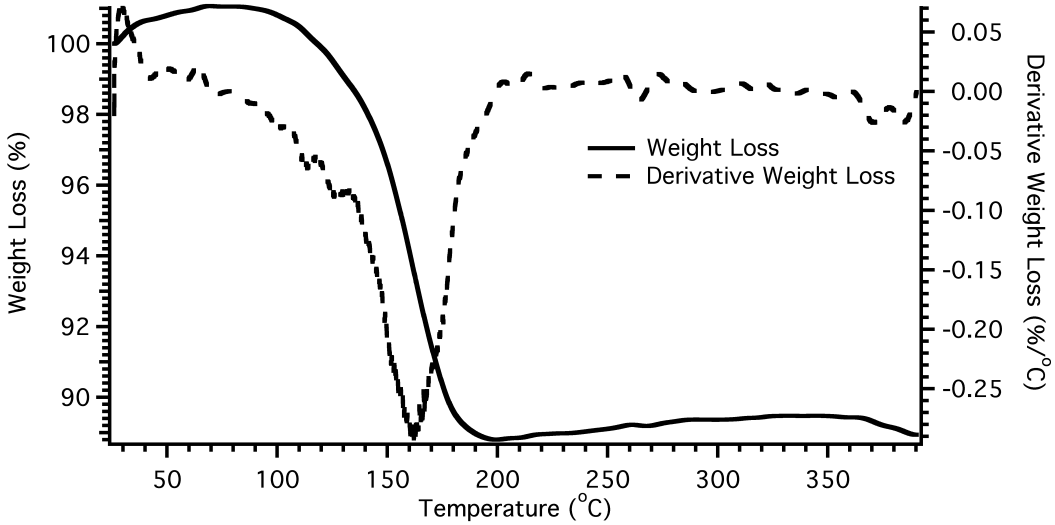

Figure 4.4 TGA curve and DTG curve of DCE/MIL-53 system.

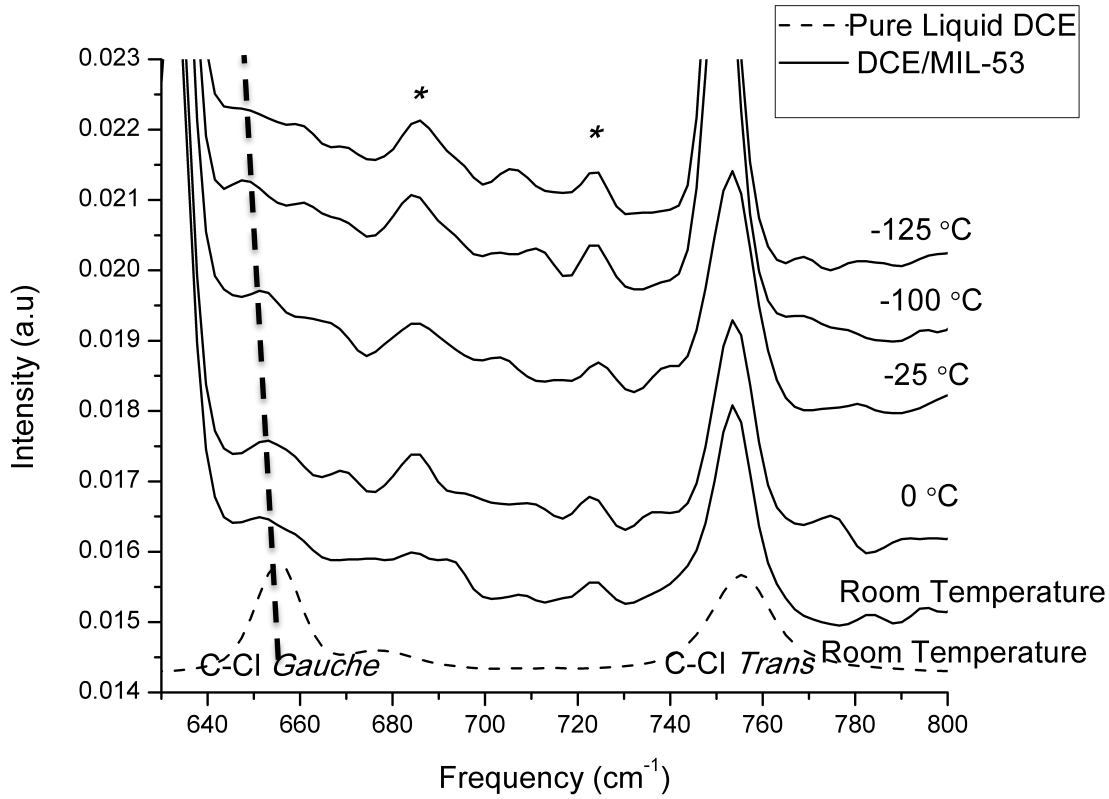

Figure 4.5 FT-Raman spectra at VT of DCE/MIL-53 system (*indicates framework).

which is a C-Cl stretching vibration.[26] For the *trans* conformer a Raman active mode that represents the C-Cl stretching vibration is assigned ν_5' and is located at 755 cm^{-1}.[6] The C_2 point group predicts 18 Raman active vibrations, with two of them being C-Cl stretching vibrations.[26] The Raman active mode, for the *gauche* C-Cl vibrations, gives rise to two peaks, ν_8' and ν_{17}' located at 675 cm^{-1} and 654 cm^{-1}, respectively.[6] The region of 600 cm^{-1} – 800 cm^{-1} of the FT-Raman spectrum of MIL-53 has very few peaks, which allows the C-Cl vibrational peaks to be well resolved. Therefore, it is possible to use the carbon-halogen stretches to quantify the *trans* and *gauche* populations of DCE in the MOF.

The formula for the intensity of a Raman band for a conformational conformer is as follows

$$I_i = c_i \sigma_i \tag{4.1}$$

Where I_i is the integrated area under the peak, c_i is the concentration of the conformation, and σ_i is the Raman scattering cross section for the conformation. Determining the Raman scattering cross section for a single conformer is extremely difficult. However, the Raman scattering ratio (σ_t/σ_g) has been previously calculated as 3.2.[27] The *trans* peak is well resolved and there is no overlap between the two *gauche* peaks. Only the larger, more defined *gauche* peak is used in determining the population.

Raman spectra were acquired and, using the previously mentioned formula and the calculated Raman cross-section ratio, the *trans* population of DCE in MIL-53 at 298K was calculated to be 73%. This value resembles that of the gas phase where

the *trans* population is 77% as opposed to the liquid phase where the *trans* population is 35%.[6] The high *trans* population can be attributed to the fact that MIL-53 has a non-polar and flexible framework that surrounds DCE molecules. Previous investigations of DCE conformations in solvents and dielectric mediums show that polar solvents are the largest contributor to an increase in the gauche population.[8] In non-polar mediums, two factors are predominant in stabilizing the *gauche* conformation, the dielectric value and the aromatic effect.[28] Previous studies have shown that a dielectric constant of $\kappa = 2$ or lower will not cause a significant induced dipole-dipole effect.[8] In the case of MIL-53, the organic ligand terephthalic acid ($\kappa = 1.5$) has too low of a dielectric constant to affect the conformation population.[29] Non-polar solvents with an aromatic ring are the cause of the "aromatic effect". Early hypotheses about the cause of the aromatic effect were that either a cavity formed around DCE causing spatial strain, the C-H of DCE interacts with the π system of the solvent or was the result of electrostatic effects.[28] However, it has been shown with glassy polystyrene that without reorientation of the aromatic planes around DCE the polarizability of benzene is not able to stabilize the *gauche* conformation.[28] In the case of MIL-53 the plane of the benzene rings of the organic linker are locked in place by the topology of the MOF. As reorientation cannot take place, the dominant interactions that can take place may include: the C-H orientating itself to interact with one aromatic system or vdW interactions.

When DCE is loaded into MIL-53 the C-Cl peaks (653, 675, 753 cm^{-1}) are near the same position as the peaks found in the liquid state (Table 4.3).[30] It has been

previously shown that it is the C-H bond of dichloromethane that interacts with the aromatic plane of the solvent.[31] The lack of red-shift or blue-shift of the C-Cl

Table 4.3 Peak assignments of Raman spectra of DCE/MIL-53, DCE/MIL-68.

DCE/MIL-53 (cm^{-1})	DCE/MIL-68 (cm^{-1})	Assignment:[6]	Literature Value: DCE (Pure liquid)[6]
653	653	C-Cl (*gauche*)	654
675	672	C-Cl (*gauche*)	675
753	752	C-Cl (*trans*)	755

vibration, may be due to the C-H bond of DCE being the predominant vibration that interacts with the π system of the organic linker.[31] It is possible that the C-H interaction with the π system is the dominant effect in the system. However, due to the lack of reorientation of multiple aromatic rings the *trans* conformer remains the preferred conformer. When investigating the FT-Raman spectra of the system, it is not possible to resolve the C-H stretch of DCE due to overlap with BDC, and therefore it is difficult to say with certainty that this is the effect taking place.

The full width at half height (FWHH) of a Raman band can give information about the molecular dynamics of both free molecules and molecules adsorbed in porous materials.[7] At room temperature (RT), the FWHH of the *trans* C-Cl peak changes from 15 cm^{-1} as a free liquid to 10 cm^{-1} when loaded in MIL-53. This change indicates that the adsorbed DCE molecules still undergo motion within the pores but the molecular motion is more limited than within a pure liquid.

When cooling takes place the relative *trans* population of DCE in MIL-53 increases. The *trans* population goes from 73% at 298K to 90% at 173K. Temperature has an effect on the peak position of Raman bands in liquids and solids. In solids, thermal expansion assumes a red-shift from heating and a blue-shift from cooling.[32] In the case of liquids, this is not the case and whether a liquid will red-shift or blue-shift under cooling depends on a number of factors and is best determined by quantum chemical calculations.[33] The slight red-shift of the C-Cl *trans* peak is most likely due to the system having less thermal energy under cooling.

Previous studies have shown that the PXRD pattern of MIL-53 changes under cooling, indicating that it is possible for MIL-53 to undergo a phase change which may aid in increasing the C-H interaction with the π system.[34] The FWHH continues to decrease from 10 cm^{-1} to 7 cm^{-1} as temperature decreases, indicating the molecular motion of DCE becomes more limited. Using the VT specta it is possible to construct a van't Hoff plot to calculate the enthalpy difference of the two DCE conformers. A ΔH° of 4.2 kJ/mol was calculated for the MIL-53/DCE system. The enthalpy of all DCE/MOFs systems will be discussed further in the chapter.

4.3.1.2 1,2-Dichloroethane/MIL-68(In)

MIL-68 is an Indium-based MOF with two distinct pores. The smaller pore has a pore size of 7 Å, while the larger pore has a pore size of 16 Å.[21] Unlike MIL-53, MIL-68 is a rigid MOF and its shape and pore sizes are not dependent on the guest molecule. After DCE was loaded into MIL-68, TGA (Figure 4.6) was conducted to determine the maximum loading, which is 1.69 molecules/unit cell. Attempts were

made to distinguish DCE in the two different pores. If it were feasible to distinguish the loading level, it would be possible to investigate the populations of the DCE conformers in only the larger pores. If DCE was loaded only into the larger pores it may give insight into whether DCE molecules in the small pores can interact with one another. However, it was not possible to distinguish the DCE molecules in both pores by TGA, as seen from the single peak in the TGA spectrum, and therefore it was not possible to investigate the population of each conformer at different loadings. Consequently, only the maximum loading is investigated in this study.

The FT-Raman spectra for the DCE/MIL-68 (Figure 4.7) system are comparable to the DCE/MIL-53 system. The signal produced by the BDC organic linker in the DCE/MIL-68 system dominates the spectra (Figure B.2). The full assignments of the peaks can be seen in the supporting information (Table B.1). The C-Cl vibration assignments can be found in Table 4.3. The region between 600 cm^{-1} and 800 cm^{-1} of the FT-Raman spectra of MIL-68 does not exhibit any strong peaks and therefore it is possible to investigate the conformational properties of DCE in MIL-68. Using formula (4.1) and the same Raman scattering cross section of 3.2, the *trans* population of the DCE/MIL-68 system at 298K was calculated to be 48%. The peak position of the ν_5' and ν_8' peaks for DCE in MIL-68 again closely resemble that of the liquid phase and minimal red-shift occurred when compared to the FT-Raman spectra of pure liquid DCE. The lack of significant shift in the peak position once again indicates that it is likely that the C-H bond of DCE is interacting with the π system of the organic linker. In the DCE/MIL-68 system, the *trans* population

resembles that of DCE in the liquid phase more than that of DCE in the gas phase. In the case of DCE/MIL-68, no reorientation of the π system is possible to permit the aromatic effect to stabilize the *gauche* conformer. The small pores in the system may be responsible for the increase in the *gauche* population, due to the strength of the *gauche* dipole of DCE. Two DCE molecules must only be within 12 Å and 15 Å to be stabilized by a neighboring DCE molecule.[9] In the case of MIL-68 the small pores only have a diameter of 7 Å, which can allow the DCE molecules to influence the conformation of one another. The FWHH in the case of the DCE/MIL-68 system is 13 cm^{-1}, which is larger than the 11.2 cm^{-1} of DCE/MIL-53, but still smaller then the liquid state of DCE, which is 15 cm^{-1}. However, as it was not possible to run the experiment with only DCE in the larger pores, it is difficult to distinguish the movement of DCE in each pore individually.

At 173 K there is not as much of an increase in the *trans* population for the DCE/MIL-68 system versus the DCE/MIL-53 system. The *trans* population increases from 48% to 68%. As thermal energy is removed from the system under cooling, DCE will adopt the more energetically stable conformation, which is the *trans* conformation. Due to the stabilizing effects of the DCE neighboring molecules the energy difference between the *gauche* and the *trans* conformations has decreased. The decrease in energy is the reason the *trans* population does not mimic that seen in the DCE/MIL-53 system. The FWHH of the *trans* peak decreases from 13 cm^{-1} to 11 cm^{-1} at 173 K. The drop in the FWHH shows that the motion of DCE has become more limited. Upon cooling, there is a 4 cm^{-1} red-shift of the C-Cl peak. The most likely causes of the red-shift and decrease in FWHH are due to the system having

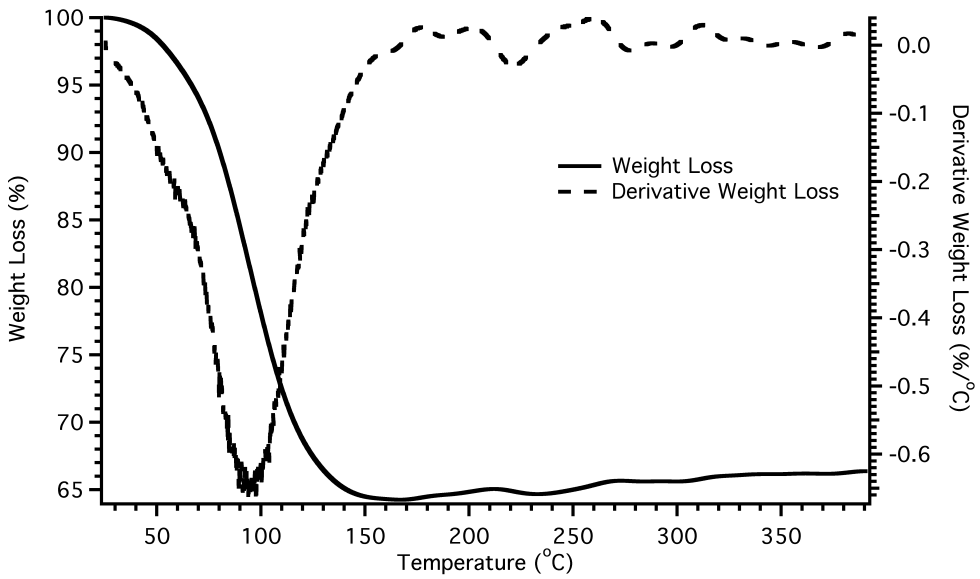

Figure 4.6 TGA curve and DTG curves of DCE/MIL-68 system.

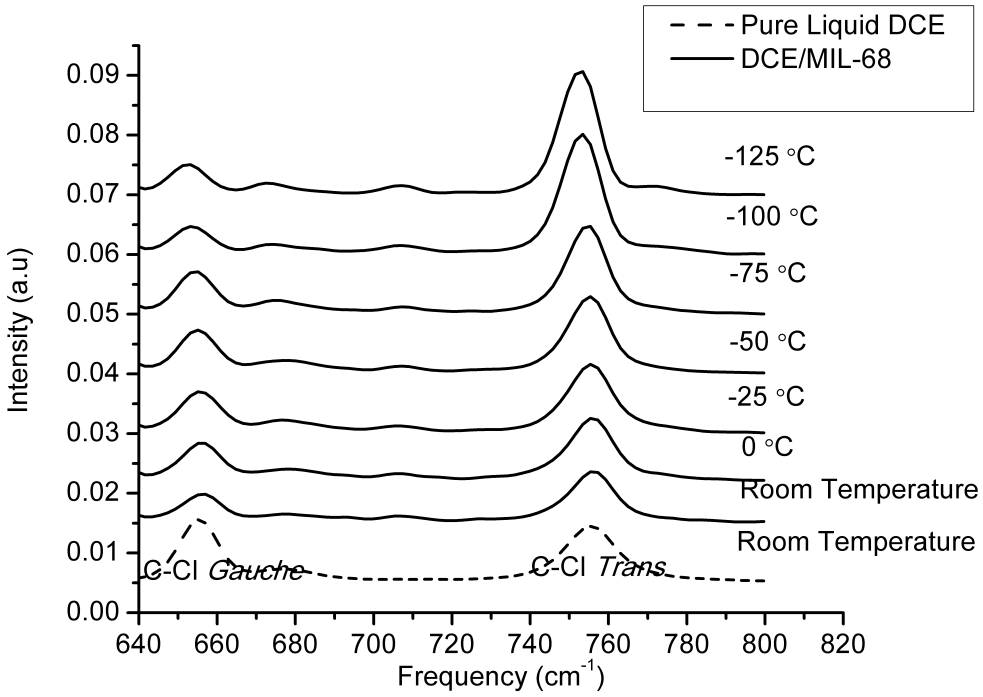

Figure 4.7 FT-Raman spectra at VT of DCE/MIL-68 system.

less thermal energy at 173 K or increased vdW interactions of DCE in the small pores. Using VTs it is possible to determine the enthalpy between the two different conformers by constructing a van't Hoff plot. A ΔH° of 3.5 kJ/mol was calculated for the DCE/MIL-68 system which will be discussed later in the chapter.

4.3.1.3 DCE/MIL-53NH_2(Al)

MIL-53NH_2 is a novel synthetic MOF derivative based on MIL-53. MIL-53NH_2, unlike MIL-53 and many other MOFs, has a polar framework. The polar framework is due to the fact that the organic linker is 2-amino-terephlaltic acid as opposed to BDC. Typical dipoles on primary amines range from 1.0 D to 1.9 D, which can stabilize the *gauche* conformer.[35] MIL-53NH_2 has a flexible framework and has a different crystallographic point group (a = 6.66 Å, b = 19.04 Å, and c = 7.80 Å) than MIL-53 (a = 6.84 Å, b = 17.04 Å, and c = 12.08 Å) when its pores are evacuated.[22] The change in crystallographic point group is due to the hydrogen bonding occurring between the amino group and the organic linkers.[22]

The FT-Raman spectra for MIL-53NH_2 have more fluorescence, which is most likely due to the additional resonance structure (Figure B.3). The framework of MIL-53NH_2 exhibits a peak near the peaks of the *gauche* conformers of DCE. A full list of DCE peaks in MIL-53NH_2 can be seen in Table 4.4.

In order to resolve the C-Cl vibrations from those of the framework, the spectra were run at a resolution of 2 cm^{-1}. The fluorescence and the 2 cm^{-1} resolution are the causes of poor S/N in the spectra.

TGA (Figure 4.8) was run to determine the maximum loading of DCE within the framework. The maximum loading was determined to be 0.64 molecules/unit-cell, which was used during the experiments in order to maximize the intensity of the C-Cl stretches. This loading is double that seen in the DCE/MIL-53 system even though the volumes of the two MOFs are almost the same. MIL-53(AM) has a pore volume of 1383.2 V/Å^3 whereas MIL-53NH$_2$(AM) has a pore volume of 1408.4 V/Å^3. Therefore, the difference in loading can be accounted for by the increase in the spatially smaller gauche population within MIL-53NH$_2$. The FT-Raman spectrum (Figure 4.9) shows that the *trans* population at 298 K is 52%. This percentage falls in the middle of the two previously seen MOFs, and is in-between that of the gas and liquid phase. As the dipole of the primary amine is not as strong as the *gauche* dipole of DCE, this value supports the hypothesis that DCE is interacting with the primary amine. The FWHH in the system is the lowest of all DCE/MOF systems at RT with a FWHH of 9.6 cm^{-1}. The DCE molecules have less molecular tumbling, as the dipole-dipole interactions would prevent the molecule from rotating freely within the pores.

VT runs were performed on the DCE/MIL-53NH$_2$ system and showed an increase to 85% in the *trans* population at 173 K. The *trans* population of this system resembles that of the DCE/MIL-53 system at low temperatures. By removing energy from the system, DCE is forced to adopt the thermodynamically favored *trans* conformation as seen by the enthalpy of the system. The dipole interaction from the primary amine is not as strong as cations in zeolites to cause the *gauche*

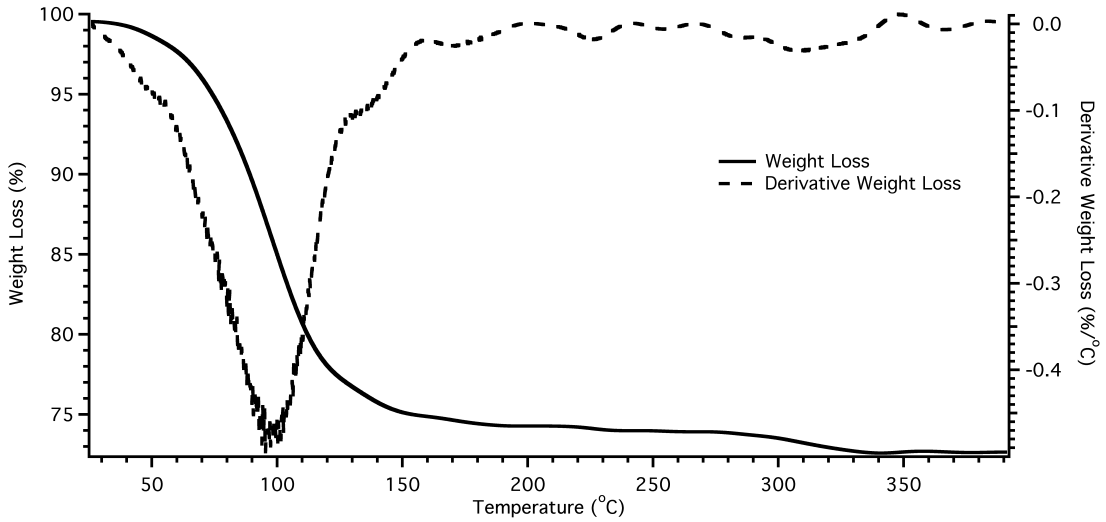

Figure 4.8 TGA curve and DTG curve of DCE/MIL-53NH$_2$ system.

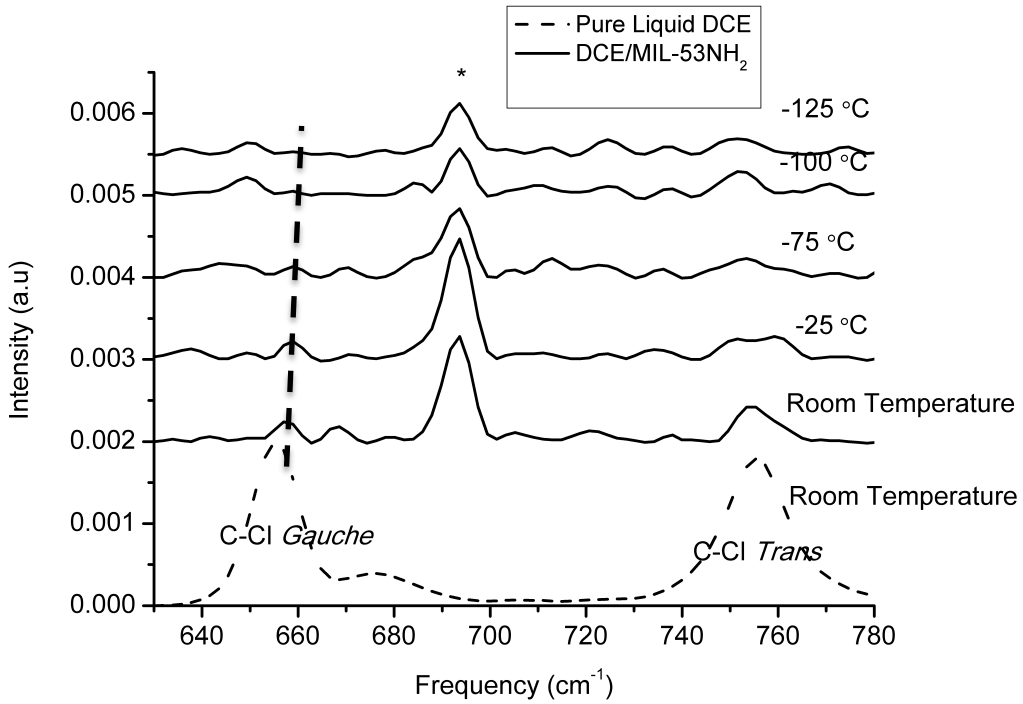

Figure 4.9 FT-Raman spectra at VT of DCE/MIL-53NH$_2$ system (*indicates framework).

conformation to be thermodynamically favored.[7] While a slight red-shift is seen at VT, using a resolution of 2 cm^{-1} there is no significant shift of the *gauche* peak in this case. The FWHH at low temperatures increase unlike DCE/MIL-53 and DCE/MIL-68. The dipole interaction is less significant at low temperatures, which allows for an increase in molecular motion. Using the VT spectra it is possible to obtain the enthalpy of rotation of the molecule within the system by creating a van't Hoff plot which gives a ΔH° of 2.1 kJ/mol.

Table 4.4 Peak assignments of FT-Raman spectra of DCE/MIL-53NH_2.

DCE/MIL-53NH_2 (cm^{-1})	Assignment:[6]	Literature Value: DCE (Pure liquid)[6]
658	C-Cl (*gauche*)	654
754	C-Cl (*trans*)	755

4.3.1.4 *Trans* → *Gauche* Enthalpy Change of 1,2-Dichloroethane

The equilibrium of DCE between the *gauche* and *trans* conformers is proportional to

$$\ln K = -\Delta H^o/RT + \Delta S^o/R \qquad (4.2)$$

where K is the equilibrium constant, H is the enthalpy, and S is the entropy of the system. Differentiation of equation (4.2) with respect to 1/T gives the van't Hoff equation. By plotting the equilibrium constant K (I_g/I_t) vs 1/T results in a linear graph, where the slope is equal to the enthalpy of the system (Figure 4.10). Using this process the enthalpy change of DCE in the gas phase has been calculated to be 4.9 kJ/mol to go from the *trans* conformer to the *gauche* conformer (*t*→*g*).[8] Previous studies have investigated the *t*→*g* enthalpy change of DCE within different zeolites and SAPOs and have found that the *t*→*g* enthalpy change of the system relies on the

microporous material.[7] Currently no studies exist that investigate the enthalpy of DCE/MOF systems. The *t*→*g* enthalpy change of all previously mentioned systems are lower then the *t*→*g* enthalpy change of DCE in the gas phase. This is due to the dipole-dipole interactions of the *gauche* DCE molecules favouring the *gauche* conformer more than the *gauche* conformers in the gas phase. All the systems favour the *trans* conformer at low temperatures. As thermal energy is removed from the systems, DCE adopts the thermally prefered conformer. All three systems give a positive *t*→*g* enthalpy change of 2.52 kJ/mol, 1.95 kJ/mol, and 1.70 kJ/mol, for MIL-53, MIL-68, and MIL-53NH_2 respectively. Both MIL-68 and MIL-53NH_2 have similar enthalpies as the *gauche* conformation of DCE is stabilized by dipole-dipole interactions. In the case of MIL-53 there are no dipole interactions, which is why it takes more energy to go from the *trans* conformer to the *gauche* conformer.

4.3.2 1-Bromo-2-Chloroethane

BCE is a dihaloalkane whose conformations have been extensively studied in the gas, liquid, and solid phases.[3,10] Using FT-Raman spectroscopy and TGA the conformations of BCE in different MOFs will be investigated.

4.3.2.1 1-Bromo-2-Chloroethane/MIL-53(Al)

BCE was loaded into MIL-53 using the same experimental method as DCE. Using TGA a maximum loading of 0.12 molecules/unit cell was determined (Figure 4.11). BCE replaces a chlorine atom of DCE with a bromine atom. As a bromine atom is larger than a chlorine atom, this may be the reason why the maximum loading is slightly less for BCE/MIL-53 than DCE/MIL-53. FT-Raman spectroscopy was used to

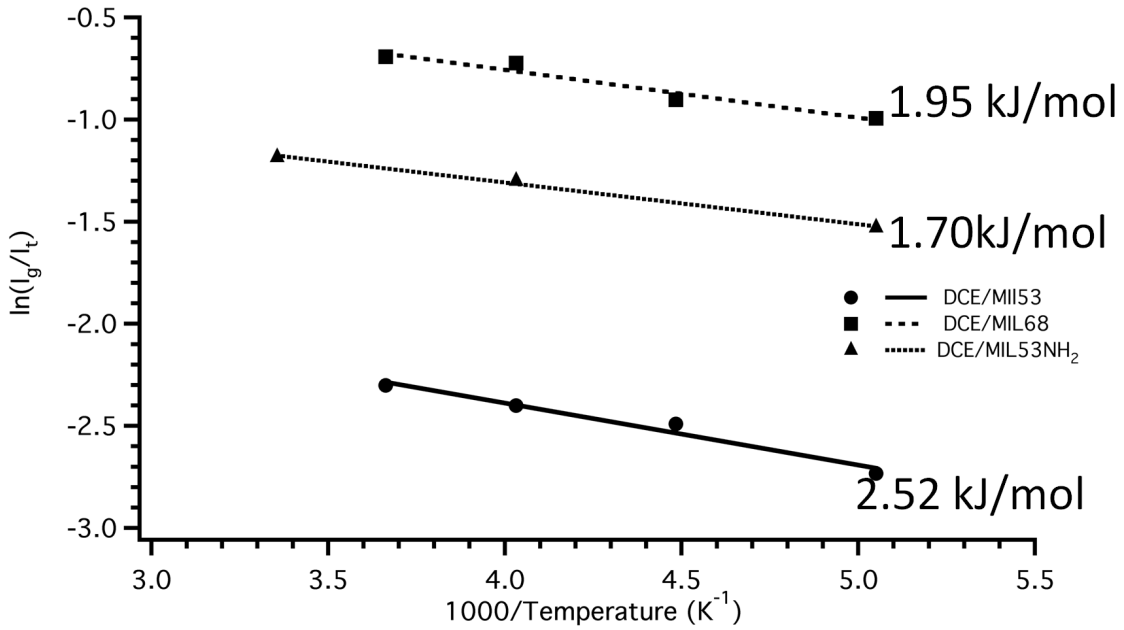

Figure 4.10 van't Hoff plot of DCE/MIL-53, DCE/MIL-68, and DCE/MIL-53NH_2 systems.

investigate the conformation of BCE within MIL-53 using the maximum determined loading. Due to the strong Raman peaks that arise from the MOF, the carbon halogen stretches are of the greatest interest in this study. Both the C-Cl and the C-Br stretch exist in the 600 cm^{-1}-800 cm^{-1} region (Figure B.4), which has very few peaks that belong to the MOF (Figure 4.12). The full set of FT-Raman peaks from the BCE/MIL-53 system can be found in Table B.3. A full list of the BCE peaks in MIL-53 and MIL-68 are given in Table 4.5. The C-Br *gauche* stretch is near 628 cm^{-1}, which as seen in Table 4.5, overlaps with the peak at 630 cm^{-1} from the framework. Due to this overlap, only the C-Cl *trans* and *gauche* stretches are investigated for the purpose of

Table 4.5 Peak assignments of BCE/MIL-53 and BCE/MIL-68.

BCE/MIL-53 (cm^{-1})	BCE/MIL-6 (cm^{-1})	Assignment Framework BCE[6]	Literature BCE (pure liquid) (cm^{-1})[6]
569	571	C-Br (g*auche*)	569
631	632	C-Br(*trans*)+ (CCCC)	632
666	665	C-Cl(*gauche*)	666
726	729	C-Cl (*trans*)	726

this study, as they will give more accurate results then deconvoluting the spectra. The *gauche* conformer of BCE is the point group C_1 and the *trans* conformer of BCE is the point group C_s. Even though both conformers are different point groups, group theory predicts that there will only be one C-Cl *gauche* peak and one C-Cl *trans* peak.[6] In BCE/MIL-53 the peak at 726 cm^{-1} corresponds to the C-Cl *trans* stretch and the peak

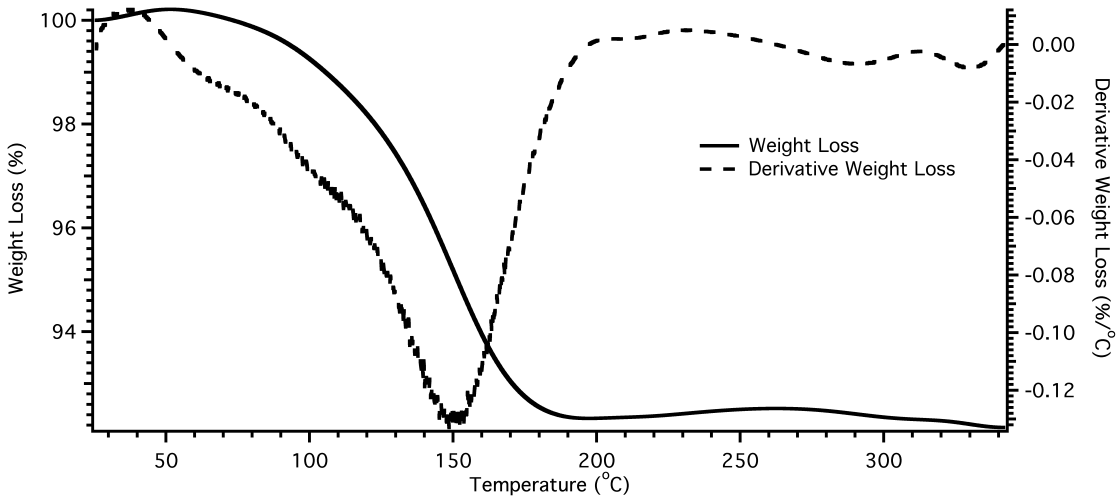

Figure 4.11 TGA curve and DTG curve of BCE/MIL-53 system.

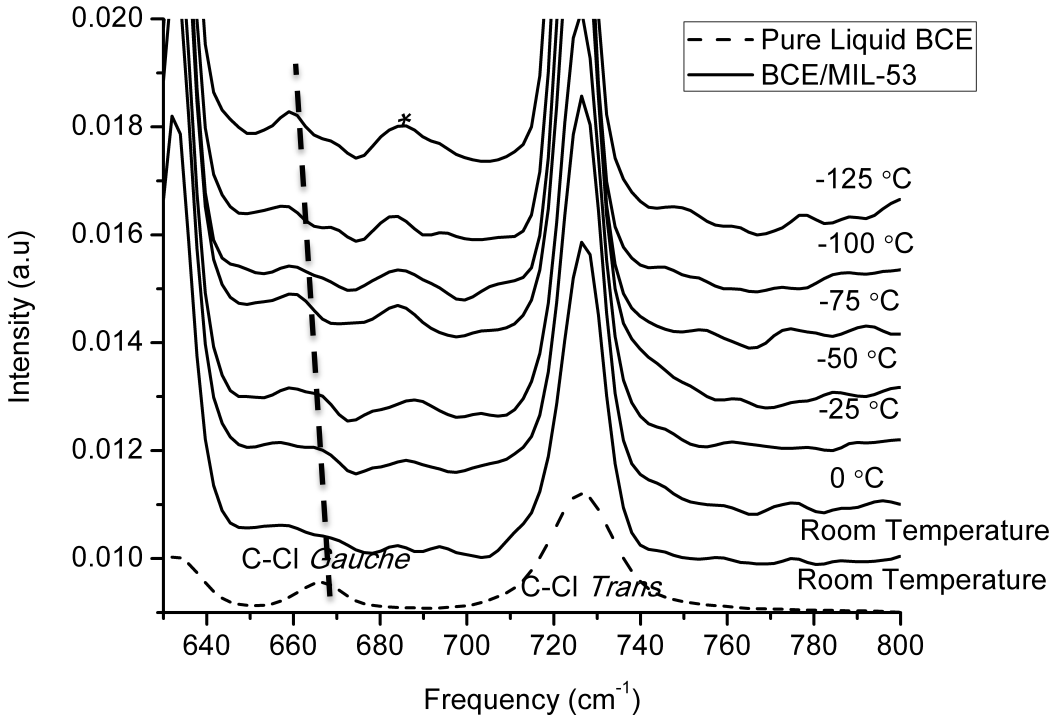

Figure 4.12 FT-Raman spectra at VT of BCE/MIL-53 system (*C-Br *trans* and framework overlap).

at 666 cm^{-1} corresponds to the C-Cl *gauche* stretch. Using Equation 4.1 for the intensity of a Raman band for a conformational isomer it is possible to determine the *trans* population of the system. A previously calculated Raman scattering ratio was determined to be 6.0.[10] By using this ratio the *trans* population of BCE in MIL-53 was calculated to be 69%. The *trans* population value of BCE/MIL-53 is near neither the gas phase value nor the liquid phase value. Once again, the low dielectric constant of BDC and the lack of reorientation of the aromatic rings of BDC prevent the ligand from stabilizing the *gauche* conformation. The calculated *trans* population in the BCE/MIL-53 system is only slightly lower than that of the DCE/MIL-53 system. The *gauche* conformation of BCE has a weaker dipole than that of the *gauche* conformation of DCE. It is likely that the weaker dipole of the *gauche* BCE molecules have less of a stabilizing effect on other *gauche* conformers.

The peak position for BCE in MIL-53 does not change at RT as the *trans* peak's wave number is located at 726 cm^{-1} and the *gauche* peak's wave number is 666 cm^{-1}. The lack of shift indicates no external attractive or repulsive forces are taking place for the C-Cl vibration once again indicating the C-H vibration is interacting with the π system may be the predominant interaction. At RT, the FWHH drops considerably, from 17.3 cm^{-1} to 10.2 cm^{-1} (65%), which is nearly the same percentage as the decrease in FWHH of the DCE/MIL-53 system (69%). The extra decrease in motion may be attributed to the fact that the BCE/MIL-53 system has a larger molecular size.

Upon cooling, the conformation of BCE is further shifted to the *trans* conformer. At 173 K the *trans* population is 85% which correlates with the *trans* population in the gas phase as determined in earlier studies.[36] As the system undergoes cooling, the C-Cl *trans* peak exhibits a gradual red-shift (4 cm^{-1}) and a decrease in the FWHH (3 cm^{-1}). Again, it is likely that the 4 cm^{-1} red-shift and the decrease of the FWHH by 3 cm^{-1} is due to removing thermal energy from the system. The VT runs determined a ΔH° of 4.21 kJ/mol.

The PXRD pattern of BCE/MIL-53 shows that the shape of the MIL-53 pores adopts a shape near the AM version. However, the peaks of the PXRD patterns of MIL-53 and BCE/MIL-53 are not identical, indicating that MIL-53 does have a unique phase for BCE. Therefore, it is possible that MIL-53 slightly distorts from the AM phase in order to maximize interactions with guest-molecules.

4.3.2.2 1-Bromo-2-chloroethane/MIL-68(In)

BCE was loaded into MIL-68 and TGA was run to determine the maximum loading. Again the TGA could not distinguish between guest molecules in the small pores and the large pores. TGA was used solely to determine the maximum loading of BCE in the MOF, which was confirmed by the DTG curve having a single peak (Figure 4.13). The maximum loading for BCE in MIL-68 was calculated to be 1.57 molecules/unit-cell. As seen in MIL-53, the loading of BCE in MIL-68 is slightly less than DCE/MIL-68. Again this can most likely be attributed to the larger molecular size of BCE.

The FT-Raman spectrum of MIL-68 is still dominated by the reflections of the

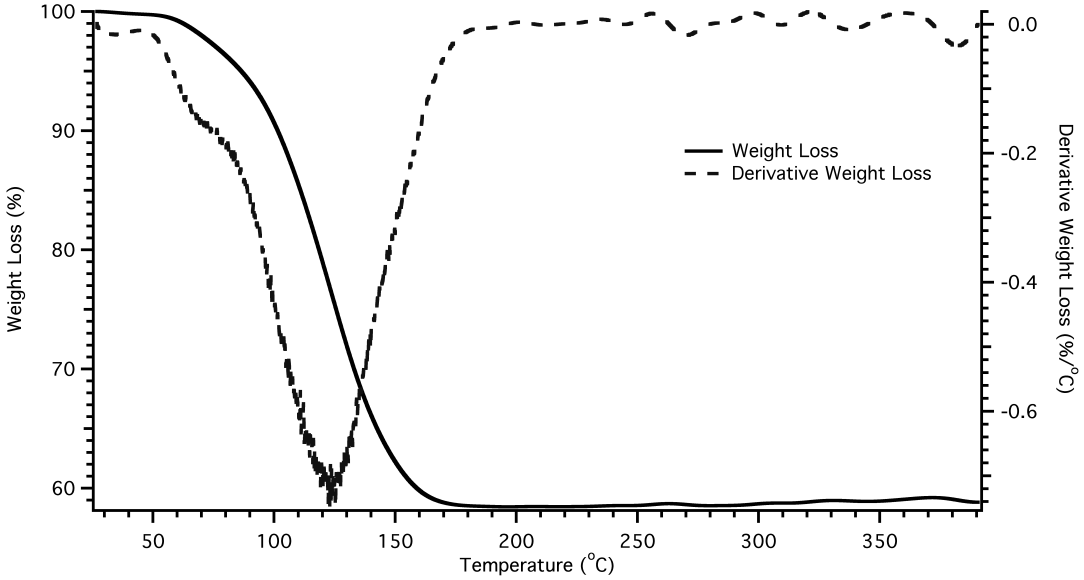

Figure 4.13 TGA curve and DTG curve of BCE/MIL-68 system.

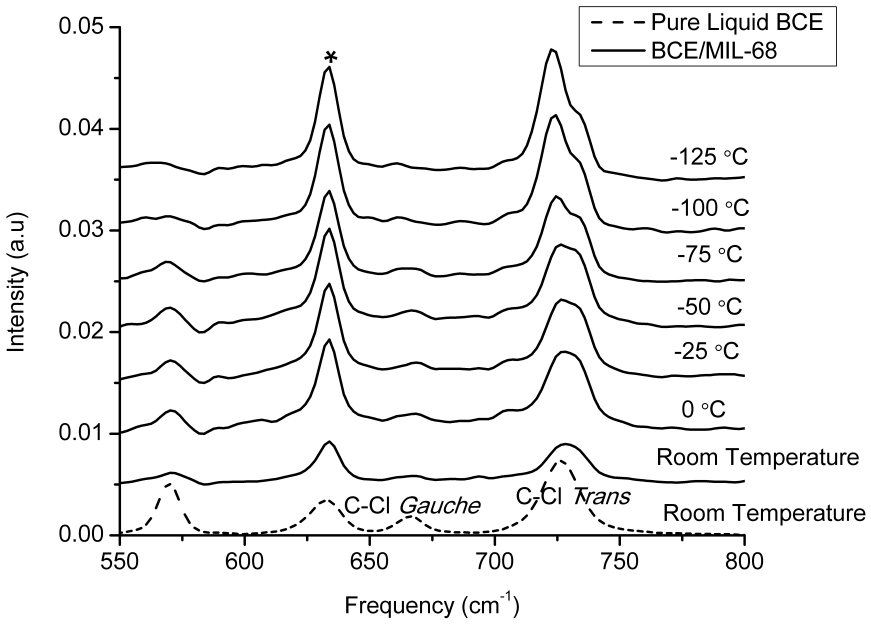

Figure 4.14 FT-Raman spectra at VT of BCE/MIL-68 system (*C-Br *trans* peak and framework overlap).

BDC linkers (Figure 4.14). However, there remains a lack of peaks in the 600 cm^{-1} - 800 cm^{-1} range (Figure B.5). The full set of BCE peaks in MIL-68 can be seen in Table 4.5. MIL-68 also has a peak at 630 cm^{-1}, as seen in MIL-53. This peak prevents the study of the C-Br vibrations, due to the overlap of the C-Br *gauche* peak with the framework peak. Using a Raman scattering of 6.0 the *trans* population of BCE in MIL-68 was calculated to be 67%. DCE favors the *gauche* conformer in the two pore system of MIL-68. However, BCE has a *trans* population that resembles that found in the BCE/MIL-53 system. The strength of the *gauche* DCE dipole allows dipole-dipole interactions up 12 Å to 15 Å. However, BCE has a weaker dipole, and therefore that distance may be shorter. Therefore, BCE within the small pores may not interact with one another, and consequently the *trans* population of the BCE/MIL-68 system would be similar to that of the BCE/MIL-53 system. Due to the shoulder of the C-Cl *trans* peak at low temperatures, the FWHH and peak position at room temperature may be inaccurate and therefore insignificant.

The C-Cl *gauche* peak intensity decreases significantly at low temperatures, while the *trans* peak increases in intensity. The population of the *trans* conformer was calculated to be 85% at 173 K. Both the C-Cl *gauche* peak and the C-Cl *trans* peak exhibit a small red-shift at low temperatures. Upon inspection, the C-Cl *trans* peak starts to exhibit a shoulder at 223 K. This shoulder becomes more pronounced as the temperature of the system decreases. The shoulder may be indicative that BCE is located in both the small pores and large pores, indicating FT-Raman spectroscopy may be more sensitive than TGA. The possible reason that this effect is seen with BCE and not DCE may be due to the size of the molecule. It is possible that

BCE is able to have stronger interactions with the π system in the small pores due to the proximity of the halocarbon to the organic linker.

The C-Cl *gauche* peak has a very low intensity causing the FWHH to be unreliable. The *trans* peak also cannot be used to investigate the FWHH due to the emergence of the shoulder at low temperatures. Using the VT experiment a van't Hoff plot was created to determine the internal rotation enthalpy of BCE. The ΔH° was determined to be 3.52 kJ/mol for the BCE/MIL-68 system, which is discussed later in the chapter.

4.3.2.3 1-Bromo-2-chloroethane/MIL-53NH_2(Al)

BCE was loading into MIL-53NH_2, which has a higher fluorescence than both MIL-53 and MIL-68. The spectrum of MIL-53NH_2 only has a few peaks within the 600 cm^{-1} - 800 cm^{-1} region (Appendix B.6), however, one of these peaks has a slight overlap with the C-Cl *gauche* peak at 680 cm^{-1}. A full list of the BCE peaks can be found in Table 4.6. The supporting information has a full list of the peaks in the BCE/MIL-53NH_2 spectra (Table B.4). To overcome the overlap problem of the framework and C-Cl *gauche* peak, the experiments were run at a resolution of 2 cm^{-1}. Using TGA, the maximum loading was determined to be 0.50 molecules/unit-cell (Figure 4.15). This loading is roughly four times as large as the loading of BCE in MIL-53, and can be attributed to the conformation population of BCE in MIL-53. The FT-Raman spectrum of BCE/MIL-53NH_2 shows a significant decrease in the intensity of the *trans* peak (Figure 4.16). Using the previously calculated Raman scattering ratio the *trans* population of BCE in MIL-53NH_2 is 32%. In this case a

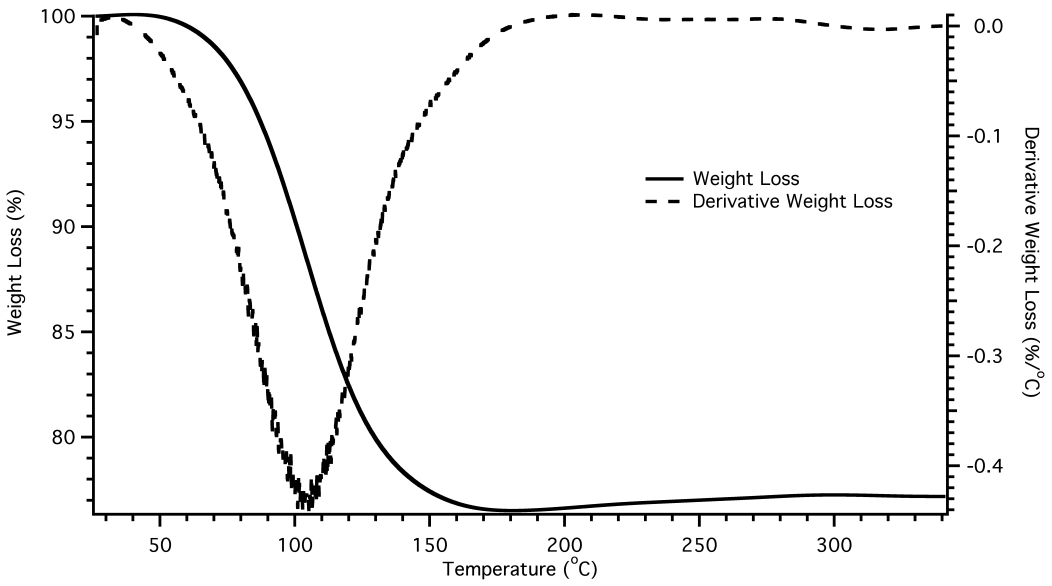

Figure 4.15 TGA curve and DTG curve of BCE/MIL-53NH_2 system.

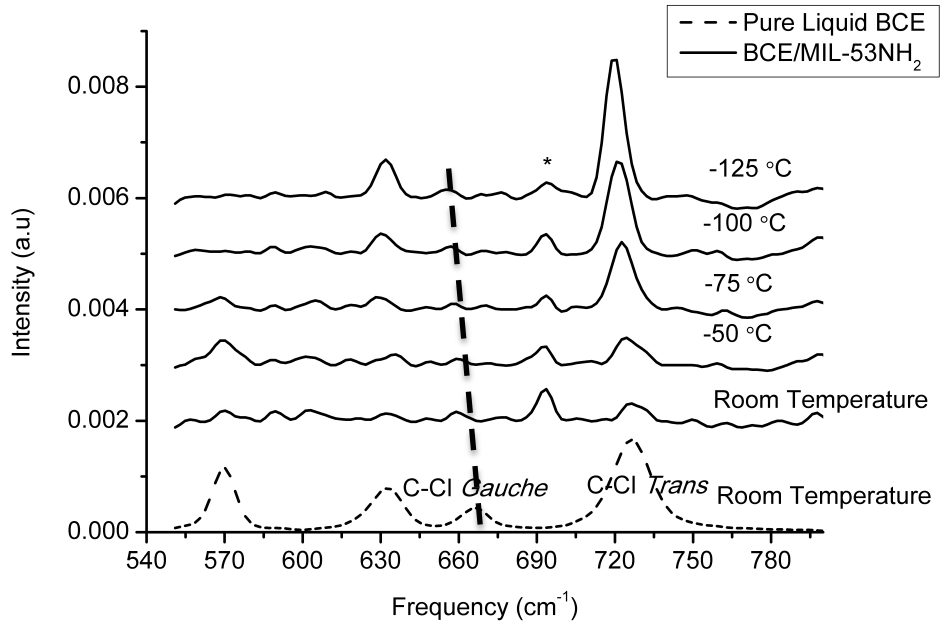

Figure 4.16 FT-Raman spectra at VT of BCE/MIL-53NH_2 (*framework)

majority of BCE molecules adopt the spatially smaller conformation allowing for more molecules of BCE to be loaded within the pores. BCE adopting the smaller conformation is further confirmed by the wave number shift. The *gauche* peak shifting by 6 cm^{-1} may be indicative that hydrogen bonding is taking place between the primary amine and BCE. The FWHH at RT decreased significantly when compared to the liquid phase from 15 cm^{-1} to 11 cm^{-1} indicating the dipole may be preventing molecular tumbling.

Upon cooling a large shift in the *trans* population occurs. At 173 K the *trans* population is 83%, which emulates the DCE/MIL-53NH_2 system. At low temperatures the conformation of BCE adopts the more thermodynamically preferred *trans* conformer. Using the VT spectra it is possible to determine the internal rotation enthalpy of the molecule. For the BCE/MIL-53NH_2 system the $\Delta H°$ is 1.7 kJ/mol.

Table 4.6 Assignments of Raman spectra of BCE/MIL-53NH_2.

Peak Values (cm^{-1})	Assignment: BCE[6]	Literature Value: BCE (pure liquid)[6] (cm^{-1})
659	C-Br (*gauche*)	659
632	C-Br (*trans*)+ (CCCC)	632
660	C-Cl (*gauche*)	666
725	C-Cl (*trans*)	726

4.3.2.4 *Trans* → *Gauche* Enthalpy Change of 1-Bromo-2-chloroethane

The *t*→*g* enthalpy of the BCE/MOF systems was determined by plotting the equilibrium constant K (I_g/I_t) vs 1/T to give van't Hoff plots (Figure 4.17). This method has been previously used to determine the internal enthalpy change of BCE in the gas phase. The enthalpy was determined to be 5.56 kJ/mol to go from the *trans* conformation to *gauche* conformation. The *t*→*g* enthalpy change of BCE has been previously determined in zeolites such as Si-Y and Silicate-1, whereas the *t*→*g* enthalpy change of BCE in MOFs has not yet been determined.[10] The values for this study are 4.21 kJ/mol for MIL-53, 3.52 kJ/mol for MIL-68 and 2.11 kJ/mol for MIL-53NH_2. In the case of the three systems studied each ΔH gave a positive value, as the *trans* conformer is highly favored at low temperatures. This differs from the previous zeolite studies where systems with many cations and small cages show a preference for the *gauche* conformer due to dipole-cation effects and spatial restrictions due to the small cages.[10] In the case of BCE, BCE/MIL-53NH_2 has a lower $\Delta H_{t\rightarrow g}$ than BCE/MIL-68. The dipole of the BCE in the BCE/MIL-68 system is not strong enough to stabilize the nearest BCE molecule. In the BCE/MIL-53NH_2 system the *gauche* conformer is stabilized through the dipole of the primary amine. MIL-53 once again has the highest *t*→*g* enthalpy change, as there are no dipole-dipole effects to stabilize the *gauche* conformation.

4.3.3 Chlorocyclohexane

The conformational analysis of CCH has been extensively studied through vibrational spectroscopy and NMR.[7,16] These studies have shown that CCH can adopt

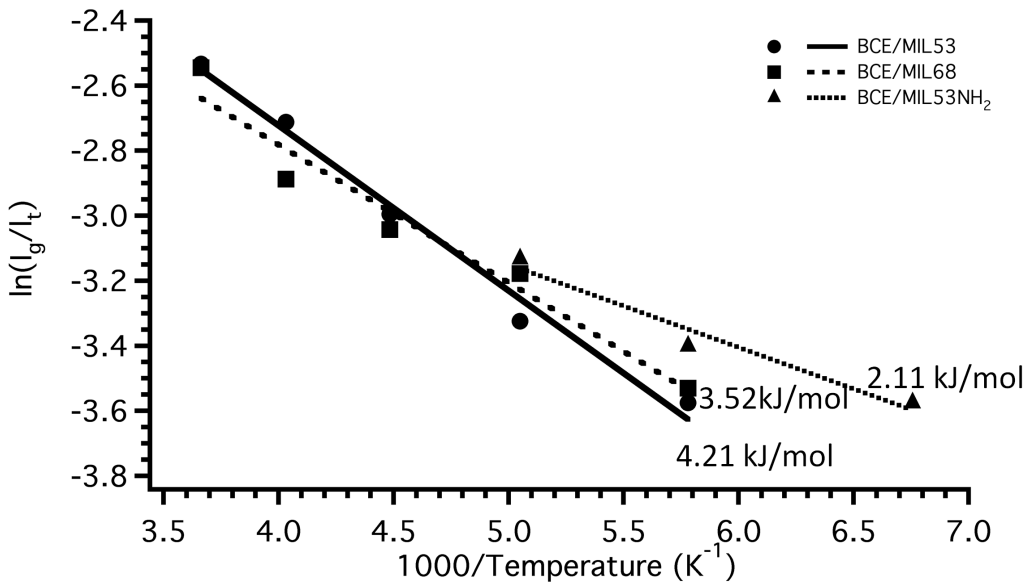

Figure 4.17 van't Hoff plots of BCE/MIL-53, BCE/MIL-68, and BCE/MIL-53NH_2 systems.

either the *axial* conformation or the *equatorial* conformation, with a prefence for the latter due to vdW interactions. Current studies of CCH and microporous materials have only investigated CCH/Zeolite systems.[7] Using FT-Raman spectroscopy and TGA, the conformations of CCH in different MOFs were studied.

4.3.3.1 Chlorocyclohexane/MIL-53(Al)

CCH was loaded in MIL-53 and TGA experiments showed that a maximum loading of 0.12 molecules/unit-cell was possible (Figure 4.18). The broad DTG peak may be due to either the *axial* or *equatorial* conformer interacting more favourably with the framework. In order to utilize the Formula 4.1 to determine the ratio of the *equatoria l* to *axial* conformations, a previously calculated Raman scattering cross section of 0.85 was employed in this study.[7] This value was determined through a vibrational study of CCH in a CS_2 solution and a previous NMR study that determined the ΔG for *axial* to *equatorial* interchange was 0.64 kcal/mol.[16] This Raman scattering cross section assumes the scattering cross section is independant of temperature and environnment. The FT-Raman spectra of CCH loaded in MIL-53 (Figure 4.19) shows a distinct change in intensity compared to that of the pure CCH solution. The intensity of the C-Cl vibrations decrease as the dominant force in the spectra is the MOF framework (Figure B.7). The *axial* vibration of C-Cl in the MOF is found at 685 cm^{-1} and the *equatori*al vibration of C-Cl is found at 730 cm^{-1}.

Using the integrated intensity of each peak, it was determined that an *equatorial* population of 84% exists at 298 K in this system. This value slightly

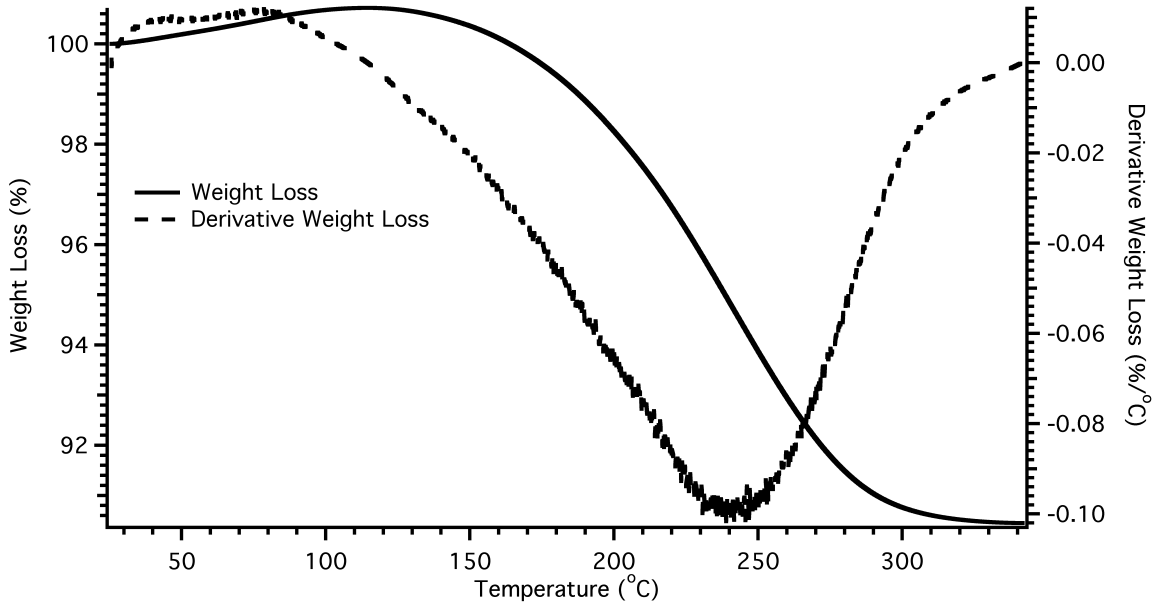

Figure 4.18 TGA curve and DTG curve of CCH/MIL-53 system.

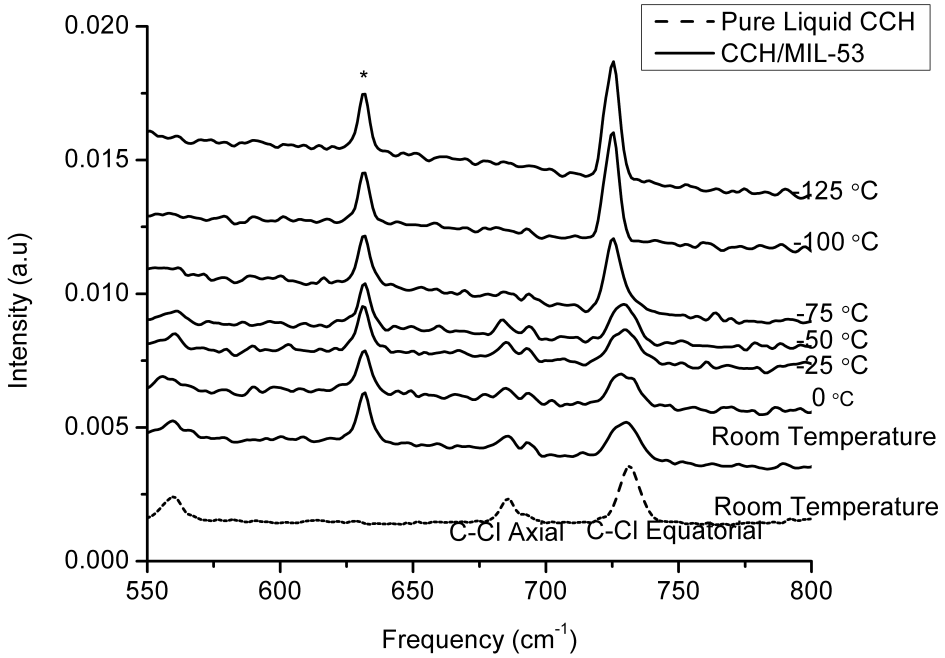

Figure 4.19 FT-Raman spectra at VT of CCH/MIL-53 system (*indicates framework).

increases when compared to the *equatorial* population of liquid CCH, which is 73%. Haloalkane compounds have distinct dipole moments for different conformations that can determine the preferred conformation in solution. Halocyclic compounds will have a dipole for both the *equatorial* and *axial* conformation. For this reason, the conformation of CCH in MIL-53 slightly favors the *equatorial* conformation as it is the most stable conformer that CCH can adopt.

At low temperatures the CCH/MIL-53 FT-Raman spectrum changes drastically. The most notable change is the disapperance of the *axial* C-Cl peak at 685 cm^{-1}. At low temperatures a distinct preference for the *equatorial* conformer exists, as its population is 97%. Unlike previous systems where the change is gradual, this transformation happens rapidly between 223 K and 198 K. At 173 K the *axial* peak disappears and coincides with an increase in the *equatorial* peak intensity. The reason for this may be due to the equatorial conformer being thermally prefered in order to minimize vdW interactions of CCH. At this temperature there is also a drastic decrease of the FWHH at the *equatorial* peak which decreases to 6.5 cm^{-1} from 12 cm^{-1} at RT. As discussed earlier, MIL-53 can undergo a phase change at low temperatures. Most likely MIL-53 is undergoing a phase change which creates a smaller volume and consequently restricts the motion of CCH. It was not possible to run PXRD at low temperatures, therefore the phase change can not be confirmed.

Using the equilibrium constant K (I_{eq}/I_{ax}) from the VTs FT-Raman spectra, a van't Hoff plot (Figure 4.20) was created to determine a $\Delta H_{ax \rightarrow eq}$ of 7.6 kJ/mol for the CCH/MIL-53 system. 7.6 kJ/mol is significantly higher than that of pure liquid of

CCH which has an enthalpy of 1.1 kJ/mol.[37] This large *ax*→*eq* enthalpy change further supports the hypothesis that MIL-53 may be stabilizing the *equatorial* conformation. The large energy difference that CCH must overcome to go from *equatorial* to *axial* indicates that CCH may be able to interact with multiple π systems in order to stabilize the *equatorial* conformation.

FT-Raman spectroscopy of CCH in MIL-68 and MIL-53NH_2 was unable to be carried out. When CCH was loaded into either MIL-68 or MIL-53NH_2, the MOF would decompose. The decomposition of MIL-68 and MIL-53NH_2 was confirmed by PXRD.

4.3.4 Powder X-ray Diffraction of Halocarbons/Metal Organic Framework Systems.

PXRD was conducted on all halocarbon/MOF systems to understand the phase changes that were taking place to maximize guest-host interactions.

4.3.4.1 Powder X-Ray Diffraction of MIL-53(Al) Systems

The flexibility of MIL-53 gives distinct PXRD patterns depending on the guest molecule. The different PXRD patterns arise from a change in crystallographic space groups and lattice parameters.[38] A distinct difference exists between the LT and AM PXRD patterns. In the MIL-53(AM) PXRD pattern a cluster of peaks exists between 10 2Θ and 20 2Θ. In this cluster of reflections, the peaks located at 17 2Θ and 18 2Θ disappear for MIL-53(LT). The PXRD patterns of the three different systems, MIL-53(AM) and MIL-53(LT) (Figure 4.21) differ from one another but do share some common characteristics.

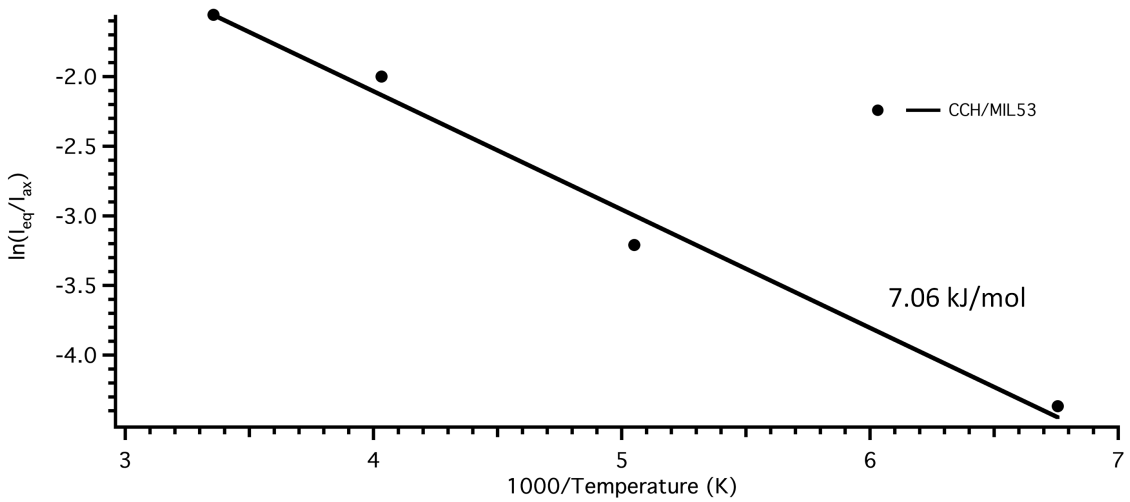

Figure 4.20 van't Hoff plot of the CCH/MIL-53 system.

MIL-53(LT) lacks peaks between 15 2Θ and 19 2Θ, and has reflections which have been shifted from 13 2Θ to 16 2Θ. However, the 3 systems retain the two reflections at 17 2Θ and 18 2Θ that exist for the MIL-53(AM) phase which do not exist for the MIL-53(LT) phase. It is most likely that the halocarbon/MIL-53 systems retain some characteristics of both the LT (narrow pores) and AM (large pores) versions of MIL-53. Most likely, MIL-53 changes phases for each guest-molecule to maximize the C-H interaction with the π system. This interaction helps stabalize the *trans* conformation for DCE, BCE and the equatorial conformation for CCH. The reflections from 10 2Θ to 14 2Θ change for each system indicating that the lattice parameters of MIL-53 does indeed change for each of DCE/MIL-53, BCE/MIL-53, and CCH/MIL-53.

4.3.4.2 Powder X-Ray Diffraction of MIL-68(In) systems

MIL-68 does not contain a flexible framework, and as such, the PXRD of the AM MOF and the evacuated MOF are identical in peak position. However, while the PXRD of both DCE/MIL-68 and BCE/MIL-68 are similar, they significantly differ from AM MIL-68 (Figure 4.22). The loaded systems have only two strong peaks at 9 2Θ and 11.5 2Θ while the rest of the smaller reflections are obscured by noise. The loss of crystallinity may be due to a slight distortion of the MIL-68 framework once the DCE/BCE molecules are loaded. The distortion may be caused by the framework reorientating itself to accomodate the guest molecules. Due to the lack of flexibility of MIL-68 any distortion may lead to a loss of crystallinity unlike MIL-53 and MIL-53NH_2, which are flexible.

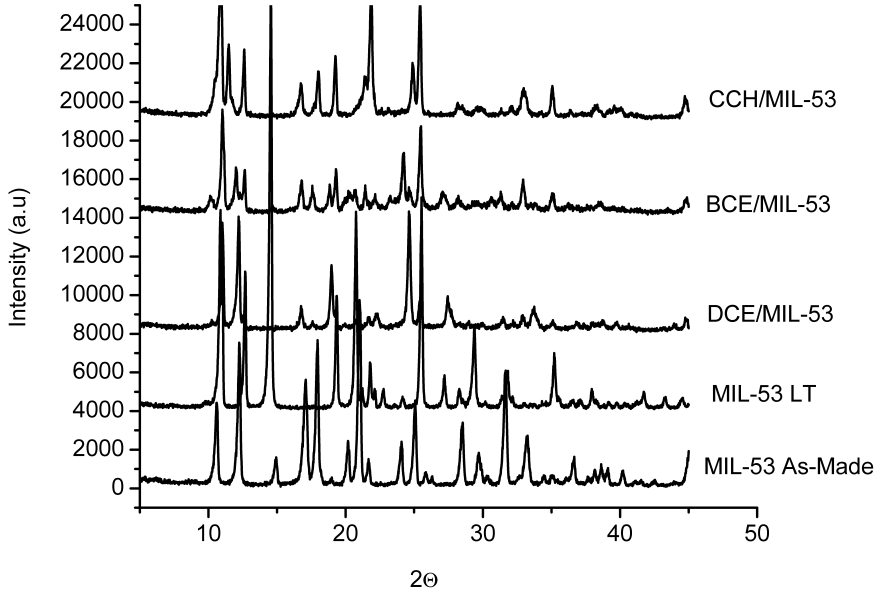

Figure 4.21 PXRD patterns of MIL-53(AM), MIL-53(LT), DCE/MIL-53, BCE/MIL-53, CCH/MIL-53.

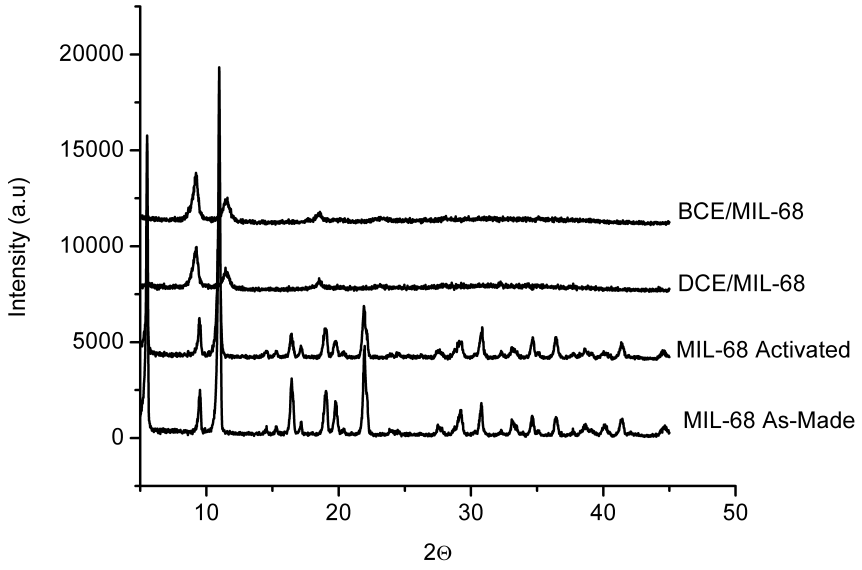

Figure 4.22 PXRD patterns of MIL-68 As-made, MIL-68 Activated, DCE/MIL-68, BCE/MIL-68.

4.3.4.3 Powder X-Ray Diffraction of MIL53-NH_2(Al) systems

MIL-53NH_2 resembles MIL-53 in the fact that it has a flexible framework with the same coordination. Once again the PXRD patterns of the AM and the LT have significant differences at both high and low reflections. Unlike MIL-53, whose framework shape is between the AM and LT framework, the systems of DCE/MIL-53NH_2 and the BCE/ MIL-53NH_2 yield PXRD patterns that strongly resemble that of the AM phase (Figure 4.23). Due to the extra noise in PXRD that seems to exist with the loaded systems, the lack of a few weak reflections may be due to low S/N. The similarity between the AM phase and the loaded PXRD patterns indicate that the MOF may not distort in order to accomodate the large guest molecules. MIL-53NH_2 seems to adopt the AM phase in order to maximize interactions with the guest-molecule.

4.5 Summary

The many different properties of a MOF dictate how it will interact with guest molecules. Whether it is the type of organic linker, the polarity of the framework, or the amount and size of the different pores all will have an influence on sorbate sorbent interactions. In the case studied, it is possible to increase the loading of MIL-53 by creating a polar framework that will prefer the spatially smaller conformation of a halocarbon.

Due to the the ligands being locked in place, it is not possible to examine a MOF as a typical solvent or dielectric medium in order to study the conformation of the guest molecules. The lack of rearrangement of the π systems prevents the

aromatic effect from stabilizing the *gauche* conformation. This causes the C-H of the halocarbons to be able to only maximize interactions with a π system. In order to maximize the storage possibilites of halocarbons in MOFs, it is necessary to maximize the loading of each unit-cell. To do this, large MOFs with a polar framework may be the ideal candidate for possible storage in the future of toxic and harmful halocarbons. Future studies should also involve high pressure studies of the halocarbon/MOF systems in order to ensure maximum adsorbtion.

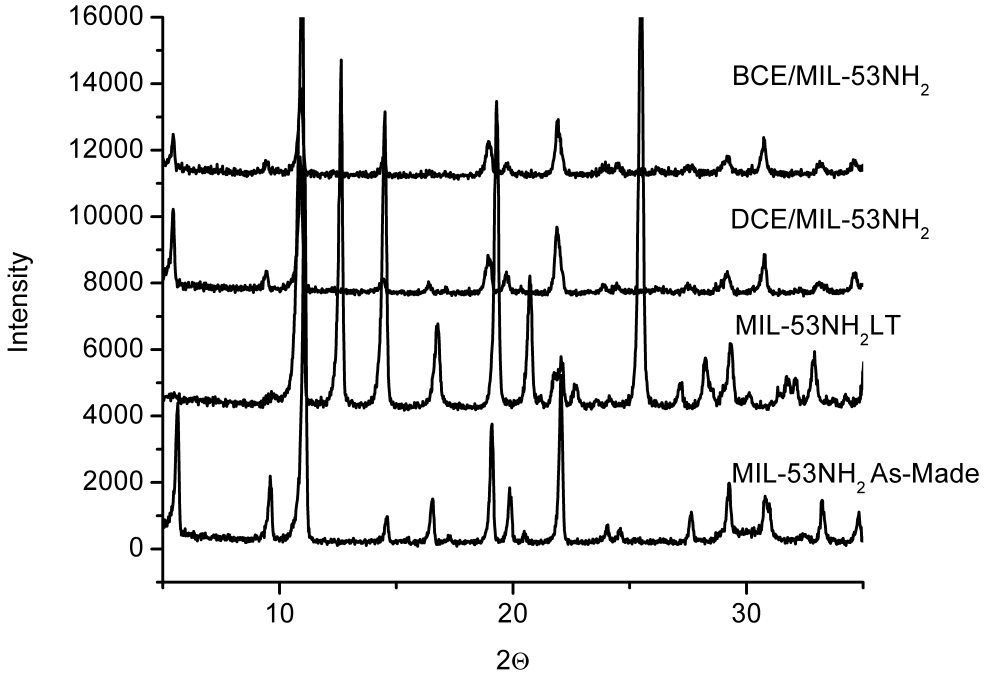

Figure 4.23 PXRD patterns of MIL-53NH$_2$(AM), MIL-53NH$_2$(LT), DCE/MIL-53NH$_2$, BCE/MIL-53NH$_2$.

4.6 References for Chapter 4

1. Mizushima, S.I. *Sci Pap Inst Phys Chem Res* **1934**, *25,* 159.

2. Sreeruttun, R. K.; Ramasami, P. *Phys. Chem. Liq.* **2006**, *44*, 315.

3. Koda, S.; Matsui, H.; Nomura, H. *J. Chem. Soc. Faraday Trans I.* **1989**, *85*, 957.

4. Gan, T. H.; Peel, J. B.; Willett, G. D. *J. Chem. Soc. Faraday Trans II.* **1977**, *73*, 965.

5. Franco, M. L.; Ferreira, D. E. C.; Santos, H. F. D.; De Almeida, W. B. *J. Chem. Theory Comput.* **2008**, *4*, 728.

6. Tanabe, K. *Spectrochim Acta* **1972**, *28A*. 407

7. Leech, J. H., Conformational Behaviour of Guest Molecules in Zeolite Hosts. Msc. Dissertation, The University of Western Ontario, 2003.

8. Wiberg, K. B.; Keith, T. A.; Frisch, M. J.; Murcko, M. *J. Phys. Chem.* **1995**, *99*, 9072.

9. Vilaseca, E. *J. Chem. Phys* **1996**, *104*, 4243.

10. Wang, H.; Huang, Y. *Langmuir* **2009**, *25*, 8042.

11. Garrot, B.; Couderc, G.; Simonot-Grange, M.H.; Stoeckli, F. *Microporous Mesoporous Mater.* **2002**, *52*, 199.

12. Martucci, A.; Pasti, L.; Nassi, M.; Alberti, A.; Arletti, R.; Bagatin, R.; Vignola, R.; Sticca, R. *Microporous Mesoporous Mater.* **2012**, *151*, 358.

13. Huang, Q.; Xue, X.; Zhou, R. *J. Hazard. Mater.* **2010**, *183*, 694.

14. Baran, R.; Kamińska, I. I.; Śrębowata, A.; Dzwigaj, S. *Microporous Mesoporous Mater.* **2013**, *169*, 120.

15. Xian, S.; Li, X.; Xu, F.; Xia, Q.; Li, Z. *Sep. Sci. Technol.* **2013**, *48*, 1479.

16. Aliev, A. E.; Harris, K. D. M.; Mordi, R. C. *J. Chem. Soc., Faraday Trans.* **1994**, *90*, 1323.

17. López-Fonseca, R.; Aranzabal, A.; Steltenpohl, P.; Gutiérrez-Ortiz, J. I.; González-Velasco, J. R. *Catal. Today* **2000**, *62*, 367.

18. Giaya, A.; Thompson, R. W.; Denkewicz Jr, R. *Microporous Mesoporous Mater.* **2000**, *40*, 205.

19. Lews, R. J. *Sax's Dangerous Properties of Industrial Materials*; 9 ed.; Van Nostrand Reinhold: New York, NY, 1996.

20. Liu, Y.; Her, J.-H.; Dailly, A.; Ramirez-Cuesta, A. J.; Neumann, D. A.; Brown, C. M. *J. Am. Chem. Soc.* **2008**, *130*, 11813.

21. Volkringer, C.; Meddouri, M.; Loiseau, T.; Guillou, N.; Marrot, J.; Férey, G. R.; Haouas, M.; Taulelle, F.; Audebrand, N.; Latroche, M. *Inorg. Chem.* **2008**, *47*, 11892.

22. Stavitski, E.; Pidko, E. A.; Couck, S.; Remy, T.; Hensen, E. J. M.; Weckhuysen, B. M.; Denayer, J.; Gascon, J.; Kapteijn, F. *Langmuir* **2011**, *27*, 3970.

23. Loiseau, T.; Serre, C.; Huguenard, C.; Fink, G.; Taulelle, F.; Henry, M.; Bataille, T.; Férey, G. *Chem. Eur. J.* **2004**, *10*, 1373.

24. Seoane, B.; Téllez, C.; Coronas, J.; Staudt, C. *Sep. Purif. Technol.* **2013**, *111*, 72.

25. Ahnfeldt, T.; Gunzelmann, D.; Loiseau, T.; Hirsemann, D.; Senker, J.; Férey, G.; Stock, N. *Inorg. Chem.* **2009**, *48*, 3057.

26. Nakagawa, I.; Mizushima, S. I. *J. Chem. Phys.* **1953**, *21*, 2195.

27. Melendez-Pagan Y, T. B. E., Ben-Amotz D *J. Phys. Chem. B* **2001**, *105*.

28. Stolov, A. A.; Remizov, A. B. *Spectrochim. Acta Mol. Biomol. Spectros.* **1995**, *51*, 1919.

29. Khrone Group. Service-Dielectric Constants. http://krohne.com/en/services/dielectric-constants/ (accessed June 10, 2014)

30. Mizushima, S.; Shimanouchi, T.; Harada, I.; Abe, Y.; Takeuchi, H. *Can. J. Phys.* **1975**, *53*, 2085.

31. Joseph, J.; Jemmis, E. D. *J. Am. Chem. Soc.* **2007**, *129*, 4620.

32. Xie, S.; Iglesia, E.; Bell, A. T. *J. Phys. Chem.* **2001**, *105*, 5144.

33. Fukushi, K.; Fukuda, T.; Kimura, M. *J. Raman Spectrosc.* **1987**, *18*, 47.

34. Volkringer, C.; Loiseau, T.; Guillou, N.; Ferey, G.; Elkaim, E.; Vimont, A. *Dalton Trans.* **2009**, 2241.

35. Cowley, E. G. *Nature* **1951**, *168*, 705.

36. Wilmsjurts, J. k. B., H.J *Can. J. Chem.* **1957**, *35*.

37. Gardiner, D. J.; Littleton, C. J.; Walker, N. A. *J. Raman Spectrosc.* **1987**, *18*, 9.

38. Millange, F.; Guillou, N.; Medina, M. E.; Férey, G.; Carlin-Sinclair, A.; Golden, K. M.; Walton, R. I. *Chem. Mater.* **2010**, *22*, 4237.

5.1 General Conclusions

This section will summarize the results of the thesis.

5.1.1 Crystallization of DNL-6

SSNMR and PXRD are powerful techniques in determining the crystallization route of silicoaluminophosphates. Obtaining intermediates from the crystallization process can give insight into the role of the surfactant, structure directing agent, and how silicon incorporates into the framework.

It was determined, through PXRD, that the hydrothermal crystallization process of DNL-6 takes roughly twenty-four hours, and an intermediate layered phase exists. The structure of the semi-crystalline layered phase is further characterized through the use of ^{31}P SSNMR in order to determine that the local environment of phosphorous is $P(\text{-}O\text{-}Al)_3(OH)$.

In the case of DNL-6, the surfactant and templating agent work as structure directing agents in the case of DNL-6. CTACl is most likely found within the larger center cages and acts as a SDA for the layered intermediate. DEA is most likely found within the LTA cages. In order to slow down the crystallization process, DGC can be employed. Using DGC it was determined that DNL-6 goes through the same crystallization pathway, however, the intermediate is not fully transformed into DNL-6. The existence of the intermediate after crystallization by DGC, may be due to the lack of SDA. In the DGC the lack of DEA seen within the pores may be due to the

lack of mobility of SDA molecules to transfer from pore to pore without a liquid phase.

Finally the silicon enters the framework solely through SM2. In SM2, only a single phosphorous atom is replaced by a single silicon atom. This creates single Si(-O-Al)$_4$ environments each of which create one Brønsted acid site per silicon atom. As seen from the CP experiments hydrogen atoms do not neutralize the framework at the same rate as silicon enters the framework. The absence of the hydrogen atom causes a temporarily negatively charged framework. The work described in this thesis does differ from past studies concerning the HTS by seeing the incorporation of the surfactant into the pores of the framework. Using DGC to slow down the reaction, is a viable alternative to HTS in studying the crystallization of SAPOs. By reducing the rate of the reaction it is possible to obtain all necessary intermediates. These intermediates allow it to be possible in understanding the formation of the framework and the individual role, played by the different templating agents.

Future work on this topic may include obtaining SEM images with elemental analysis to determine the topology and composition of the SAPO. Furthermore, it has been shown that using VPT synthesis has led to different silicon incorporation routes. Therefore, the crystallization of DNL-6 should be investigated under VPT conditions to expand knowledge of the roles of the different templating agents. Finally, the porosity of both the DGC and HTS samples should be determined by nitrogen isotherms.

5.1.2 Conformational analysis of Halocarbons in Metal Organic Frameworks

Vibrational spectroscopy is an effective and formidable tool in determining the conformation of halocarbons in MOFs.

The conformations of both DCE and BCE were studied in MIL-53, MIL-68 and MIL-53NH_2. Each MOF was chosen for its unique properties which are flexibility, two unique pores, and a polar framework, respectively. Both halocarbons exhibit the same trends for each MOF. A slight variance in the trends can be attributed to different molecular sizes and the strength of their permanent dipoles.

In MIL-53 the population of both DCE and BCE mimic that of the gaseous phase due to the low dielectric constant of BDC and a non-polar environment. The main interaction stabilizing the molecules is either vdW interaction with the MOF or the C-H bond of DCE/BCE interacting with the π systems. The lack of rearrangement of the benzene rings prevents the aromatic effect from stabilizing the *gauche* conformer. For these reasons the larger *trans* conformation is favored to maximize interactions, and additionally it is more energetically favoured in non-polar mediums.

In MIL-68 there is a stark difference between the conformation populations of DCE and BCE. Due to the small pores and distance to nearest neighbour, dipoles of DCE molecules are able to stabilize the *gauche* isomer. As BCE has a weaker dipole this phenomenon is not seen and its conformation populations resemble that of the gas phase. Furthermore, it is possible to distinguish BCE being in both pores as upon

cooling the red-shift of the trans peak, most likely caused by vdW interactions, is more pronounced in the smaller pore.

Finally in the halocarbon/MIL-53NH_2 systems there is a shift towards the *gauche* isomer as the hydrogen bonding interactions with the polar amine are able to stabilize the *guache* isomer. Upon cooling in halocarbon/MIL-53NH_2 systems the guest molecule adopts the more energetically preferred conformation, which is still the *trans* isomer.

From the analysis it was determined that MIL-53NH_2 can load roughly four times more DCE/BCE molecules into its pores then MIL-53. Future work should involve taking MOFs with large pores that are known to have a high loading value such as MIL-100 and MIL-101 and comparing their loadings against the amino modified version of the two MOFs. Doing this may prove that polar frameworks allow for more molecules to be loaded and maximize MOFs storage potential of halocarbons. Further, vibrational spectroscopy at high pressures should be undertaken to confirm that the halocarbons remain in the MOF at high pressure and that there is no change in structure of the MOF. Additionally, this may lead to a possible short-term storage option for the transport of halocarbon waste and could possibly lead to long-term storage as a viable alternative to current disposal methods utilized for halocarbon waste.

Appendix A

List of Figures

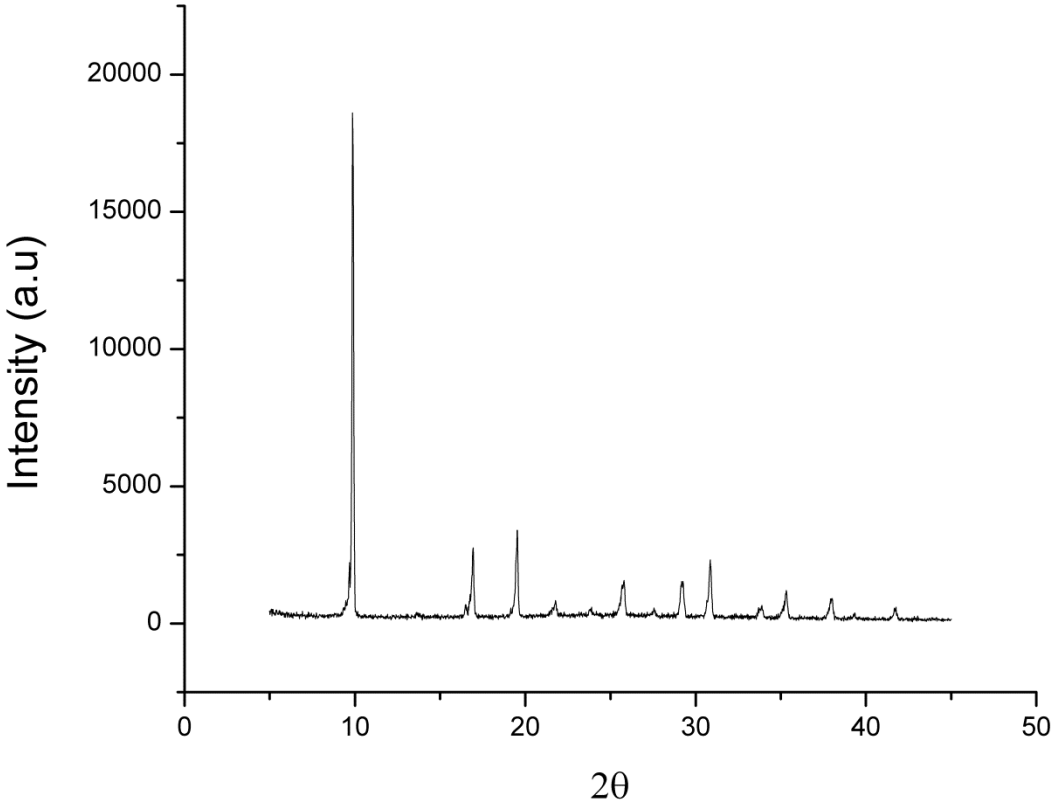

Figure A.1 DNL-6 synthesized by the hydrothermal method after 24 hours

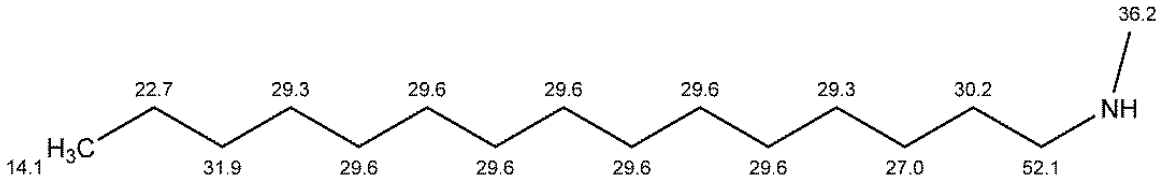

Figure A.2 ^{13}C chemical shift predictions of cetyltrimethylammonia

Appendix B

List of Figures

Page

List of Tables

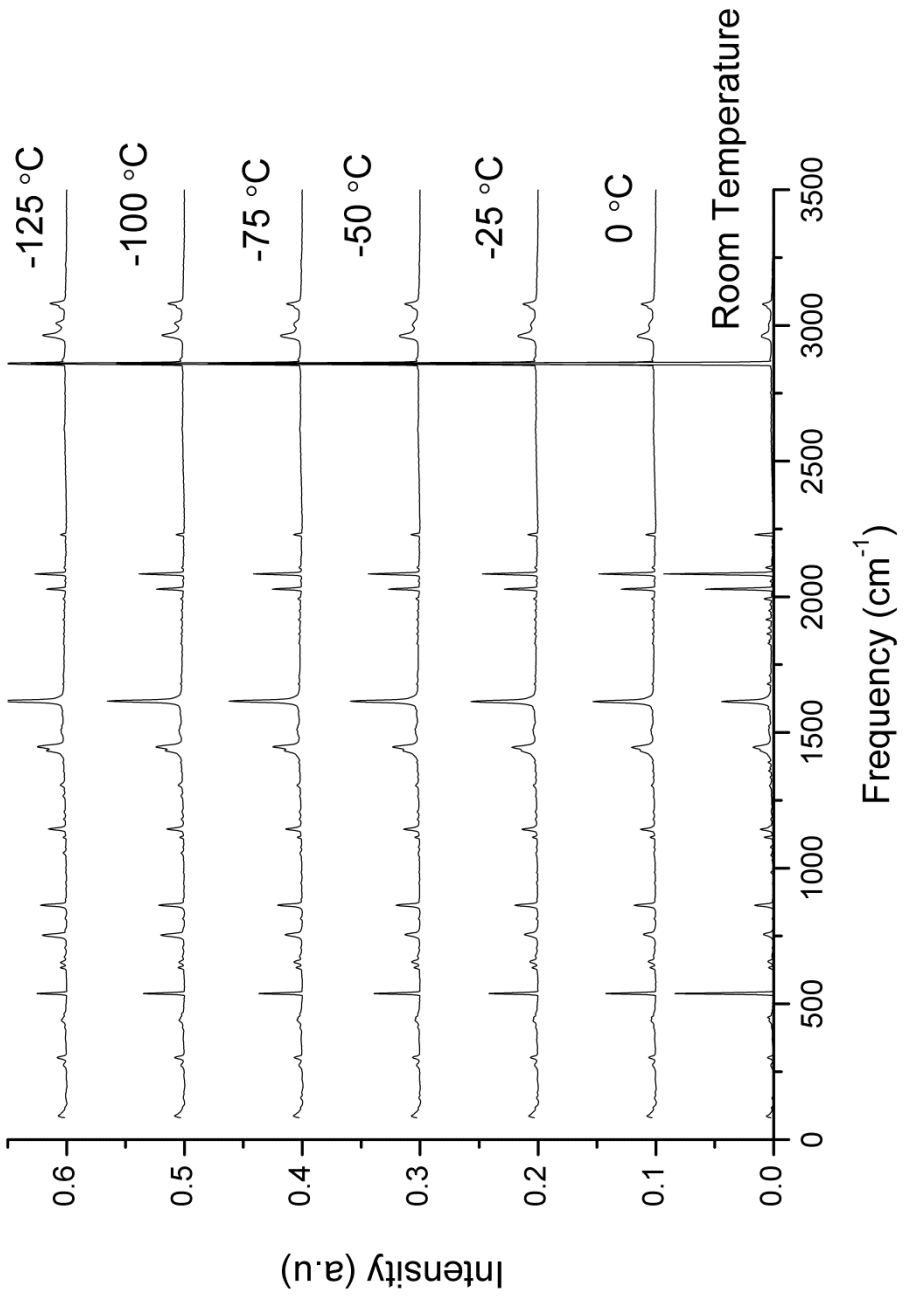

Figure B.1 FT-Raman spectra of DCE/MIL-53 system at VT

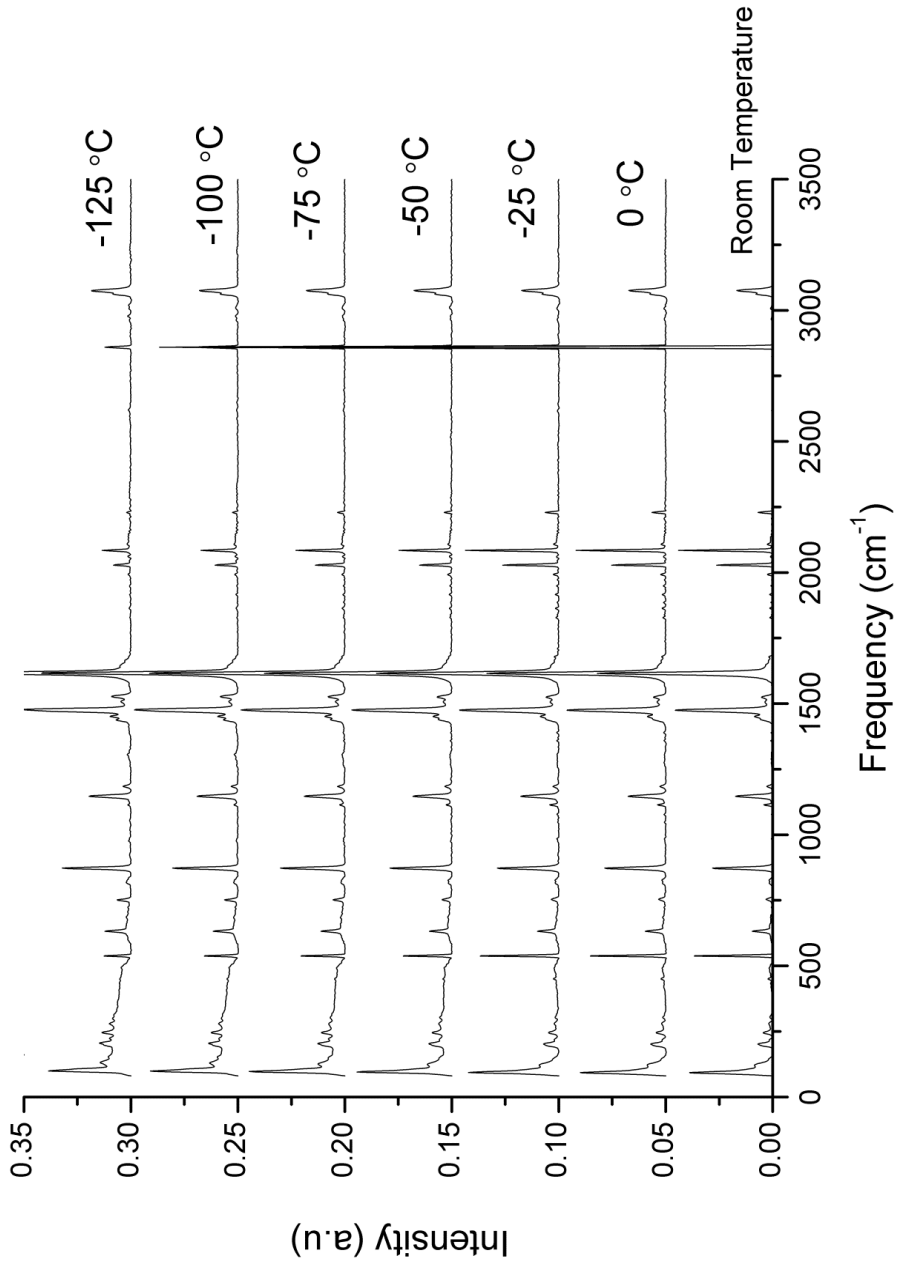

Figure B.2 FT-Raman spectra of DCE/MIL-68 system at VT

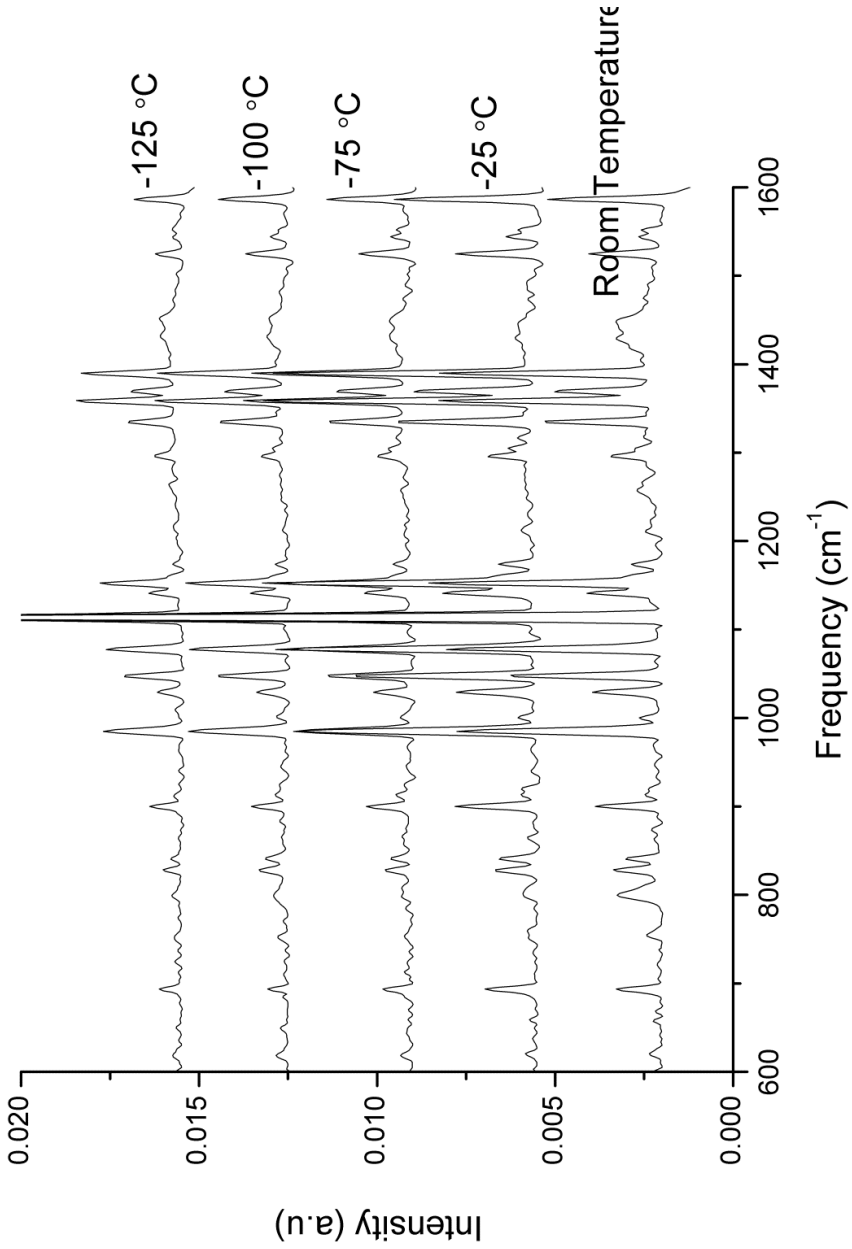

Figure B.3 FT-Raman spectra of DCE/MIL-53NH_2 system at VT

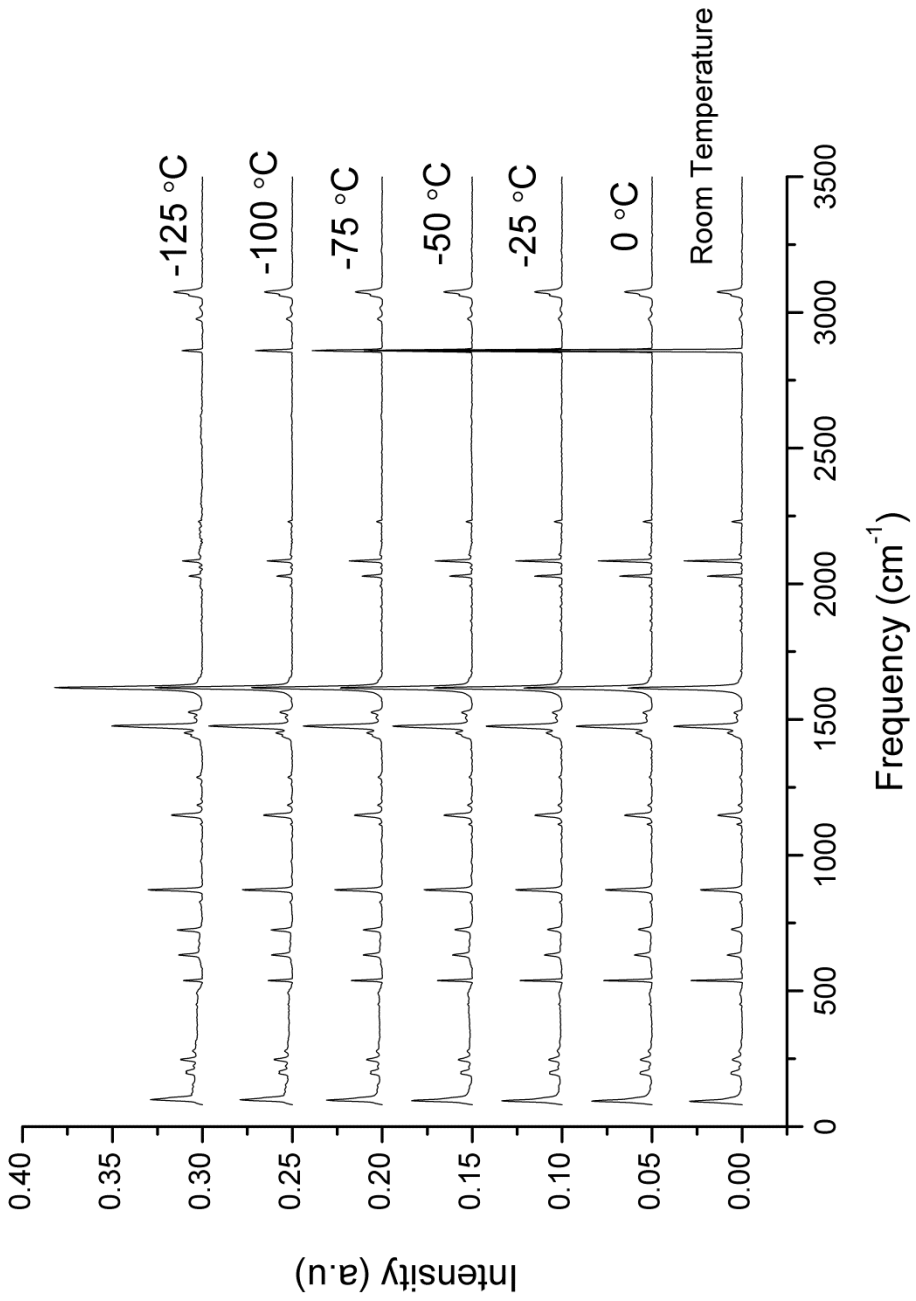

Figure B.4 FT-Raman spectra of BCE/MIL-53 system at VT

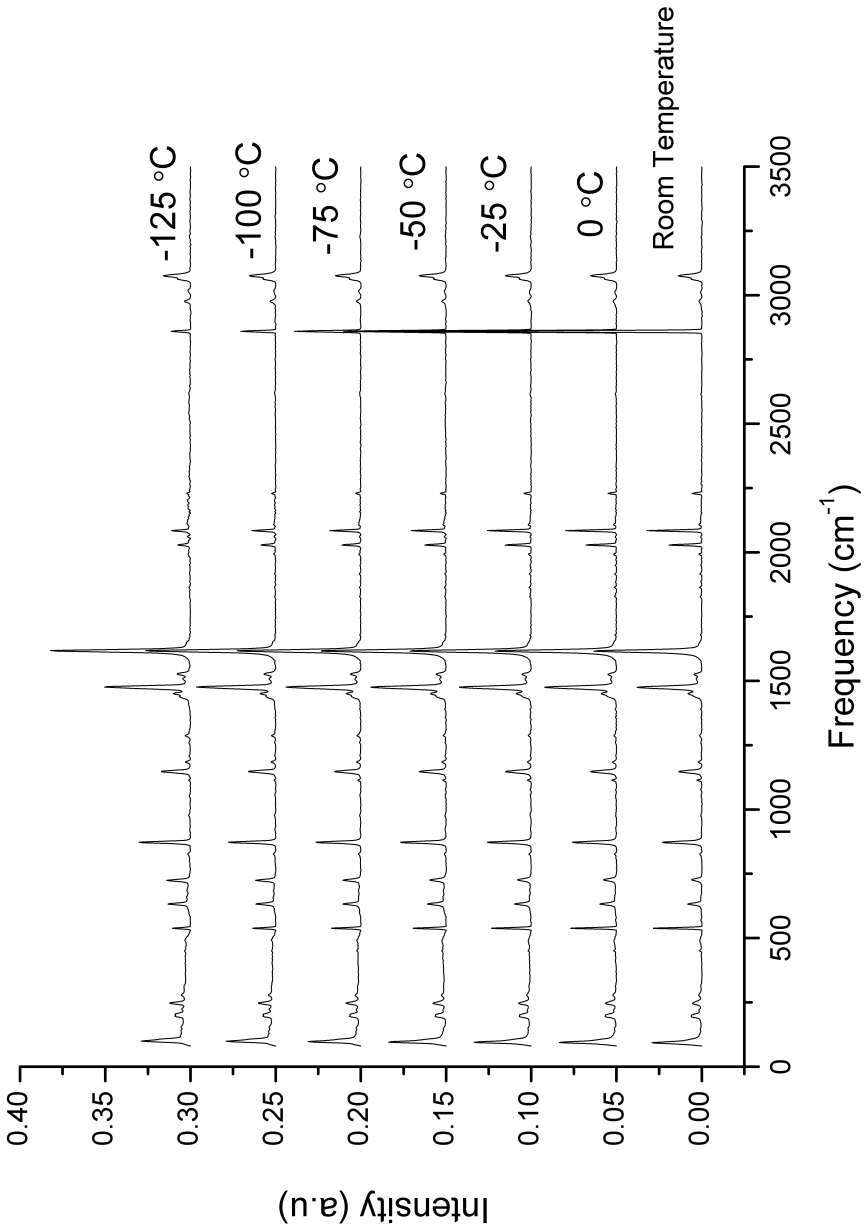

Figure B.5 FT-Raman spectra of BCE/MIL-68 system at VT

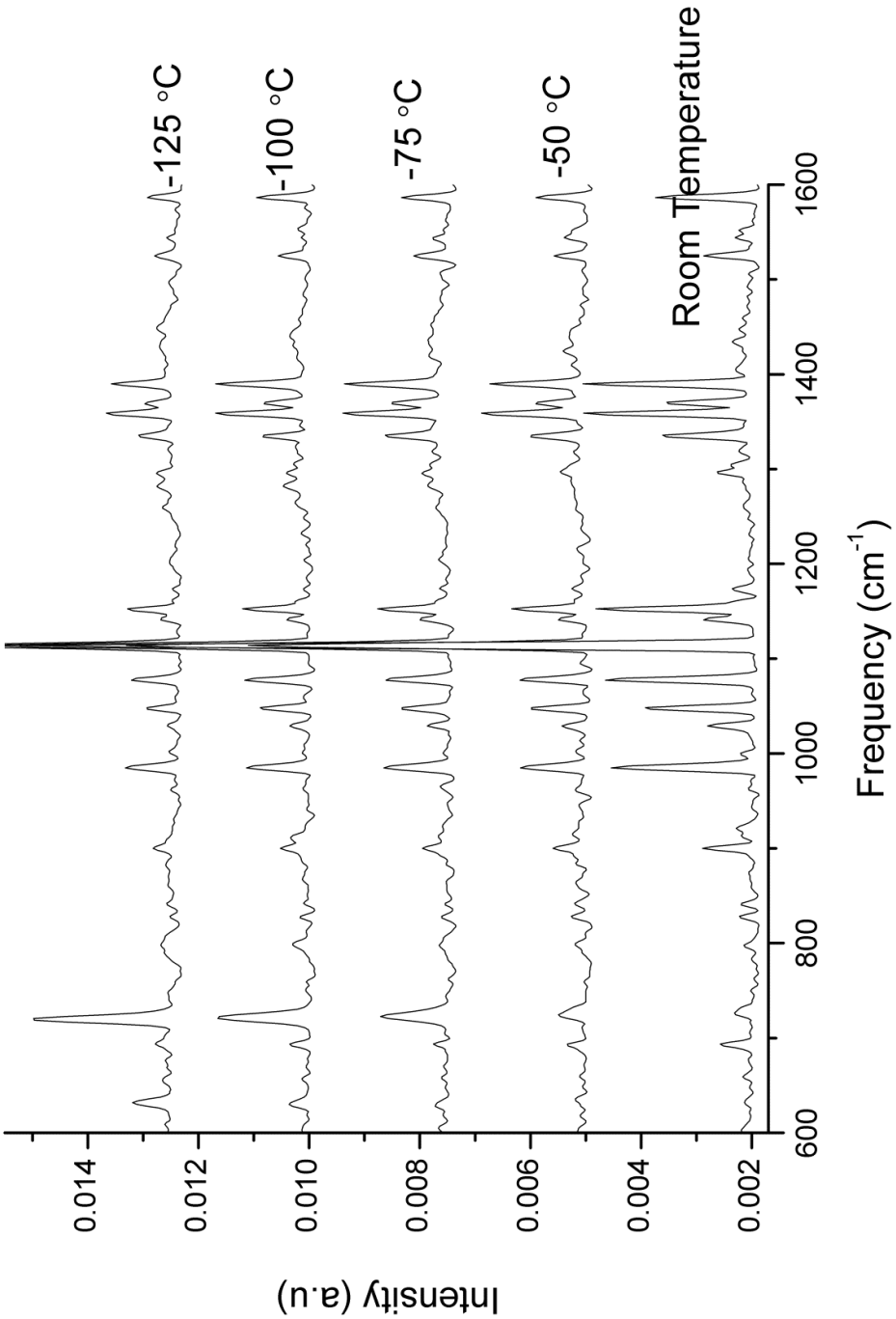

Figure B.6 FT-Raman spectra of BCE/MIL-53NH_2 system at VT

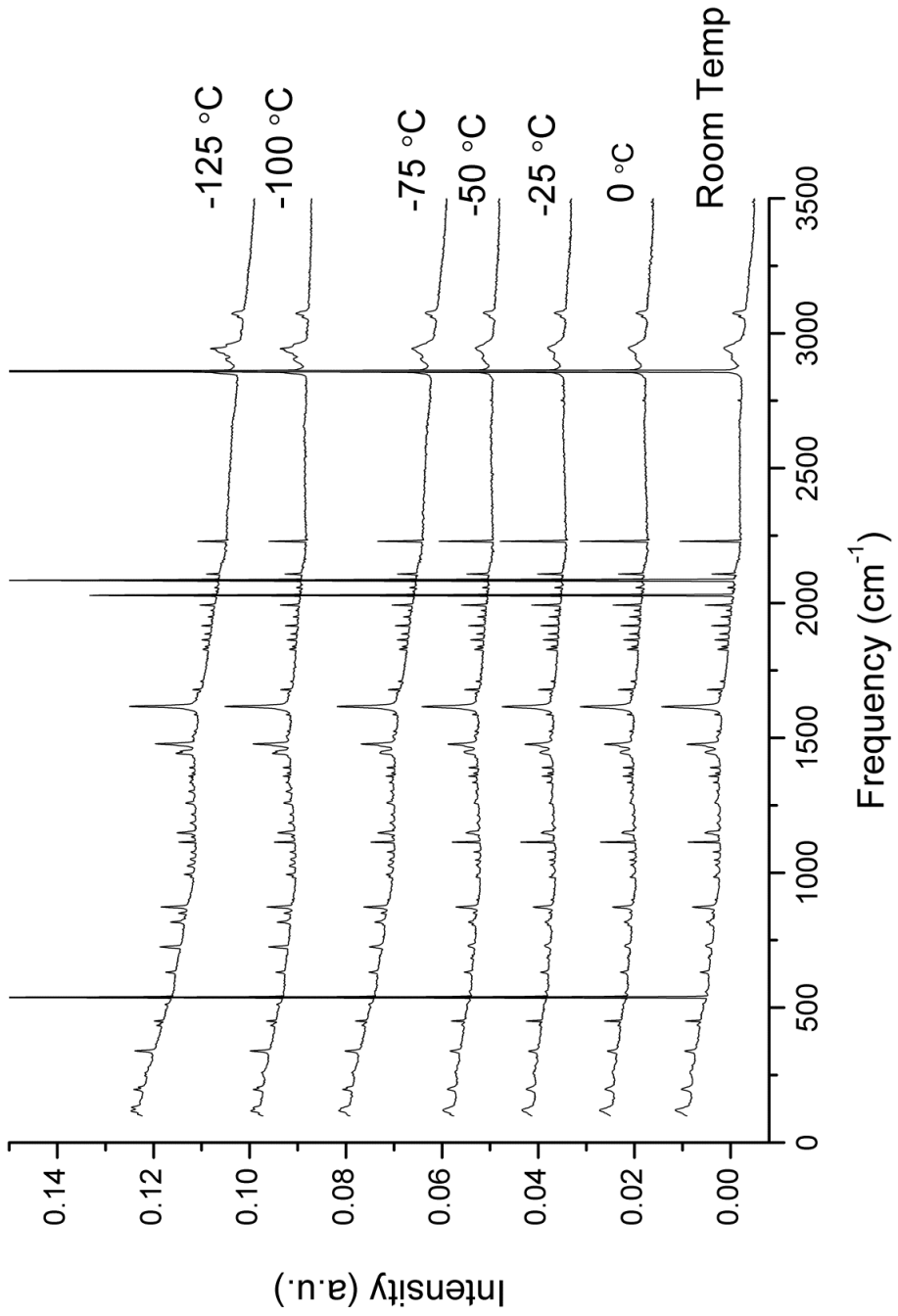

Figure B.7 FT-Raman spectra of CCH/MIL-53 system at VT

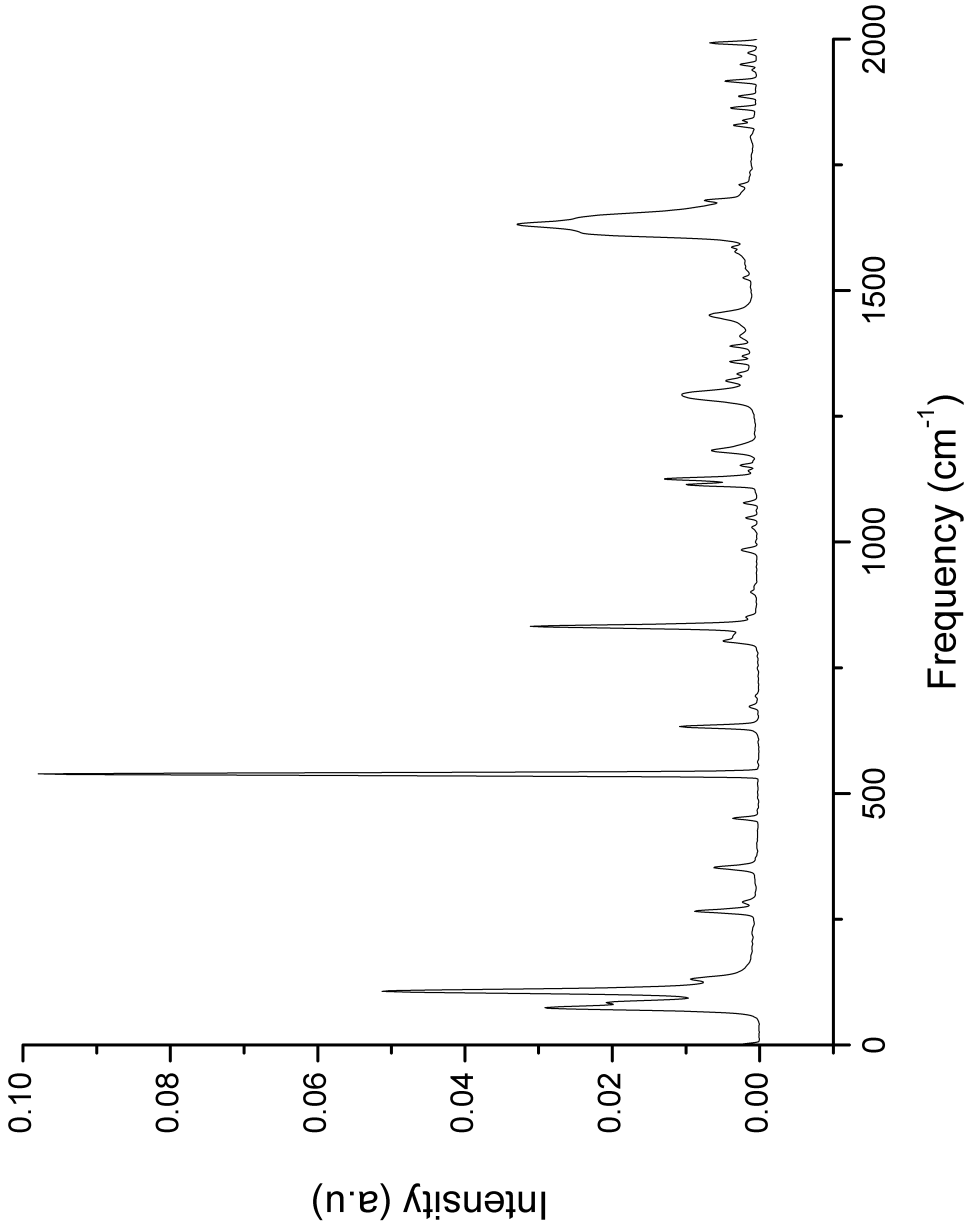

Figure B.8 FT-Raman spectra of terephthalic acid

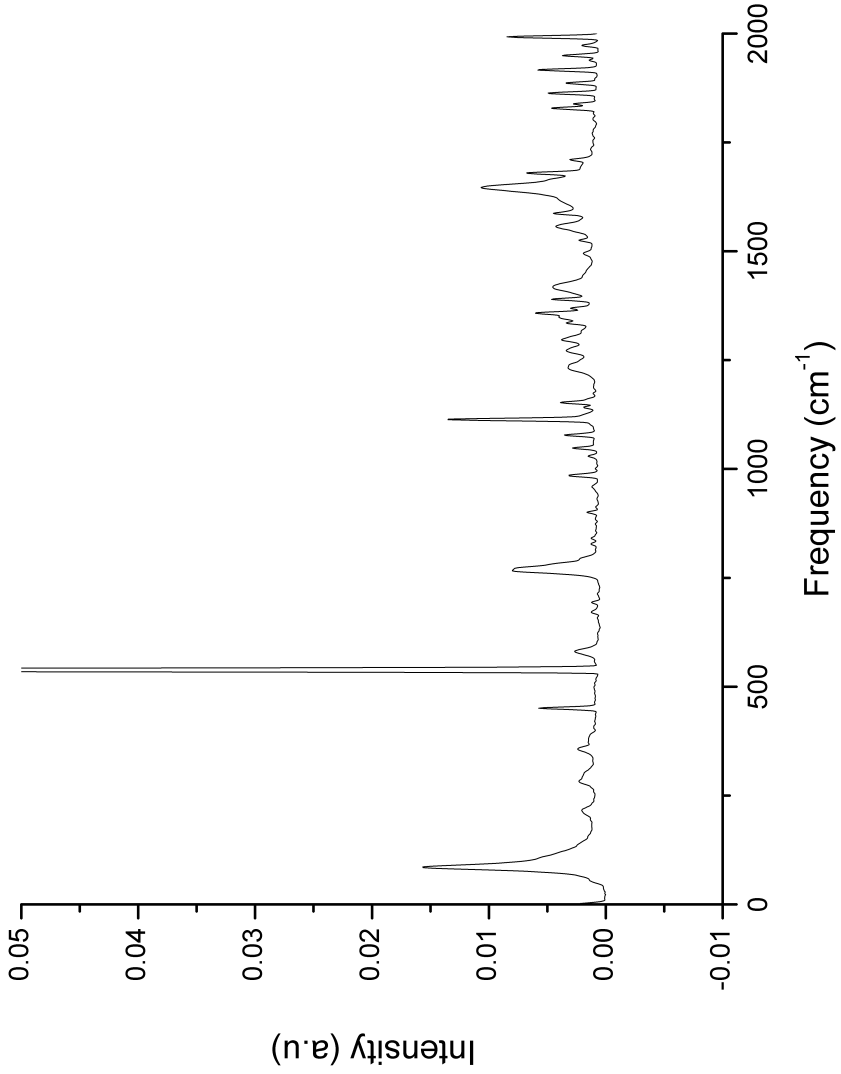

Figure B.9 FT-Raman spectra of 2-amino,1,4-benzenedicarboxylate

Table B.1 Peak Assignment for full spectra of DCE/MIL-53, DCE/MIL-68

MIL-53 DCE (cm-1)	MIL-68 DCE (cm-1)	Assignment:[1] Framework	Literature[1] (cm-1)
631	632	(CCCC)χ	633
860	862	(CC) υs	851
872		(CH)ρ	889
1143	1142	(CO)υs	1141
1439	1447	(CCH)β + (CH)υs	1409
1471		(CO)β	1449
1524	1510	(C=C)υs + (CCH)β	1520
1613	1614	(C=C)υs + (CCH)β	1611
3073	3066	(CH)υas	3074
	3079	(CH)υs	3081

ν= stretching, δ=deformation, t=twisting, ρ = rocking, ω = wagging, β=in-plane bending, γ=out-of-plane bending and τ= torsion

Table B.2 Peak Assignment for full spectra of DCE/MIL-53NH_2

MIL-53NH_2 DCE (cm-1)	Assignment: [2] Framework	Literature[2] (cm-1)
693		*690*
754	C-Cl (*trans*)υs	755
798	*γ*CCOO	*782*
901	*γ*CH	910
985	*γ*CH	*986*
1049	*v*CC_{ring}+ r NH_2	*1054*
1076	*v*C–OH + r NH_2 + *v*CC_{ring}	*1089*
1114	*β*CH + *v*CC_{ring}+ *v*C–OH + r NH_2	*1128*
1152	*β*CH+ *v*CC_{ring}	*1177*
1361	*v*CC_{ring} + *β*OH + *β*OH	*1355*
1390	*v*CC_{ring}+ *v*C–CA	1392
1524	*β*CH+ *v*CC_{ring}	*1524*
1585	*v*CC_{ring}+ *ρ*NH_2	1580

ν= stretching, δ=deformation, t=twisting, ρ = rocking, ω = wagging, β=in-plane bending, γ=out-of-plane bending and τ= torsion

Table B.3 Peak Assignment for full spectra of BCE/MIL-53, BCE/MIL-68

MIL-53 BCE (cm-1)	MIL-68 BCE (cm-1)	Assignment: [1] Framework	Literature[1] (cm-1)
860	862	(CC) υs	851
872		(CH)ρ	889
1143	1142	(CO)υs	1141
1439	1447	(CCH)β + (CH)υs	1409
1471		(CO)β	1449
1524	1510	(OH)υs	1520
1613	1614	(C=C)υs + (CCH)β	1611
3073	3066	(CH)υas	3074
	3079	(CH)υs	3081

ν= stretching, δ=deformation, t=twisting, ρ = rocking, ω = wagging, β=in-plane bending, γ=out-of-plane bending and τ= torsion

Table B.4 Peak Assignment for full spectra of BCE/MIL-53NH_2

MIL-53NH_2 BCE (cm-1)	Assignment: [2] Framework	Literature[2] (cm-1)
797	γCCOO	782
901	γCH	910
986	γCH	986
1049	νCC_{ring}+ r NH_2	1054
1078	νC–OH + r NH_2 + νCC_{ring}	1089
1113	βCH + νCC_{ring}+ νC–OH + r NH_2	1128
1172	βCH+ νCC_{ring}	1177
1357	νCC_{ring} + βOH + βOH	1355
1390	νCC_{ring}+ νC–CA	1392
1524	βCH+ νCC_{ring}	1524
1586	νCC_{ring}+ ρNH_2	1580

ν= stretching, δ=deformation, t=twisting, ρ = rocking, ω = wagging, β=in-plane bending, γ=out-of-plane bending and τ= torsion

1. Téllez S, C. A.; Hollauer, E.; Mondragon, M. A.; Castaño, V. M. *Spectrochim. Acta Mol. Biomol. Spectros.* **2001**, *57*, 993.

2. Karabacak, M.; Cinar, M.; Unal, Z.; Kurt, M. *J. Mol. Struct.* **2010**, *982*, 22.

Curriculum Vitae

Education

Graduate Student, M.Sc., Inorganic Chemistry
2012 – 2014
Western University, London, Ontario

Academic Courses:

- Surface Science – 87%
- Crystallography 1 – 83 %
- Vibrational Spectroscopy of Solid-state Materials – 78%
- Seminar – 82%

Bachelor of Science, Chemistry
2009 - 2012
McGill University, Montreal, Quebec

Positions and Working Experience

Teaching Assistant, Chem 1302 Department of Chemistry, Faculty Of Science, Western University, Winter Term 2014.

Teaching Assistant, Chem 1301 Department of Chemistry, Faculty Of Science, Western University, Fall Term 2013.

Teaching Assistant, Chem 1100/1200 Department of Chemistry, Faculty Of Science, Western University, Summer Term 2013.

Teaching Assistant, Chem 1100 Department of Chemistry, Faculty Of Science, Western University, Fall Term 2012.

Research Experience

September 2012-Present
Supervisor: Dr. Yining Huang

- Synthesis and characterization of SAPO
- Vibrational Spectroscopy of guest organic molecules in MOFs

Summer 2011
Supervisor: Dr. Ian Butler

- Synthesis of aliphatic nitrenium compounds

Conferences

Inorganic Discussion Weekend
November 8-10 2013:
Poster: "Raman Study of Guest-Host Interactions of Halocarbons in Metal Organic Frameworks" Maxwell Goldman, Yining Huang.

CAMBR Day
November 1st 2013:
Poster: "Raman Study of Guest-Host Interactions of Halocarbons in Metal Organic Frameworks" Maxwell Goldman, Yining Huang.